Mass selected copper clusters on well-ordered aluminum oxide layers

Dissertation

zur Erlangung des akademischen Grades
Doktor der Naturwissenschaften

vorgelegt von

Dominik Wolter
geboren in Arnsberg

technische universität
dortmund

Lehrstuhl für Experimentelle Physik I
Fakultät Physik, März 2018

1. Gutachter : Prof. Dr. Heinz Hövel
2. Gutachter : Prof. Dr. Mirko Cinchetti

Datum des Einreichens der Arbeit: 29. März 2018

Contents

Chapter 1

Introduction

Oxide surfaces are well known though often unwanted as they appear in the form of rust. This unfavorable effect is caused by an electron transfer from e.g. metal to oxygen and amplified by heat. A bane not only for car manufactures turns out as a boon for electronic industries. Oxides are mainly used as insulators with a wide range of application. For high voltage insulation it is namely aluminum oxide that prevents flash-overs when electricity is carried over huge distances. But also surfaces of oxides have already found a way in our everyday life. Each transistor in modern cell phones, cameras and computers is based on an insulating oxide layer between the gate material and the conducting channel. While these oxides mainly focus on the insulating character, the structure is more or less arbitrary. However, this thesis concentrates on well-ordered oxide layers of aluminum oxide. By exposing a clean Ni_3Al surface to oxygen in an ultra high vacuum at elevated temperatures, it is feasible to obtain a long-range ordered Al_2O_3 film of approximately 5 Å thickness [Bar92]. This oxide film exhibits hexagonal arranged, 4.16 nm spaced sites, which serve as nucleation points for evaporated metal atoms [Buc10]. Also a second honeycomb-like lattice is present and suitable for adsorption [Kho13]. As can be seen in figure 1.1 the oxide film is well-suited to grow nanostructured palladium cluster arrays. However, these arrays contain polydisperse clusters.

The accumulated metal atoms may have unique electronic, optic and catalytic properties depending on their size. Even our ancestors took implicitly advantage of nanoparticles by using them as additives during glass-making, leading to different colors and optical effects [Col09]. Nowadays a whole field in physics is dedicated to quantize properties of so-called clusters. Over the past decades, many impressive scientific results especially concerning catalysis [Hug05] were achieved. Possible applications even reach into other disciplines like medicine. Gadolinium

ions trapped in C_{60} clusters, which are then enclosed by silicon particles, can be used as contrast agents for magnetic resonance imaging, enhancing the magnetic contrast by a factor of 50 [Ana10]. The semiconductor industry has always been interested in shrinking existing structures. But as standard lithography processes will soon come to a limit, cluster physics may find the way out: by using a bottom-up approach, where functionalized structures are build up of individual nanoparticles, it is possible to introduce sub-nanometer transistors switchable by a single electron [Par00].

In most cases, an exact size selection is crucial, because properties like catalytic activity vary dramatically by adding or removing a single atom [Lim06]. Therefore it is necessary to maintain a size selection even after depositing clusters either on a substrate or in a matrix material. Depending on both, the substrate and cluster material, coalescence or ripening potentially occur, ruining unique features. Since the Al_2O_3/Ni_3Al system exhibits binding sites for cluster growth, it could serve as a template for nanostructuring, leading to size selected, equally spaced clusters on that surface.

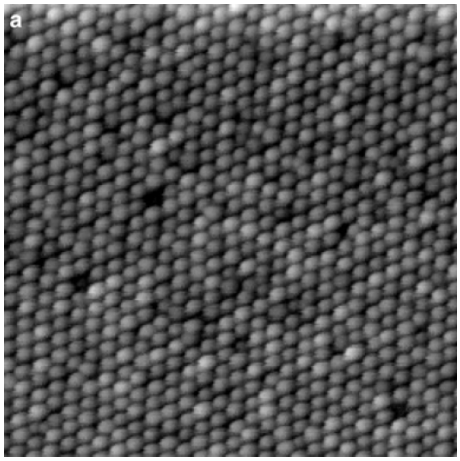

Figure 1.1: Polydisperse Pd clusters grown on Al_2O_3/Ni_3Al. Reproduced from Ref. [Deg04] with permission from The Royal Society of Chemistry.

In this thesis the suitability of the template structure given by Al_2O_3/Ni_3Al for deposition of size selected metal clusters is investigated. While the following chapter deals with some essential knowledge about clusters and their properties in contact with surfaces, chapter 3 focuses on techniques to investigate the quality of the oxide film and the deposited clusters properly. In order to determine the cluster positions on the surface, scanning tunneling microscopy is the method of choice. Low energy electron diffraction reveals the quality of the (un)oxidized sample at an averaging level. The used instruments for sample preparation, cluster deposition and analysis are introduced in chapter 4. Oxidation of the sample requires a low background pressure at specific elevated temperatures, which is achieved by electron bombardment and infrared pyrometry. Furthermore, new electronics for improved mass selection are introduced. A recipe for obtaining well-ordered aluminum oxide layers on the Ni_3Al surface can be found in chapter 5 together with a verification of the quality of the produced oxide

film. Chapter 6 contains the results concerning the arrangement of clusters on the surface compared to Monte Carlo simulations as well as the apparent height, which strongly depends on the tunneling junction. Spectroscopic measurements were also performed and yield an interpretation of the different heights. This is supported by modeling and numerically solving a double tunneling barrier circuit. The results are discussed in chapter 7, while chapter 8 handles with improvements and additional ideas to the sample system.
The appendix contains the commented Monte Carlo source code used for simulations in chapter 6 and is also dealing with the movement of the UHV system to a new building, which was a major part of the instrument-based work done. Hence vibration velocity measurements of the basement for reliable operation of scanning probe microscopy were performed. The dimensioning of a new foreline pumping system was also documented. Parameters for the various cluster depositions can be found in the appendix as well.

Chapter 2

Essentials

This chapter will provide some essential knowledge about clusters and their interaction in contact with surfaces. After a brief description of geometric and electronic properties of clusters, ripening processes and the mobility of clusters on surfaces are discussed.

2.1 Clusters

Cluster physics takes place in the transition region between particle and molecular physics on the one hand and condensed matter physics on the other hand. Thus the high ratio of surface atoms to those in the bulk is distinctive. However, a broad size range applies to the term clusters. A coarse classification, taken from [Hab06], is more or less common:

- Small clusters with 2 - 13 atoms show discrete energy levels and nearly all atoms are on the surface. Actually these clusters can be regarded as molecules.
- Medium sized clusters, composed of less than 100 atoms, often appear in different isomers, even if the number of atoms is equivalent. Energy levels begin to merge, thus, molecular approaches e.g. for the prediction of electronic properties cannot be applied successfully in every scenario.
- Large clusters with hundreds of atoms are more or less spherical and form energy bands rather than discrete levels. Some approximations for continuous problems can be applied.
- Micro-crystals, starting at several thousands of atoms, have most properties of bulk material but are sometimes referred to as clusters.

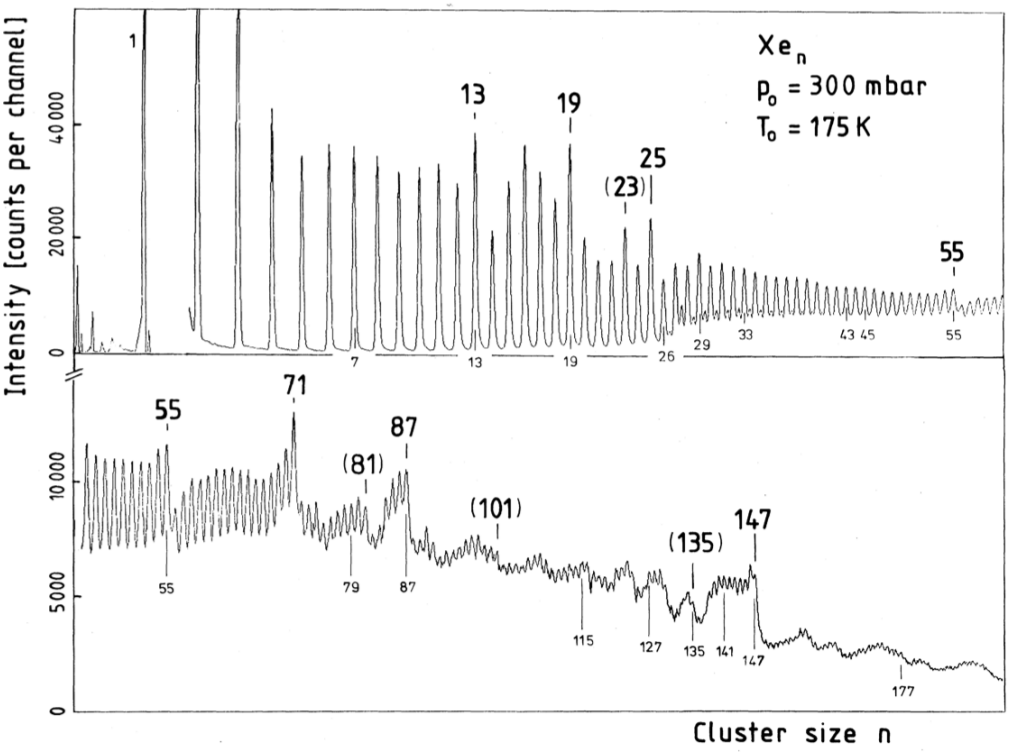

Figure 2.1: Mass spectrum of xenon clusters. Peaks with higher intensity compared to adjacent maxima are labeled with the number of atoms composing the cluster. Less relevant peaks are written in brackets. Reprinted figure with permission from [Ech81]. Copyright 1981 by the American Physical Society.

The shape of especially medium sized clusters differ heavily. Possible geometric objects are an icosahedron with 20 triangular faces, the dodecahedron with its 12 pentagonal faces or other platonic solids like the tetrahedron for only a few atoms in the cluster. A more common polyhedron is the decahedron since it can be formed through a face-centered cubic structure. Arising from the nucleation regime, a broad number of different shapes were already identified [Bar15]. Nevertheless, it seems like the icosahedral shape is preferred if the formation of a whole shell can be accomplished. This manifests in a higher occurrence of clusters with 13, 55, 147, ... atoms as it is shown in figure 2.1. These geometric magic numbers are calculated through the formula

$$N(\ell) = \frac{10\ell^3 - 15\ell^2 + 11\ell - 3}{3} \quad ,$$

where ℓ stands for the number of closed shells [Mac62]. For any ℓ, icosahedra have the highest surface to volume ratio behind a sphere. Therefore, it is reasonable to assume a sphere when calculating the diameter of an icosahedral shaped

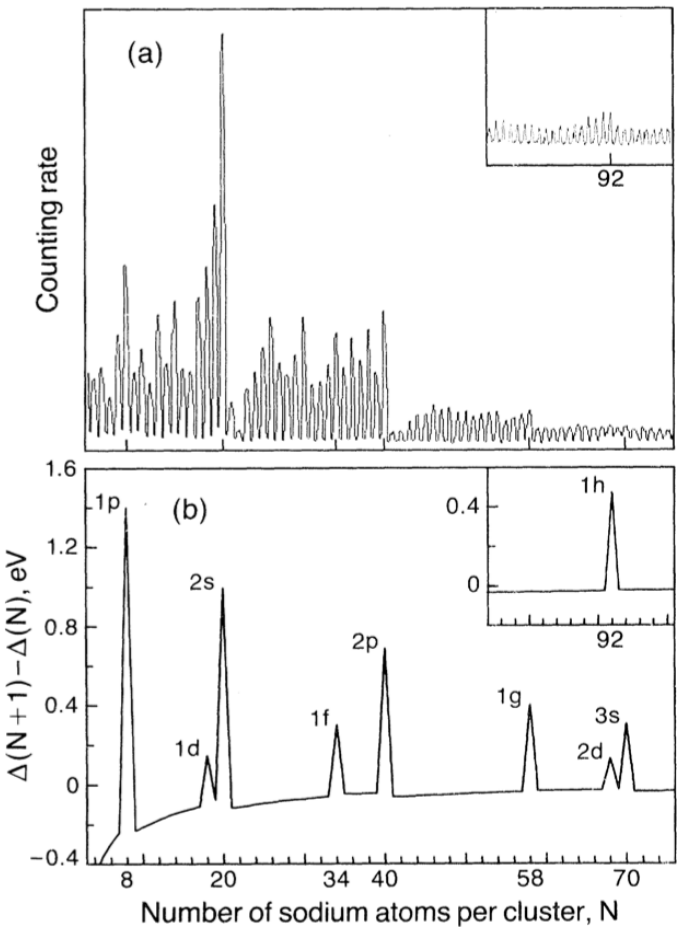

Figure 2.2: (a) Mass spectrum of sodium clusters. (b) Change of the electronic energy determined with a one-electron shell model. Reprinted figure with permission from [Kni84]. Copyright 1984 by the American Physical Society.

cluster [Hab06]. Neglecting packing effects, the volume of the cluster equals the number of atoms multiplied by the volume of a single (spherical) atom given by the Wigner-Seitz radius

$$r_{\mathrm{s}} = \left(\frac{3M}{4\pi \varrho N_{\mathrm{A}}} \right)^{\frac{1}{3}} \quad ,$$

where M stands for the molar mass, ϱ represents the density of the bulk material and N_{A} is the well-known Avogadro constant. Thus, the diameter reads

$$d = 2 r_{\mathrm{s}} N^{\frac{1}{3}} \quad . \tag{2.1}$$

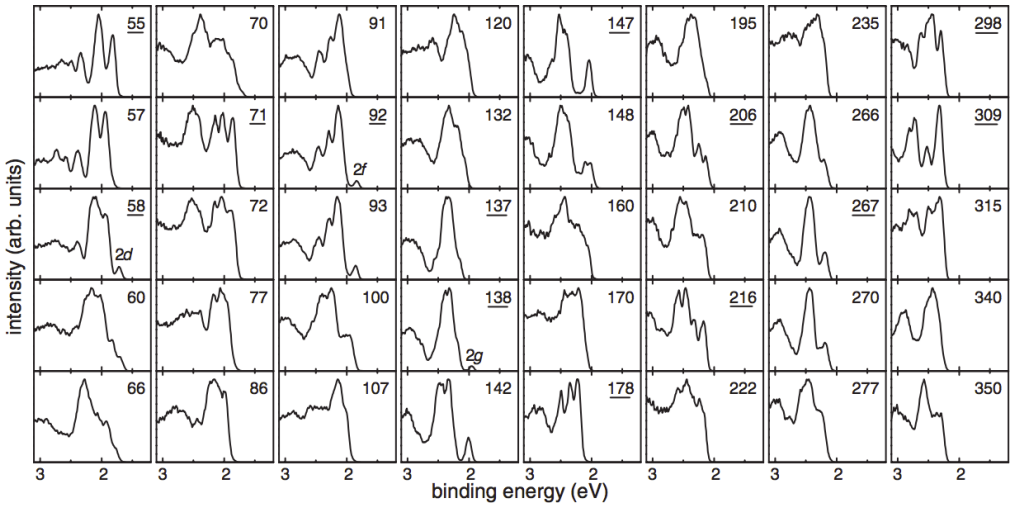

Figure 2.3: Photoelectron spectra of sodium clusters. In the upper right, the number of atoms composing a cluster is denoted. Reprinted figure with permission from [Kos07]. Copyright 2007 by the American Physical Society.

Furthermore, the existence of electronic magic numbers was also verified as shown in figure 2.2. A completely filled electronic shell yields higher stability. An explanation can be given by means of the Jellium model, where the cluster is simplified to a positive charged background, which is combined with delocalized electrons in different shells. The calculated magic numbers strongly depend on the used potential and can therefore not be specified in general. According to figure 2.2, prominent peaks occur at 8, 20, 40 atoms forming a sodium cluster.
In order to prove the filling of electronic shells quantitatively, spectroscopic measurements are necessary. Hence, electrons are ejected from a free cluster by e.g. UV radiation and their energy is analyzed. The specific distribution (spectrum) then provides information about the electronic structure. Further electronic magic clusters were identified with 58, 92 and 138 atoms forming a sodium cluster [Kos07]. It should be noted that these sodium clusters are anions i.e. they are singly negatively charged. The additional electron is located in the next shell and a signal from this electron indicates a closed-shell cluster with the given number of atoms as it is depicted in figure 2.3.
As already stated in the introducing chapter, the exact number of atoms is crucial for both, electronic and geometric properties. This was also emphasized in previous publications e.g. for platinum clusters and their catalytic activity regarding the oxidation of carbon monoxide [Hei99]. Retaining a size selection after deposition on a substrate might be challenging due to additional influences caused by the supporting material.

2.2 Interactions With Substrates

When single atoms or clusters get in contact with a surface they can either be chemisorped or physisorped. The latter requires less energy and is in most cases reversible. This mechanism is driven by van der Waals forces. Whereas chemisorption changes the electronic properties of the surface and/or the adsorbate, leading to newly formed bonds. Upon a certain level and depending on the cluster and substrate material, the kind of adsorption can be controlled by the impact energy during deposition. To preserve the electronic and geometric properties of clusters after deposition, physisorption and hence less interaction with the substrate is preferred. Nevertheless, this interaction cannot be completely switched off.
Possible consequences for clusters in contact with surfaces are deformations up to mono-atomic wetting. This rather strong interaction between substrate and cluster material leads to island formation and was observed e.g. for medium sized silver clusters deposited on the (111)-surface of a gold crystal [Grö12].
But even if the interaction is such weak that the geometry of clusters is preserved, diffusion processes might play a role. If energetically more favorable, two adjacent clusters merge to form a bigger one. Depending on the dynamics, this mechanism is called Smoluchowski ripening. The process implies that entire clusters have a certain mobility i.e. they can move freely on a surface, which is also of importance for aligning with a template structure after deposition. A track of a single Pd cluster, which was traced by an STM tip, can be found in figure 2.4.
Another way of ripening is the exchange of atoms. Ostwald ripening describes the growth of large clusters by the expense of smaller surrounding clusters. This can be explained by means of binding energy per atom in different sized clusters. Each atom in a small cluster is weaker bound than in a bigger one due to the higher surface to volume ratio. Referring to the Gibbs-Thomson effect, small clusters (with higher surface to volume ratio) have a higher effective vapor pressure. A visualization of the Ostwald ripening process is depicted in figure 2.5. A comprehensive study of growth mechanisms, including diffusion processes, can be found in [Ven84].
All of the mentioned processes ruin the mass selection and thus the unique geometric and electronic properties of the deposited clusters. The method of choice to gain information about particles after deposition and a verification of retained mass selection is the scanning tunneling microscopy technique, which will be described in detail in the following chapter.

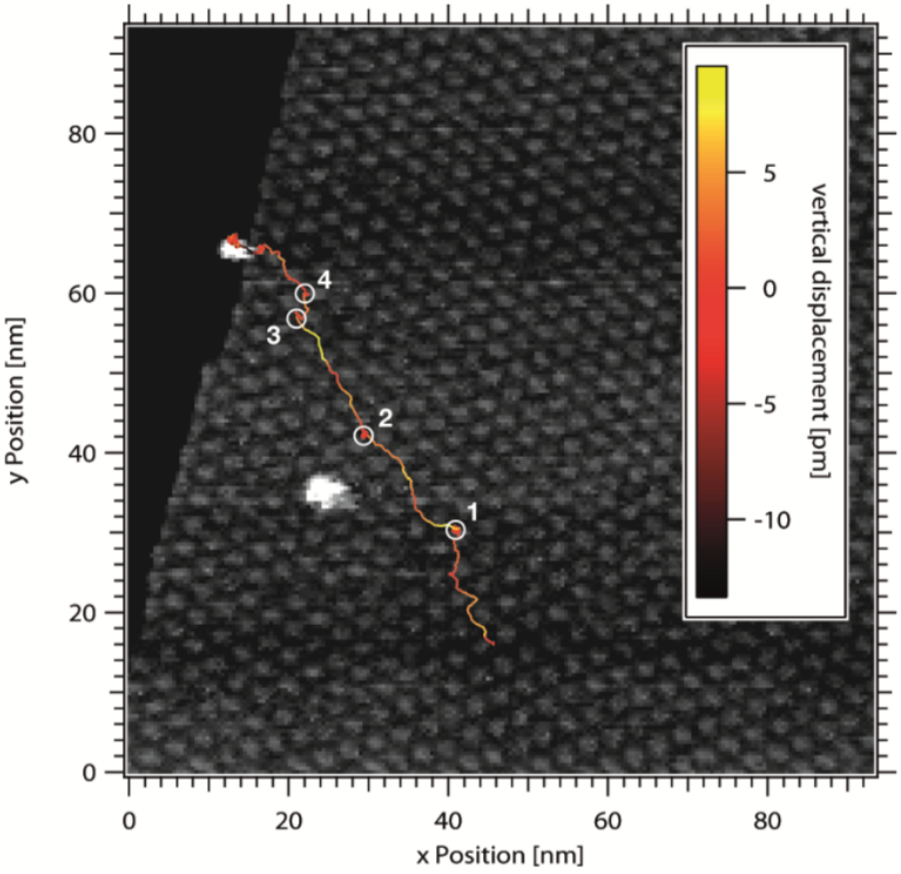

Figure 2.4: Track of a small Pd cluster on graphene/Rh(111) support, taken from [Fuk16]. The numerated white circles mark the four main resting points.

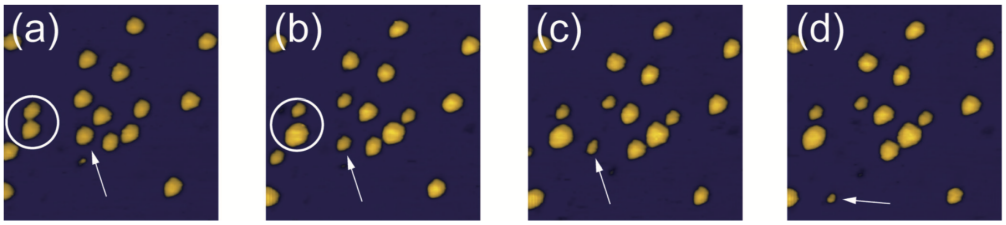

Figure 2.5: Ripening process of monodisperse Pd particles on Rh(111) substrate at room temperature. (a) was recorded immediately after deposition, (b) after 7:38 h, (c) after 17:00 h and (d) after 17:45 h. Reprinted figure from [Fuk13] by permission of WILEY-VCH Verlag GmbH & Co. KGaA, Copyright 2013.

Chapter 3

Techniques

This chapter provides a brief theory of the used techniques for sample quality verification and data acquisition. The major method for characterizing oxide films at an averaging level is the diffraction of low energy electrons. To reveal local details down to the nanometer scale, Scanning Tunneling Microscopy is the most appropriate approach.

3.1 Scanning Tunneling Microscopy/Spectroscopy

The Scanning Tunneling Microscopy (STM) technique was developed in the early 1980s by Gerd Binning and Heinrich Rohrer at the IBM research facility in Zurich. They achieved the first atomically resolved measurement of a gold surface in real space [Bin82]. In 1986 Binning and Rohrer were awarded the Nobel Prize for physics.
The STM principle relies on the tunneling effect, which occurs between two (vacuum-separated) conductors while an electric potential is present. If using a sharp tip in sub-nanometer distance to a surface, it is possible to obtain the resulting current via first-order perturbation theory

$$I = \frac{2\pi e}{\hbar} \sum_{\mu,\nu} f(E_\mu)\left[1 - f(E_\nu + eV)\right] \left|M_{\mu,\nu}\right|^2 \delta(E_\mu - E_\nu) \quad , \tag{3.1}$$

where $f(E)$ is the Fermi function, E_μ and E_ν are energies of states in the tip respectively the sample, V is the applied voltage and $M_{\mu,\nu}$ represents the tunneling matrix between states ψ_μ and ψ_ν. This approach was introduced by Tersoff and Hamann in 1983 [Ter83]. The tunneling matrix is similar to the

current operator known from quantum mechanics

$$M_{\mu,\nu} = \frac{\hbar^2}{2m} \int \mathrm{d}\vec{S} \left(\psi_\mu^* \nabla \psi_\nu - \psi_\nu \nabla \psi_\mu^*\right) \quad ,$$

which has to be integrated over any surface $\vec{S}$ within the tunneling area. To simplify expression (3.1) a series of assumptions is made. The temperature is meant to not exceed room temperature, which roughly transforms the Fermi function into a Heaviside step function. The tunneling voltage is constrained to be much lower than the average work function Φ of the tip and the sample. By further modeling the tip wave function with spherical symmetry and assuming a homogeneous density of states for the tip, the tunneling current is proportional to the local density of states (LDOS) of the sample

$$I \sim \sum_\nu |\psi_\nu(\vec{r}_0)|^2 \, \delta(E_\nu - E_\mathrm{F}) \equiv \rho_\nu(\vec{r}_0, E_\mathrm{F}) \quad ,$$

where $\vec{r}_0$ denotes the position of the tip and E_F represents the Fermi edge. Since the LDOS decays exponentially when increasing the distance d to the sample the tunneling current shows this dependence likewise. If eventually moving the tip across a surface, it is possible to obtain a visualization of the LDOS in real space. The STM enables spectroscopic measurements as well. In local tunneling spectroscopy the tip is held at a certain position and the current is recorded while tuning the gap voltage. This implies usually higher electric potentials between tip and sample. For that case it obviously cannot be assumed that the LDOS is measured at the Fermi edge. The contribution of all energies between E_F and eV, weighted by a transmission function, has to be integrated to gain the correct tunneling current. An energy level scheme as shown in figure 3.1 illustrates the actual conditions. The first derivative allows then access to the LDOS spectrum depending on the gap voltage

$$\frac{\mathrm{d}I}{\mathrm{d}V} \sim \rho_\nu(\vec{r}_0, eV)$$

with fixed $\vec{r}_0$ and tunable voltage V, assuming that the structure of the tip density of states can be neglected (mostly featureless tip DOS compared to sample DOS with features in figure 3.1). By increasing the electric potential further, field emission effects have to be taken into account. A detailed explanation regarding the calculations can be found in [Voi15].

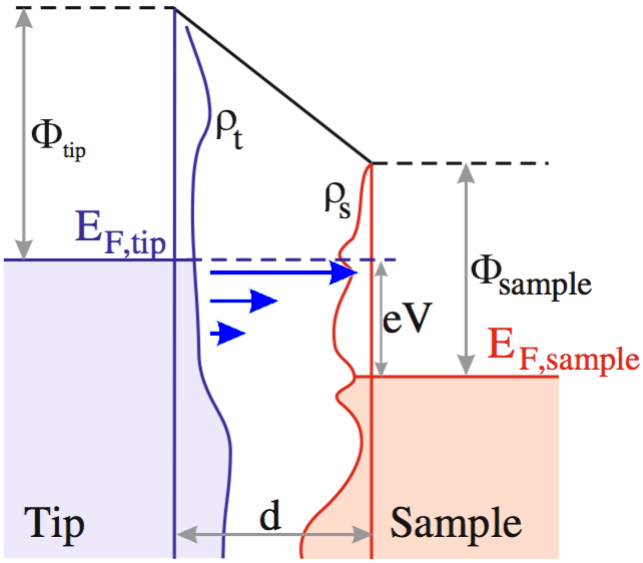

Figure 3.1: Scheme of relevant energy levels concerning the tunneling junction. Occupied states of the DOS are colored. The Fermi level is shifted by eV due to the applied voltage. Reprinted figure from [Voi15] by permission of Springer Nature, Copyright 2015.

3.2 Low Energy Electron Diffraction

The diffraction of low energy electrons (LEED) can be traced back to Davisson and Germer, who measured the number of electrons scattered from a nickel crystal at different angles [Dav27]. Davisson was awarded the Nobel Prize for physics in 1937 for this work. With the advent of adequate vacuum generators and chambers, LEED became a standardized tool for surface analysis.

A LEED system is basically build up of an electron gun, accelerating and retarding grids, as well as an detector (luminescent screen). Figure 3.2 provides a sketch of the layout. When the primary beam hits the surface, its electrons are reflected on various crystal planes. This leads to interfering beams and eventually well-defined spots on the screen, naturally depending on the investigated sample.

By using a kinetic energy within the range of roughly 20 eV to 500 eV for the incident electrons, their mean free path can be estimated to a few atomic layers, making LEED a highly surface sensitive method. To quantitatively describe the interaction of an electron wave with a crystal lattice, it is straightforward to use the first Born approximation [Bor26].

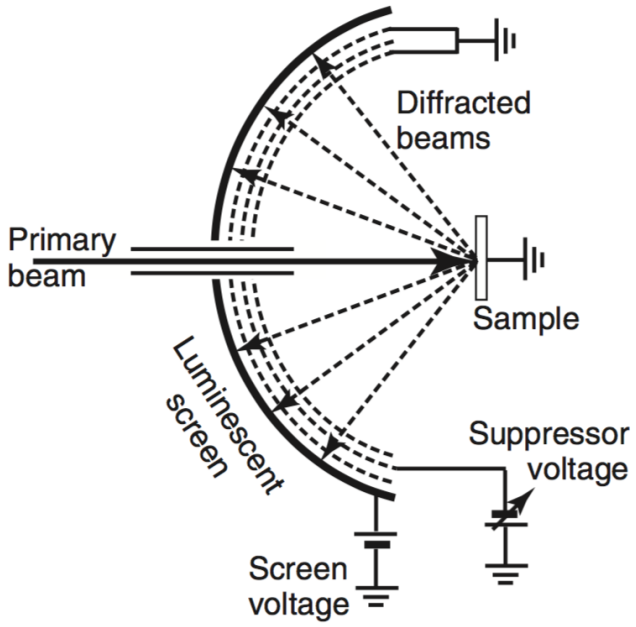

Figure 3.2: Schematic illustration of a three-grid LEED optics.
Reprinted figure from [Hei14] by permission of
WILEY-VCH Verlag GmbH & Co. KGaA, Copyright 2014.

The measured intensity I is the squared amplitude of the scattered wave

$$I\left(\vec{k}-\vec{k}_0\right) \sim \left| \int \rho(\vec{r}) \exp\left(-\mathrm{i}(\vec{k}-\vec{k}_0)\vec{r}\right) \mathrm{d}\vec{r} \right|^2$$

and thus the Fourier-transform of the density of scatterers ρ at position $\vec{r}$ with respect to the difference of the outgoing and initial wave vector $\vec{k}-\vec{k}_0$. If ρ is periodically like the lattice in a crystal, defined by a reciprocal lattice vector $\vec{G}$

$$\rho(\vec{r}) = \sum_{\vec{G}} \rho_{\vec{G}} \exp\left(\mathrm{i}\,\vec{G}\,\vec{r}\right) \quad ,$$

the symmetry is obviously broken at the surface and it is reasonable to use an Ewald-sphere [Ewa13] with reciprocal lattice rods to identify the reflexes in reciprocal space as depicted in figure 3.3. This construction is basically a visualization of the Laue equation, where a reflex occures if the difference of the initial and outgoing wave vectors equals a reciprocal lattice vector [Fri13]. Actually the intensity of a spot varies periodically dependent on the energy of the incident electrons due to their interaction with several crystal planes. Referring to figure 3.3 this is equivalent to rescaling the Ewald-sphere. For a

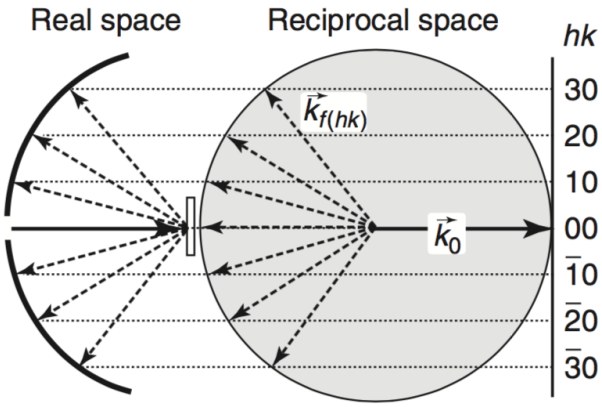

Figure 3.3: Ewald-sphere construction in reciprocal space and corresponding reflexes assigned to spots on the LEED screen. Reprinted figure from [Hei14] by permission of WILEY-VCH Verlag GmbH & Co. KGaA, Copyright 2014.

quantitative analysis of the spot intensity, a dynamic theory beyond the first Born approximation is needed, leading to so-called LEED I-V curves. Since the lattice factor (spot position) is sufficient to determine the quality of the prepared surface, the form factor (spot intensity) is neglected here. The theory solely treats elastic scattered electrons. To get rid of the inelastic compounds retarding grids are used to hold back secondary electrons.

Chapter 4

Experimental Setup

The basis for the experiments is a commercial surface analysis system from Scienta Omicron [Höv98], equipped with LEED optics and a low temperature STM. Custom-build parts like an electron bombardment heating stage and a cluster beam facility are also attached to this UHV system.

4.1 Surface Analysis System

The surface analysis system consists of two major components: a low temperature scanning tunneling microscope with options for sample storage and a preparation chamber with the possibility of performing high resolution angle resolved photoelectron spectroscopy, which was not used in the course of experiments within this thesis. The system is equipped with turbo-molecular pumps (details can be found in the appendix) for high gas loads especially at baking or sputtering. During STM operation only titan sublimation and ion pumps are used due to interfering vibrations caused by mechanical pumps. A detailed description of the operation can, for instance, be found in [Wut86]. Baking and pumping yields an ultra high vacuum (UHV) with a base pressure below $p_0 \leq 2 \cdot 10^{-10}$ mbar.
Transfer between various preparation and analysis positions is realized by a cryogenic 4-axis manipulator. Temperatures below 10 K, measured next to the attached LT sample holder, can be reached using a flow of liquid helium. The HB sample holder on the manipulator can be heated up to 900 K. Furthermore, sample surface cleaning is achieved by a sputter gun, operated with argon. The gas ions ablate contaminating atoms and molecules from the surface of a sample. Kinetic energies on impact are in the range of 1 - 2 keV. Samples, and STM tips likewise, can be prepared ex-situ and transferred to the manipulator by a load lock without breaking the vacuum.

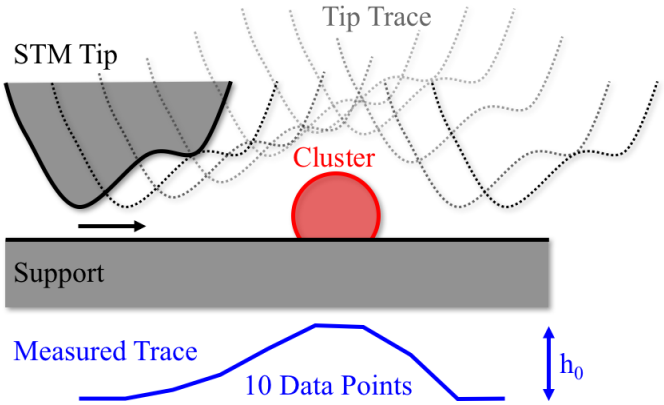

Figure 4.1: Actual geometry on the surface and measured height profile.

4.1.1 Low Temperature STM

The LT STM can be divided into three parts: the instrument itself, an inner radiation shielding and reservoir, which can be filled with either liquid helium (LHe) or liquid nitrogen (LN) and an outer shielding and reservoir, which is filled with LN. Temperatures of 5 K (LHe) respectively 77 K (LN) are achieved and held during measurement. The sample is kept in a fixed position, while the STM stage containing the tip is movable via piezoelectric coarse drive to reach any position on the sample surface. The scanner tube is carried out as a segmented piezo-element to address movement in x, y and z direction simultaneously.
The STM tip is usually made of a polycristalline tungsten wire with 0.1 mm in diameter, which is electrochemically etched and then transferred to the preparation chamber. Heating and sputtering procedures according to [Alb94] are applied afterwards. As mentioned before, using the load lock for tip exchange avoids additional baking of the system. Obtaining an apex radius of $r_a < 5\text{-}15$ nm is possible, but achieving a perfect sphere as assumed in chapter 3 seems slightly misleading. The atomic arrangement at the tip apex might have a substructure as depicted in figure 4.1. Since the geometric constitution of the tip also affects the resulting tunneling current, objects may not be imaged correctly regarding their lateral dimensions. A spherically shaped cluster potentially appears as an undefined island in the tip trace. However, the maximum height h_0 of such structures is conserved, assuming a minor influence of LDOS effects discussed in section 3.1.
To calculate an absolute height, the STM is operated in constant current mode. This means that the z position is governed by a control loop, targeting on holding the tunneling current at a specific value. In terms of the theory presented

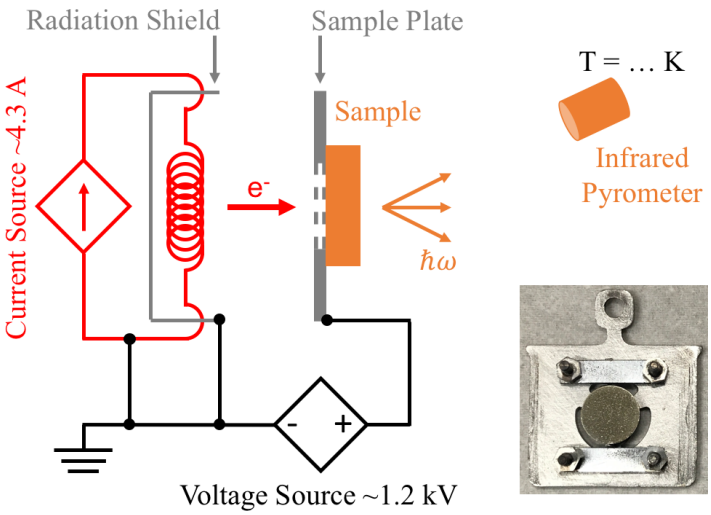

Figure 4.2: Schematic of the electron bombardment heating stage and photography of the mounted sample.

in chapter 3, the tip follows a surface area, where the LDOS of the sample is constant. The required voltage at the piezo-element then translates to an absolute height usually given in nm. This also implies that worse configured loops lead to artifacts in the resulting images.

4.1.2 Electron Bombardment Heating Stage

To retain a background pressure in the low 10^{-9} mbar regime during heating and oxidation procedures only the sample itself should reach high temperatures. This is best achievable with the impact of high energy particles, in particular electrons, on the sample backside. The custom-build electron bombardment heating stage is using a current-controlled tungsten filament, which generates free electrons via thermionic emission. A potential of $U_a \approx 1.2\,\mathrm{kV}$ between the sample and the filament accelerates electrons towards the sample backside. In order to avoid an increased temperature of the surrounding parts the area of the filament is shielded by a tantalum foil on the opposite side of the sample. The whole configuration is sketched in figure 4.2. As can been seen in the photography, the sample plate had to be adjusted to expose the sample backside, which is henceforth supported by only three legs. A special challenge is the accurate measurement of the sample surface temperature. A spot-welded thermocouple is ruled out due to the wired connection and hence mobility constraints within the UHV chamber. Another way is a pyrometric determination. This method relies on the concept of black-body radiation. Planck's law states that such bodies emit

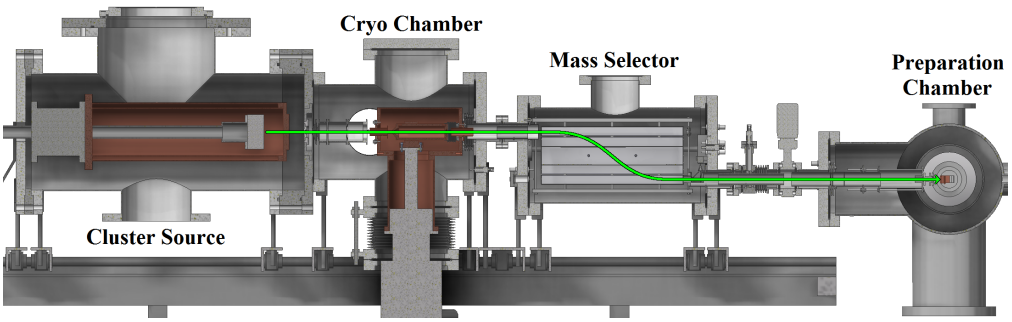

Figure 4.3: Cluster Beam Facility attached to the preparation chamber. A trajectory of the cluster beam is shown in green.

a specific spectrum depending on their temperature. Integrating the spectral radiance over all frequencies and the solid angle yields the Stefan-Boltzmann law

$$j^* = \sigma T^4 \qquad \sigma \equiv \frac{2\pi^5 k^4}{15 c^3 h^3} \tag{4.1}$$

with the Boltzmann constant k, the Planck constant h and the speed of light in vacuum c. The radiated power j^* is detected by an infrared pyrometer and converted to a temperature according to equation (4.1). Since the surface of the sample is not an ideal black-body j^* is multiplied by the emissivity $\varepsilon < 1$. This factor strongly depends on the material, the surface texture and even on the observation angle [Vol10]. Comparative measurements at various temperatures with a temporally spot-welded thermocouple yielded an emissivity of $\varepsilon = 0.28$ for the Ni_3Al sample.

4.2 Cluster Beam Facility

The Cluster Beam Facility (CBF) was developed in Freiburg in the group of Bernd von Issendorff [17a], who provided technical drawings of the system, which are used in this chapter[1]. The local setup in Dortmund was initially done by Thomas Irawan [Ira06] and Stefanie Duffe [Duf09]. Figure 4.3 shows the CBF attached to the preparation chamber of the surface analysis system. Three components are necessary to provide a charged beam of mass selected clusters. The respective functionality will be discussed in the following.

[1] Visualization was realized via Autodesk Inventor.

4.2.1 Magnetron Sputter Source

The cluster source utilizes magnetron sputtering and gas aggregation as it is described in detail in [Hab94]. The core part is a magnetron head with one central placed and 16 concentrically distributed permanent magnets, yielding a radial magnetic field of $B \approx 300\,\mathrm{mT}$ parallel to the head's surface. A target, usually a cylindrical metal plate of 1 - 3 mm thickness, is mounted onto the head. Within this thesis copper was used as target/cluster material. The magnetron head is biasable to a potential of typically $U_\mathrm{s} \approx 1\,\mathrm{kV}$. If now argon and helium gas is let in, an argon discharge can be ignited in front of the target. The high voltage accelerates argon ions towards the target surface, which remove atoms there by sputtering. Due to the magnetic field electrons are restricted to cyclotron orbits, increasing their dwell time in this region and thus the possibility of ionizing more argon atoms. Typical operating power of the magnetron drive ranges from 10 - 20 W. To stay well below the magnet's Curie temperature the backside of the source head is cooled with liquid nitrogen. The sputtered target atoms can now agglomerate to clusters in a helium and argon atmosphere, where helium ensures further cooling by collisions. Due to Penning ionization, i.e. the interaction of excited argon atoms with copper clusters

$$\mathrm{Ar}^* + \mathrm{Cu}_n \rightarrow \mathrm{Ar} + \mathrm{Cu}_n^+ + e^- \quad ,$$

a major amount of the clusters ($\approx 80\%$) is singly positively charged [Hab91]. The aggregation region can be mechanically extended or diminished, which shifts the cluster size distribution. Large clusters are rather produced within a large aggregation region and vice versa. Furthermore, the amount of gas also affects the initial size distribution. Typical flow rates are 200 sccm for helium and 100 sccm for argon[2]. To retain an acceptable pressure the source chamber is equipped with a $700\,{}^{\ell}/_{\mathrm{s}}$ turbo-molecular pump. The aggregation region is terminated by an adjustable diaphragm. Small apertures prolong the time clusters spend in the aggregation region and lead therefore again to larger clusters. Biasing the diaphragm slightly negative results in a preferred direction of movement towards the following parts of the CBF. Additionally a ring electrode, positioned after the aperture, yields an initial collimation of the cluster beam.

[2] A flow of 1 sccm indicates a gas volume of $1\,\mathrm{cm}^3$ under normal conditions ($T = 273.15\,\mathrm{K}$ and $p = 1013.25\,\mathrm{mbar}$) passing a certain point in 60 s.

4.2.2 Cryo Chamber

The entrance of the cryo chamber is carried out as a skimmer, which truncates the diffuse parts at the periphery of the ion beam. An array of four cylindrically shaped tubes, forming electrostatic lenses, lies past the skimmer. Their purpose is a collimation and acceleration of the beam, while the position in x and y is adjustable by further deflection electrodes. All following parts of the CBF, as they are not meant to deflect or focus cluster ions, are set to a floating potential of $U_\mathrm{f} = -500\,\mathrm{V}$. Residual gases within the cryo chamber are mainly helium and argon influxing from the cluster source. The pressure is improved by another turbo-molecular pump and additionally a cryo stage. The stage consists of cupreous surfaces connected to a cold head, which is cooled through adiabatic expansion of gaseous helium in a closed cycle. Temperatures of $T_\mathrm{i} \approx 10\,\mathrm{K}$ are measured at the inner surfaces while the outer shieldings reach $T_\mathrm{o} \approx 30\,\mathrm{K}$ [Ira06]. If an argon atom is adsorbed at these surfaces a desorption is not assumed until the temperature rises. However, this is not the case for helium. Finally, another focusing tube guides the cluster ion beam to the mass selector.

4.2.3 Mass Selector

Invented by Bernd von Issendorff and Richard Palmer, the mass selector makes use of a special time-of-flight principle described in [Iss99]. If the electronic control system is turned off, the beam passes straight through the interior parts of the chamber and hits a measurement electrode, which is used for a coarse optimization of the prior electrostatic lens system. The selection of specific particle masses is achieved via applying short voltage pulses between the plates of two capacitors, which are timed in a way that only the desired particles stay on trajectories as exemplary shown in figure 4.4. These particles are able to leave the chamber without perturbation while others collide with solid parts of the system. During the first voltage pulse, the cluster ions are accelerated for a time τ_p depending on the desired mass. All particles gain the same momentum but due to the size/mass distribution the velocities perpendicular to the initial direction of movement are different. Thus, after a drift period τ_d in a field-free region, the clusters have covered various distances according to their number of atoms. Now, a second voltage pulse, identical to the first one, is applied between the lower plate pair. All particles in this region are decelerated and regain the velocity components before entering the mass selector. This cycle is continuously repeated after a waiting time τ_w between two accelerating pulses. In order to gain maximum transmission τ_w should be set to the time that it takes to fill

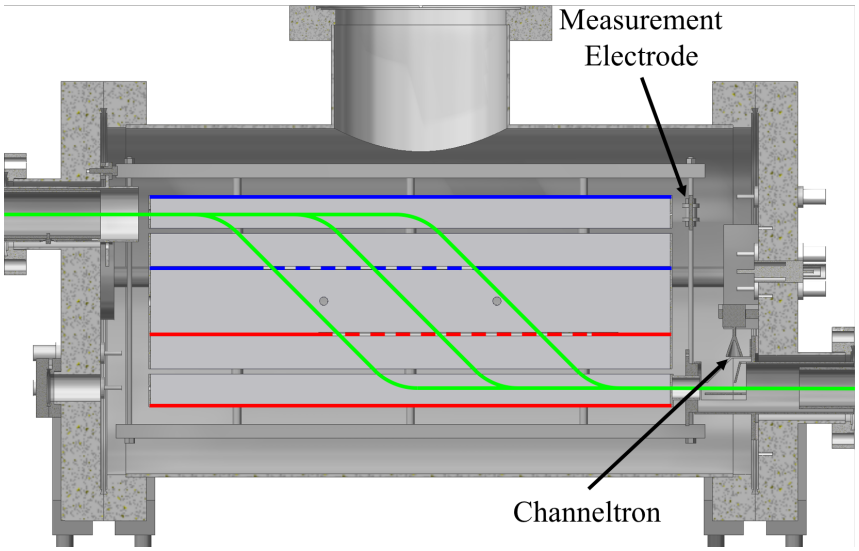

Figure 4.4: Drawing of the mass selector with trajectories of the mass selected beam emerging from left to right in green, the accelerating capacitor in blue and the decelerating plate pair in red. Dashed lines indicate openings covered by mesh to homogenize the electric field.

the space between the plates with new clusters. For testing purposes the cluster beam can be deflected upwardly beyond the exit by 90° to reach a channeltron used as electron multiplier. However, the clusters are usually detected within the preparation chamber with a Faraday cup. For practical application the characteristic times $\tau_{\mathrm{p,d,w}}$, which depend on the mass to be transmitted, are scaled with the help of a frequency generator. This allows the introduction of generalized times $t_{\mathrm{p,d,w}} = f(m) \cdot \tau_{\mathrm{p,d,w}}$, where a certain frequency corresponds to a specific mass. With fixed t_{p} and t_{d} trajectories of the selected clusters are identical for all masses. By tuning $f(m)$ it is possible to record a mass spectrum as shown in figure 4.5. For a few tens of atoms the clusters appear as isolated peaks in the spectrum. At higher masses these peaks broaden and clusters with a specific number of atoms can not be distinguished anymore. For the selection of Cu_{55} clusters in particular, the desired mass has to be extrapolated linearly from the measured spectrum of isolated peaks.
It is also possible to determine the quality of the selection by fitting gaussian distributions to the occurring maxima. For the spectrum depicted in figure 4.5 with $n = 23$ peaks a resolution of

$$\frac{m}{\Delta m} = \frac{1}{n} \sum_i \frac{x_{\mathrm{c},i}}{2\sigma_i} = 40.25$$

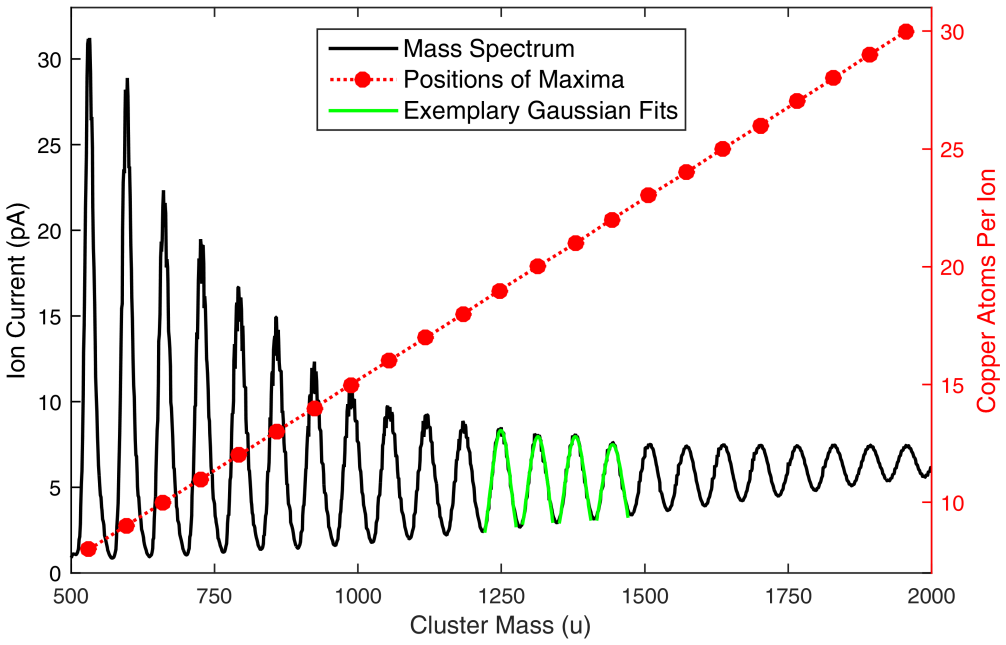

Figure 4.5: Mass spectrum of Cu_{55} clusters. The peak positions, obtained by gaussian fits, are linearly fitted to extrapolate for higher masses.

was obtained, where σ is the standard deviation (correlated to the peak width) and x_c is the position of the maximum. This corresponds to a selection error below 2.5 %. The resolution mainly depends on the exit aperture, which was chosen to be circular with an $r \approx 1.5\,\text{mm}$ radius in this setup[3]. But there is a conceptional problem with this kind of selection. If larger clusters than the desired ones are exactly $n \cdot \tau_d$ ($n \in \mathbb{N}$) in the field-free region they are parasitically decelerated with the subsequent smaller clusters. This issue is avoided by increasing the waiting time τ_w. Unfortunately, the transmission rate decreases concurrently. To address this problem the field-free region has to be cleared every time when decelerating the desired particles.

Improved Electronics

The parasitic selection is best visualized by optimizing the source to produce large clusters. If then selecting small clusters with low waiting times τ_w, a noticeable amount of large clusters is erroneously transmitted. In terms of figure 4.6 the broad peak at $m \approx 52000\,\text{u}$ is compressed and reproduced at $m \approx 17000\,\text{u}$ (black curve), which is in good agreement with theoretic calculations assuming a doubled

[3] $m/\Delta m = 68$ is optimally feasible using an exit aperture with $r \approx 1\,\text{mm}$ referring to [Ira06].

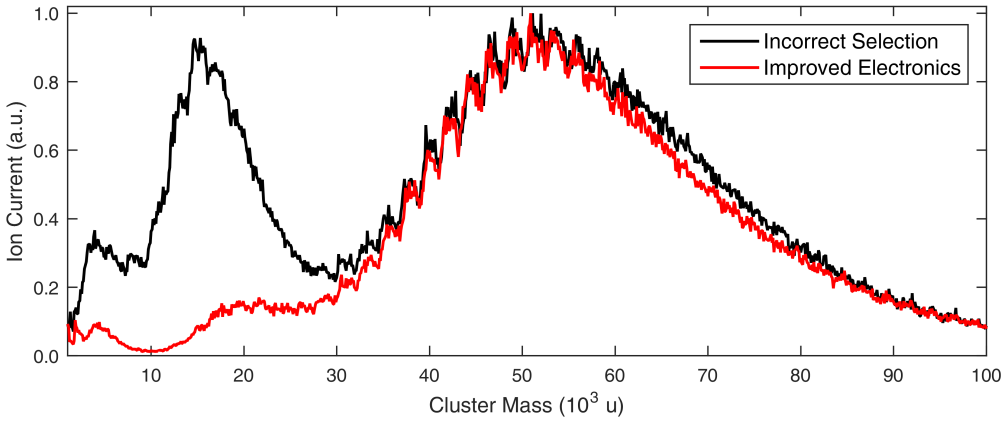

Figure 4.6: Mass spectrum of copper optimized for large clusters. Without "kicker"-electronics an incorrect selection occurs at smaller masses.

drifting time τ_d in the field-free region

$$\frac{m_\mathrm{parasitic}}{m_\mathrm{desired}} = \frac{2\tau_\mathrm{p}^2 + \tau_\mathrm{p}(\tau_\mathrm{d} + \tau_\mathrm{w})}{\tau_\mathrm{p}^2 + \tau_\mathrm{p}\tau_\mathrm{d}} \quad ,$$

yielding $m_\mathrm{parasitic} = 3\, m_\mathrm{desired}$ for $t_\mathrm{p} = 2$, $t_\mathrm{d} = 3$, $t_\mathrm{w} = 8$ and the corresponding $\tau_\mathrm{d,p,w}$ scaled according to the desired mass. In order to clear the field-free region simultaneously with the decelerating pulse another electrode is introduced to deflect clusters perpendicular to the drawing plane shown in figure 4.4. The necessary "kicker"-electronics were developed in cooperation with Philipp Gust and Thorsten Witt. Technical details can be found in the master's thesis of Philipp Gust [Gus18]. A deflecting potential of $U_\mathrm{d} = 73\,\mathrm{V}$, applied simultaneously with the decelerating pulse, is sufficient to cause the parasitic peak to vanish (see red curve in figure 4.6). It should be noted that the spectra in figure 4.6 were measured by using the channeltron in order to gain a stronger signal. However, the signal of a cluster impinging on the channeltron depends on its mass [Kre05].

4.2.4 Deposition Optics

Exiting the mass selector the beam is guided in an U_f-biased tube, followed by another x and y deflector to compensate for any imbalanced position of the beam. Two options, regarding focusing, are available to measure the cluster current with a Faraday cup or to deposit clusters on a substrate:

- Without focus lens, the deposition spot is roughly circular and about 3 mm in diameter. The distance between the last electrode of the CBF and the

sample respectively the Faraday cup amounts to several mm. Nearly all of the selected clusters are deposited respectively detected.

- With focus lens, the deposition spot shrinks to a $d \approx 1\,\text{mm}$ circle [Grö11]. This enables the deposition of multiple spots on the same sample. Furthermore, the distance between the focus lens and the sample decreases to 1 - 2 mm (depending on the sample). These well-defined deposition parameters are bought at the expense of losing intensity - only a fraction of the selected clusters is able to reach the sample or the Faraday cup.

Both options are available at any time since the lens is movable. The manipulator itself is biased during deposition to avoid the impact of clusters with high kinetic energy, which potentially leads to their deformation.
In the course of this thesis the resulting current after mass selection was increased by more than an order of magnitude as can be deduced from table 9.2 in the appendix. This was achieved by an optimization of the source parameters as well as all deflecting and focusing electrodes, but mainly of the lens array at the entrance of the cryo chamber.

Chapter 5

Sample Preparation and Characterization

This chapter is divided into two major topics. On the one hand, the preparation and properties of the oxide film are described in detail. The quality and suitability for cluster deposition is determined by STM as well as LEED. On the other hand, the deposition of clusters itself is addressed. Data visualization of STM measurements in the course of this thesis was realized via Gwyddion [Neč12].

5.1 Well-Ordered Oxide Layers

Preparation

The term oxide refers to a compound between a material and oxygen. Usually the oxidation takes place under uncontrolled conditions and leads to disordered oxide films at the surface of a bulk material. Otherwise, if these conditions are controlled carefully, it is feasible to obtain a long-range well-ordered oxide surface. An alloy crystal of nickel and aluminum has proven as an ideal substrate to form various phases of Al_2O_3 oxide [Fra96]. In particular the γ'-phase of Al_2O_3/Ni_3Al is of interest, since it exibits two superstructures [Ham06]. This phase can either be prepared by annealing an oxygen precovered $Ni_3Al(111)$ crystal to $T_a = 1000\,K$ or the oxidation directly takes place at $T_o = 1000\,K$ [Bec98]. The structure of the oxide depends on the mobility of the aluminum atoms [Ros99a], which naturally increases at higher temperatures. However, bare aluminum subtrates form amorphous Al_2O_3 layers upon oxidation [Flö15]. Especially Conrad Becker [17e] and co-workers put much effort in the determination of suitable oxidation parameters to obtain a long-range ordered γ'-Al_2O_3 film. He

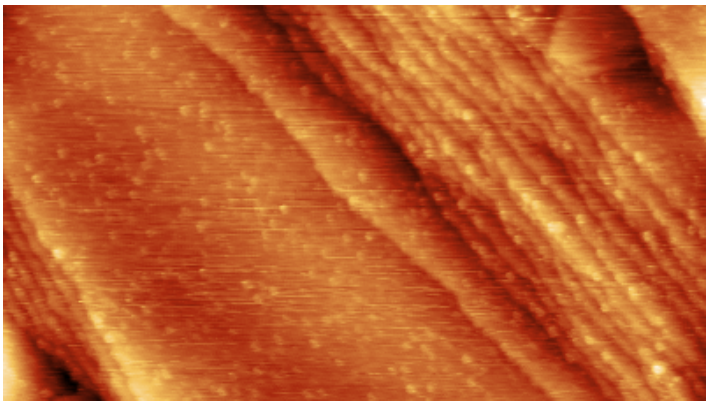

Figure 5.1: $Ni_3Al(111)$ surface after preparation and 24 h storage under UHV conditions. Parameters: $I_T = 160\,\text{pA}$, $U_G = 0.19\,\text{V}$, $(200 \times 112)\,\text{nm}^2$.

kindly provided the $Ni_3Al(111)$ crystal and a recipe for preparing the stated oxide structure on its surface.

Basically, the crystal is sputtered by Ar^+ ions with a potential gradient of 1.5 kV and a drained current of $I_s = 5\,\mu\text{A}$ to remove adsorbates and partially the oxide film. Afterwards, the sample is annealed to $T_1 = 1150\,\text{K}$. This temperature lasts for $t_1 = 7\,\text{min}$ before it is lowered to $T_2 = 1000\,\text{K}$ and again kept there for $t_2 = 7\,\text{min}$. In order to obtain a clean surface for oxidation the cycle should be repeated several times with decreasing time for sputtering. Since the $Ni_3Al(111)$ surface is quite reactive, the oxidation shall begin immediately after preparation. Figure 5.1 contains an STM image of the bare $Ni_3Al(111)$ substrate after 24 h storage under UHV conditions. A step bunching, characteristic for alloy crystals, is clearly visible as well as the presence of numerous adsorbates. A controlled oxidation is achieved by exposing the clean Ni_3Al surface to an oxygen (purity N4.7) atmosphere of $p_{O_2} = 3 \cdot 10^{-8}\,\text{mbar}$ at $T_o = 1000\,\text{K}$ for $t_o = 30\,\text{min}$. This corresponds to a dose of 40 L[4]. In order to relieve tension of the formed oxide film the temperature of the sample is increased to $T_f = 1050\,\text{K}$ without the presence of an oxygen atmosphere (flash). The procedure is then repeated once to gain a dose of 80 L. A complete set of the preparation cycle can be found in table 5.1. The time course of the different temperature regimes as measured by the pyrometer is shown in figure 5.2. The temperature graph of the oxidation (red curve) also contains a preparation cycle at the beginning and two flashing procedures after 30 min oxidation each. It should be noted that the kink, while initially ramping up the temperature, is caused by a changeover in the amount of scattered infrared light, generated by the incandescent filament, and the thermal

[4]Langmuir: $1\,\text{L} = 10^{-6}\,\text{Torr·s}$.

Action	Duration (min)	Parameters
Sputtering	60	5 µA, 1.5 kV
Heating	2 × 7	1150 K, 1000 K
Sputtering	45	5 µA, 1.5 kV
Heating	2 × 7	1150 K, 1000 K
Sputtering	30	5 µA, 1.5 kV
Heating	2 × 7	1150 K, 1000 K
Sputtering	15	5 µA, 1.5 kV
Heating	2 × 7	1150 K, 1000 K
Sputtering	10	5 µA, 1.5 kV
Heating	2 × 7	1150 K, 1000 K
Sputtering	5	5 µA, 1.5 kV
Heating	2 × 7	1150 K, 1000 K
Oxidation	30	1000 K, 40 L ($3 \cdot 10^{-8}$ mbar)
Flashing	5	1050 K
Oxidation	30	1000 K, 40 L ($3 \cdot 10^{-8}$ mbar)
Flashing	5	1050 K
Cooling	30	-
Flashing	10	1050 K

Table 5.1: Complete preparation cycle for γ'-Al_2O_3 on $Ni_3Al(111)$.

radiation emitted by the sample surface itself. A precise control of the surface temperature is indispensible for the final quality of the oxide film. By altering the potential U_a between sample and filament of the heating stage, it is possible to adjust the temperature within a range of $\Delta T = 1\,\mathrm{K}$. After 80 L oxidation and flashing the electron bombardment is switched off to let the crystal and the whole heating stage including the surrounding parts cool down in order to lower degas rates. Eventually adsorbed molecules and emerged tensions are removed with a final flash to $T_f = 1050\,\mathrm{K}$ for 10 min.

Characterization

An averaging characterization is achievable by LEED measurements. For the clean Ni_3Al surface the six-fold symmetry, depicted in figure 5.3(a), indicates a surface unit cell of fcc(111)-type with Al atoms in p(2 × 2)[5] arrangement. Regarding the 2d surface structure, each Al atom is surrounded by 6 Ni atoms in a hexagonal composition. Upon oxidation the spots become concentrically decorated with reflexes of the so-called network-structure. Figure 5.3(b) also

[5] Wood's notation for a primitive unit cell where the spacing between Al atoms is twice the spacing between Al (Ni) and Ni atoms.

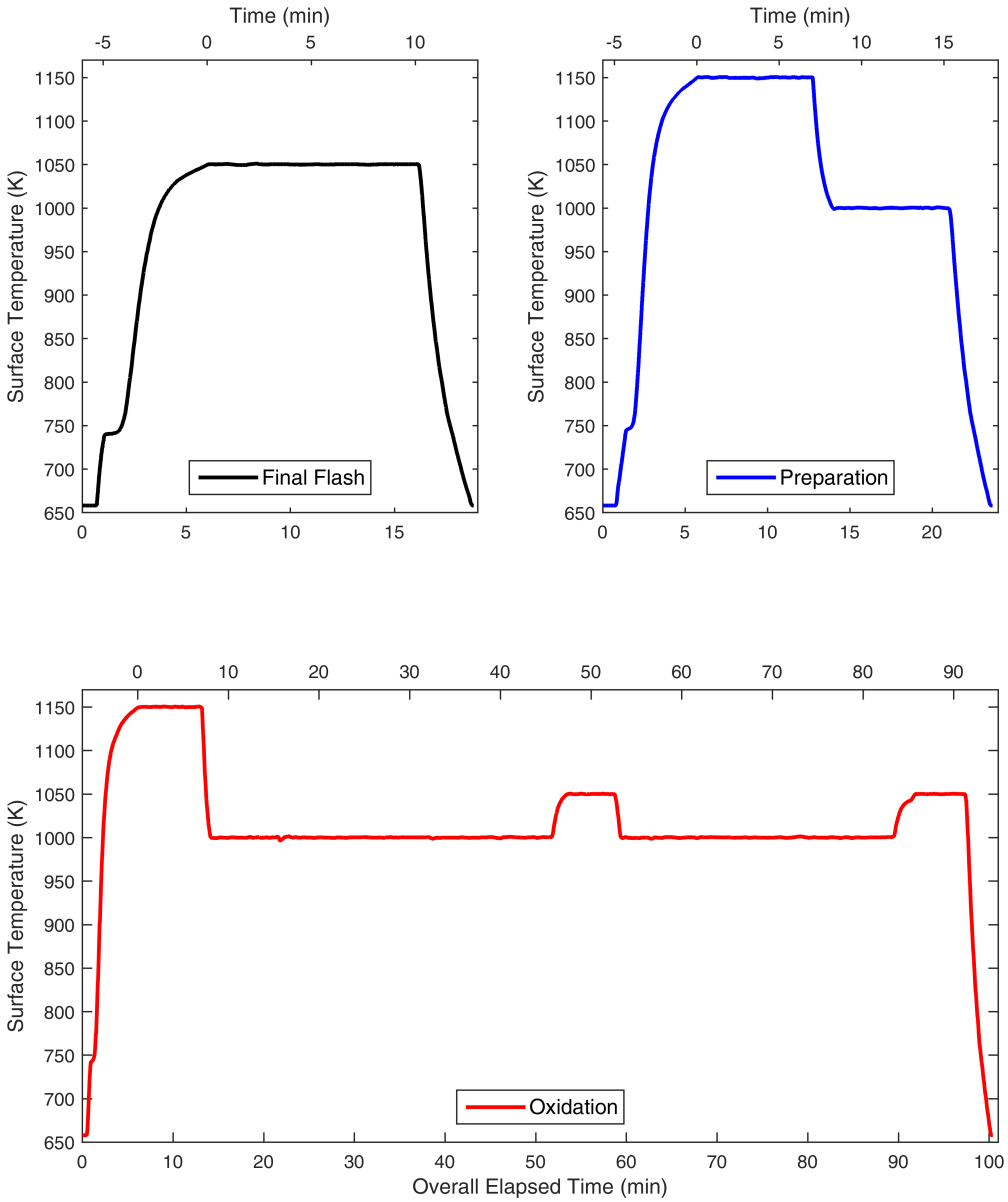

Figure 5.2: Surface temperature of the sample during various preparation procedures as provided by pyrometry. The upper axis starts with the reach of the final temperature, while the lower axis yields the overall elapsed time including the initial warming.

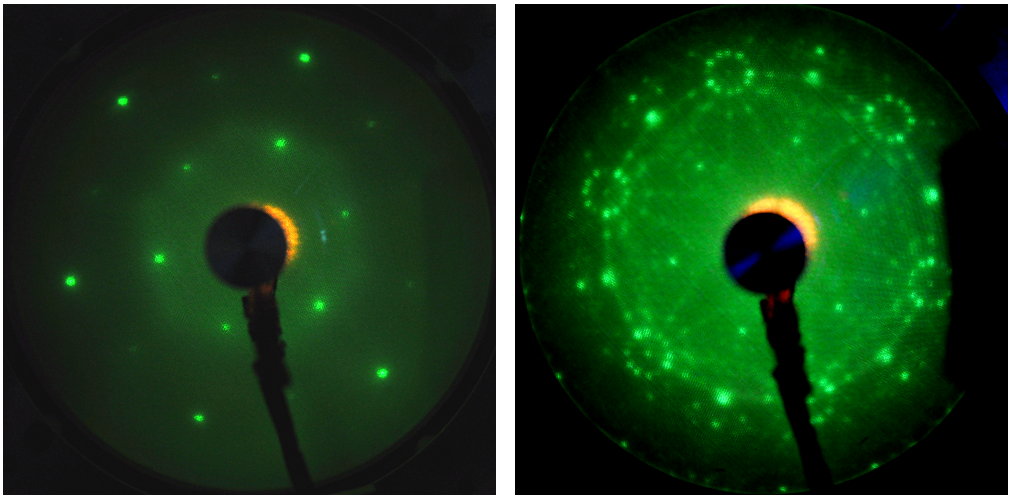

(a) Clean Ni_3Al. (b) γ'-Al_2O_3/Ni_3Al.

Figure 5.3: LEED images of the clean (a) and oxidized (b) Ni_3Al surface. Incident beam energy for both pictures was set to $E_i = 93\,eV$. Camera sensor exposure time was 30 s (a) respectively 60 s (b).

reveals the existence of two domains rotated by approximately 26.5°, which is in good agreement with SPA-LEED[6] measurements from literature yielding 24° [Deg05]. This emphasizes a long-range order of the oxide film.
Since the Al_2O_3 film is only about 5 Å in thickness [Bar92], it is feasible to perform STM measurements of the oxidized surface. The investigation took place at 77 K in order to reduce thermal drifting. An overview of the orientation of the bias dependent superstructures as measured by [Mar03] is given in figure 5.4, stating that the dot-structure is a $\left(\sqrt{3} \times \sqrt{3}\right)$ R30° subset of the network-structure. At tunneling voltages of $U_{Gap} = 3.2\,V$ the previously mentioned network-structure becomes visible. The corresponding constant current topography of the honeycomb-like lattice is shown in figure 5.5(b). Decreasing the tunneling voltage to $U_{Gap} = 2.0\,V$ while maintaining the frame position yields the so-called dot-structure, which is depicted in figure 5.5(a). Comparing both images, it is striking that the dot-structure is solely present if the network structure has sufficient order. Defect-rich terraces, like in the upper left corner of figure 5.5(b), exhibit no ordered structure at all. In order to determine the lattice factors of the two superstructures line profiles along ordered areas were taken as shown in figure 5.5(c). The data arise from two different domains to match roughly the fast scan direction of the STM (reduced influence of thermal drifting). While the unit cells of the superstructures are rotated by 30°, these domains are

[6]Spot Profile Analysis Low Energy Electron Difraction.

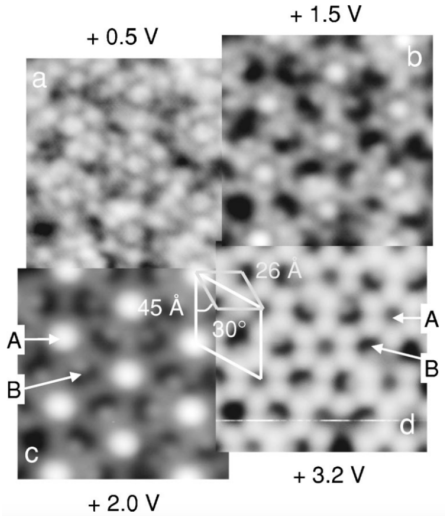

Figure 5.4: Bias dependent topography of γ'-$Al_2O_3/Ni_3Al(111)$. Parameters: $I_T = 100\,pA$, $(13 \times 13)\,nm^2$ each. Reprinted figure with permission from [Mar03]. Copyright 2003 by the American Physical Society.

	dot-structure	network-structure
Total length (nm)	16.24	26.11
Occurrences	4	11
Lattice factor (nm)	4.08	2.37
Literature [Deg05] (nm)	4.16	2.40
Difference to Literature	1.9 %	1.3 %

Table 5.2: Superstructure lattice factors compared to literature data obtained with SPA-LEED.

rotated by 24° resulting in an angle of 6° between the line profiles. The results, obtained by measuring the distance between the dashed lines, are presented in table 5.2. The small difference of $< 2\,\%$, compared to results obtained with SPA-LEED [Deg05], indicates a good calibration of the STM. By tuning the tunneling voltage in the range of $U_{Gap} = 0.5 \ldots 2.0\,V$ the corrugation of the dot-structure increases almost by an order of magnitude - this behavior unlikely arises from simple Moiré patterns, but indicates a local electronic state within the oxide film [Mar03]. Attempts to identify the origin of the dot-structure using STM, AFM and DFT[7] calculations lead to periodic point defects [Sch07], which could also explain the phenomenology of nucleation mentioned in chapter 1.
A comprehensive description of the Al_2O_3 properties can be found in [Deg06]. In a next step size selected clusters are deposited on the prepared oxide surface.

[7] AFM: atomic force microscopy - DFT: density functional theory

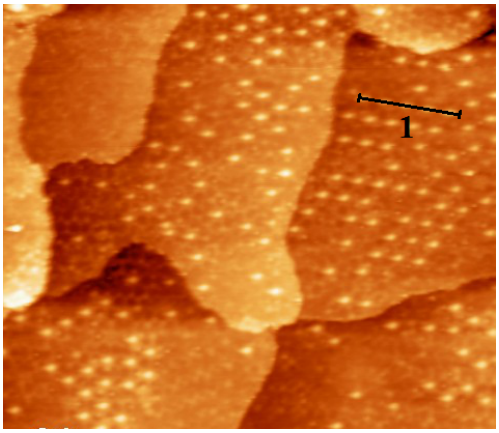

(a) Dot-structure including profile 1.

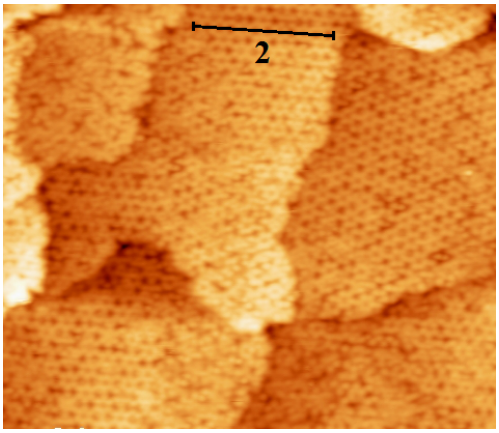

(b) Network-structure including profile 2.

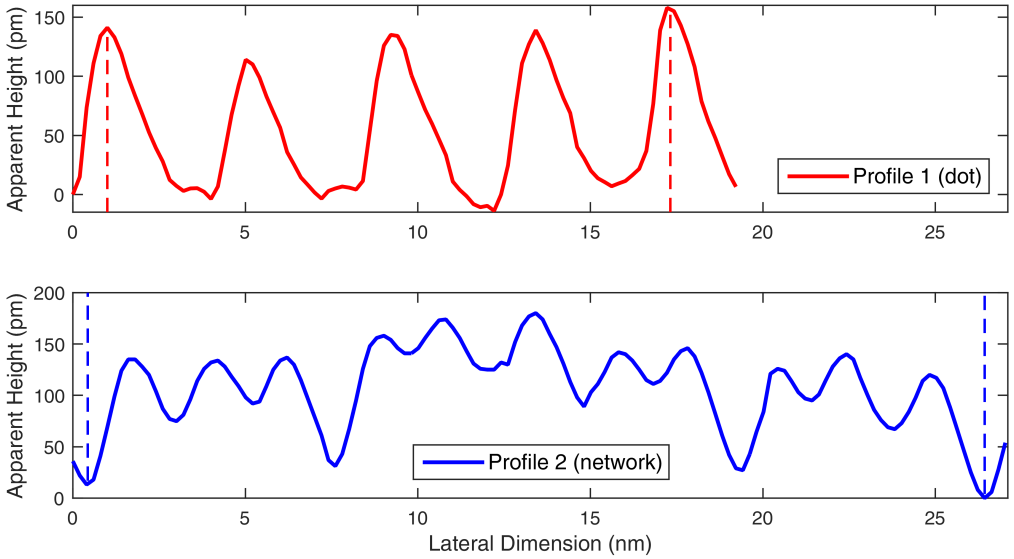

(c) Line profiles along dot- and network-structure

Figure 5.5: Investigation of the γ'-Al_2O_3 superstructures. Parameters for both STM images: $I_T = 90\,pA$, $(95 \times 82)\,nm^2$. (a) Dot-structure visible at $U_{Gap} = 2.0\,V$. (b) Network-structure visible at $U_{Gap} = 3.2\,V$. (c) Line profiles corresponding to (a) and (b) - the dashed lines indicate an averaging measurement of the respective lattice constant.

5.2 Cluster Deposition

Usually the deposition is done immediately after preparing the crystal without a further quality verification by STM, assuming a constant quality for identical preparation cycles. To improve reliability of the extrapolation process for cluster mass selection (see chapter 4) a new tool based on a C++ program and the open source software gnuplot [17c] was introduced. Firstly a recorded mass spectrum is loaded and smoothed by using the moving average method. This ensures an attenuation of the occurring spikes. The hereby generated mass spectrum is numerically derivated to find the positions of the maxima corresponding to single cluster masses. The algorithm only accepts peaks separated by the atomic mass of the cluster material with a certain tolerance. A linear regression, to deduce on higher cluster masses, is performed by matching these peaks to the number of atoms composing a cluster. To avoid an erroneous matching a deviation of ± 1 is taken into account during the linear fit. The correct matching is determined by the offset, which is typically slightly above zero. Additionally the offsets for ± 1 atom are provided in the output of the program. The points to be averaged, the atomic weight of the material, as well as the cluster sizes to be extrapolated can be specified on program start-up. The graphical output is automatically generated using gnuplot and depicted in figure 5.6 exemplary for copper clusters. Furthermore, a console output provides information about the slope and offset of the regression while simultaneously displaying the masses for the initial input of cluster sizes. Once the mass selector is adjusted for the desired clusters, the source parameters and deflecting/focusing voltages are optimized while monitoring the current, measured by the Faraday cup. Since every single cluster possesses a kinetic energy of roughly $E_{\mathrm{C}} = 500\,\mathrm{eV}$ on exiting the last aperture (which is approximately at floating voltage $U_{\mathrm{f}} = -500\,\mathrm{V}$, see voltages of aperture for experiment no. 2 and 3 in table 9.2), a suitable decelerating bias applied to the sample is necessary. The potential on the Faraday cup is therefore tuned from $-50\,\mathrm{V}$ to $50\,\mathrm{V}$, corresponding to "all clusters are detected" respectively "no clusters are detected". An adequate retarding potential is reached, if 80 % of all clusters are detected. The kinetic energy upon deposition lies then in the low eV regime per cluster. The procedure is visualized in figure 5.7. Depending mainly on the cluster size either a retarding potential or small accelerating potential is required. With this soft-landing procedure the structure of the clusters is preserved and the surface remains undamaged.

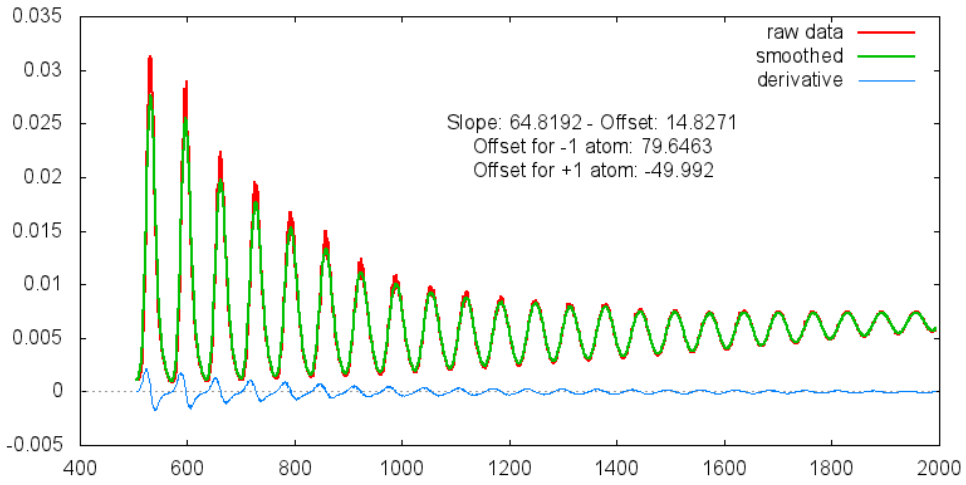

Figure 5.6: Graphical output of the introduced C++ program for reliable cluster mass extrapolation. The maxima belong to copper clusters starting with 8 atoms and ending with 30 atoms. Slope and offset of the regression are provided directly within the diagram.

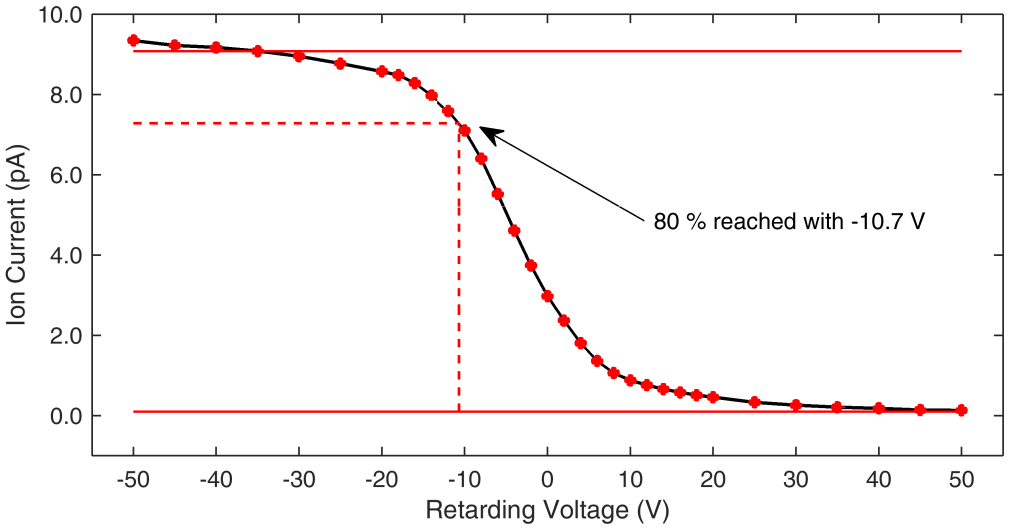

Figure 5.7: Detected Cu_{309} cluster current versus Faraday cup bias. In order to reduce kinetic energy upon impact a potential is used for deposition where 80 % of the initially detected clusters still reach the sample.

Assuming that each cluster is singly positively charged, a current of 1 pA equals $6.24 \cdot 10^6$ clusters per second. Depending on the cluster diameter (see equation 2.1) and the size of the deposition spot (see chapter 4),

$$n_{\mathrm{ML}} = \frac{\pi r_{\mathrm{Spot}}^2}{d_{\mathrm{Cluster}}^2}$$

clusters are needed to wet the surface with a monolayer equivalent[8]. Within this thesis only fractions below 3 % of n_{ML} were used to keep clusters separated and distinguishable in STM measurements. Due to the non-vanishing conductivity of the 5 Å thin oxide film, the positively charged clusters are neutralized after deposition.

[8]The calculation is valid for clusters forming a square lattice. In case of a hexagonal lattice $1/\cos(30°)$ more clusters are necessary for a monolayer equivalent.

Chapter 6

Results

This chapter contains the results for mass selected copper clusters deposited on γ'-$Al_2O_3/Ni_3Al(111)$. The nearest-neighbor distances of Cu_{13}, Cu_{55} and Cu_{309} are presented respectively as well as their apparent height, deduced from STM images, which was further studied by local height spectroscopy. In order to investigate effects on thermal stability of the deposited clusters incremental heating procedures up to 600 K for 45 min were applied. The nearest-neighbor distances for various frame sizes, coverages and cluster sizes are simulated by means of Monte Carlo methods to interpret the experimental data.
The different experiments and applied annealing steps are listed in table 6.1. The first experiment and first data analysis for cluster positions and height distributions for this experiment were carried out in cooperation with Raphael Floegel [Flo15]. All configurations were investigated immediately after deposition at $T = 77$ K. In order to perform the annealing steps the sample was removed from the STM stage and put either in the HB or the LT holder of the manipulator, which had already the final temperature to achieve a fast equilibration. After the stated time, the sample is cooled to 77 K again and reinserted in the STM. If indicated this procedures is repeated several times.

Experiment No.	1	2		3	
Cluster size (atoms)	55	309	55	13	55
Heating duration (min)	45	-		30	
Temperatures (K)	100, 200, 300, 400, 600	-		90, 95, 100	

Table 6.1: Applied heating procedures for copper clusters of various sizes. The deposited spots of the second experiment were only investigated at 77 K due to stability problems with the STM tip (see chapter 7 for further information).

Data Processing

After recording an STM image it is converted to an xyz-data file. Thus, an absolute height z is assigned to every position $\{x, y\}$ within a frame. In order to process this data with a perl script called "clusterizer", developed by Niklas Grönhagen [Grö11], all z values are fitted using a global plane, which is then subtracted from z. This compensates for the angle between tip trace, defined by x and y piezo actuators, and the sample mounting. The clusterizer provides a graphical output of the STM image and allows the selection of potential clusters by mouse click. Eventually, the height with respect to the surrounding substrate and the position of all selected clusters of a frame is written to a text file. This firstly enables the calculation of a local coverage

$$c = N \cdot \frac{d_{\text{cluster}}^2}{L^2} \quad , \tag{6.1}$$

where N is the number of counted clusters, d their estimated diameter (see equation 2.1) and L the lateral dimension of the (square) STM image. Although the coverage was chosen already during deposition, rather large variations are achievable by changing the position of the STM tip within the deposition spot, since the density of clusters decreases at the periphery of the spot. While an evaluation of the apparent height in terms of a histographic representation is directly feasible, the nearest-neighbor distances have to be deduced from the cluster positions. Therefore, a C++ program was written, which iteratively compares the distances from a certain cluster to all others of the frame and adds the smallest value to the mentioned text file. The nearest-neighbor distance strongly depends on the coverage. In order to compare various coverages a normalized distance d_{norm} in the form of

$$d_{\text{norm}} = \frac{d_{\text{real}}}{\sqrt{L^2/N}}$$

is introduced by scaling the measured distance d_{real}. Making use of equation (6.1) the normalized distance can be expressed through

$$d_{\text{norm}} = d_{\text{real}} \cdot \sqrt{c/d_{\text{cluster}}^2} \quad , \tag{6.2}$$

now depending on the coverage and the diameter of deposited clusters. The calculated value is also saved to file and can be visualized in a histogram.
For a broad comparability the coverages are distinguished in three categories.

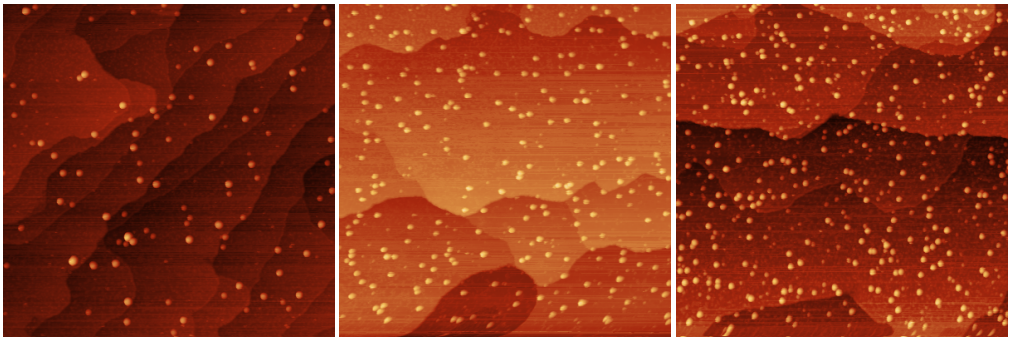

(a) Low (b) Medium (c) High

Figure 6.1: Examples of different coverage categories. Parameters: Cu_{55}, $I_T = 20\,pA$, $U_G = 1.8\,V$, $(200 \times 200)\,nm^2$. Deviating Parameters for (a): Cu_{13}, $I_T = 18\,pA$. Number of counted clusters: (a) 95, (b) 212, (c) 308.

These are exemplary shown in figure 6.1. It should be noted that the dot-structure is not simultaneously visible due to optimized tunneling parameters for cluster visualization. Moreover, the lateral dimensions of a cluster imaged by STM [Kly00] might exceed the lattice factor of the dot-structure. The direct observation of an alignment of clusters with the template structure is thus not possible. However, indicative methods like nearest-neighbor distances allow to analyse the cluster arrangement on the oxide film.

6.1 Nearest-Neighbor Distances

If every site of the dot-structure is occupied by a cluster, the measured nearest-neighbor distance is always the lattice factor of this structure ($a_{dot} = 4.16\,nm$). In a histographic representation a single peak would occur. If only a fraction of the dot-structure is occupied, the nearest-neighbor distance could also amount to subsequent sites with $d = \sqrt{3} \cdot a_{dot}$ or $d = 2 \cdot a_{dot}$ or even more, resulting in additional peaks in a histogram. However, a minimal distance of $d_{min} = a_{dot}$ is not undercut. In order to make use of this constraint the lattice factor a_{dot} must as well be normalized for various coverages. This is achieved by replacing the real distance d_{real} in equation (6.2) with the lattice factor a_{dot} to obtain $a_{dot,\,norm}$. Since the histogram bins should have a reasonable error[9], their width was chosen to be 0.05 normalized distances. In order to obtain a good visualization of the distance limit, defined by the normalized dot-structure lattice factor, the coverage categories are chosen according to table 6.2. The upper bound for high coverage

[9] Assuming a Poisson distribution, the error for each bin depends solely on the counted value for this bin $\Delta n = \sqrt{n}$.

Category	Low	Medium	High
Coverage range Cu_{309}	$< 0.47\,\%$	$0.47\,\%$ - $1.32\,\%$	$1.32\,\%$ - $2.59\,\%$
Coverage range Cu_{55}	$< 0.15\,\%$	$0.15\,\%$ - $0.42\,\%$	$0.42\,\%$ - $0.82\,\%$
Coverage range Cu_{13}	$< 0.06\,\%$	$0.06\,\%$ - $0.16\,\%$	$0.16\,\%$ - $0.31\,\%$
Color indicator	Red	Blue	Green
Normalized lattice factor	< 0.15	0.15 - 0.25	0.25 - 0.35
Characteristic $a_{\text{dot, norm}}$	0.15	0.25	0.35

Table 6.2: Quantitative categorization of various coverage ranges.

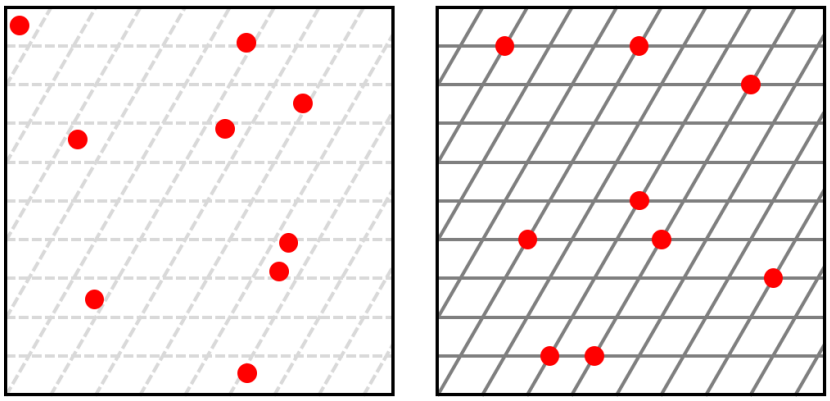

Figure 6.2: Exemplary sketch of possible cluster positions. Left frame: randomly arranged clusters (dashed grey lines as guide to the eye). Right frame: clusters aligned with the dot-structure, defined by a solid grid.

$a_{\text{dot, norm}} = 0.35$ is in accordance with the respective coverage maximum for the deposited cluster sizes. In order to increase the significance, the characteristic normalized lattice factor is set to the upper bound of the $a_{\text{dot, norm}}$-interval. Due to the square root dependence in equation (6.2) decreasing the coverage in the mentioned interval will not affect $a_{\text{dot, norm}}$ in the same extend. Distances below the characteristic limit are allowed for a coverage below that upper bound also for clusters on dot-sites, but if no distances below the limit occur, a strong indication for cluster alignment with the template structure is found. Considering low coverages, it is unlikely to find distances $d \leq a_{\text{dot, norm}}$ due to the large measured distances, regardless of whether the clusters are aligned with the dot-structure. A sketch concerning the arrangement of randomly distributed clusters and clusters aligned with the dot-structure is exemplary shown in figure 6.2. Regarding the random arrangement depicted in the left frame, only one distance smaller than the grid size is found for this rather low coverage. In the right frame clusters are restricted to grid positions. Without a grid as guide for the eye, positions in both frames seem random at first sight.

Histograms for the first experiment can be found in figure 6.3 and in figure 6.4 together with an expected distribution for a completely random arrangement f_{random} (see following section 6.2). The distribution was scaled in a way that its integral matches the counted occurrences. The dashed line indicates the limit given by the characteristic lattice factor. Due to the low temperature ($\approx 77\,\text{K}$) during deposition and thus a lower mobility, the clusters are expected to stick where they landed. This results in a roughly random distribution as can be seen in the histograms for 77 K. Especially for high coverages, the limit given by the characteristic lattice factor is undercut by far. During the first heating procedure the clusters gain energy to possibly snap on a dot-site. Further annealing to 200 K, 300 K, 400 K and 600 K for 45 min respectively seems to have no effect on the shape of the nearest-neighbor distributions. Unfortunately, after the last annealing step no images were recorded that fit medium coverages. To evaluate these distributions quantitatively the integral of the random distribution curve

$$\eta = \int_0^{a_{\text{char}}} f_{\text{random}}\left(d_{\text{norm}}\right)\,\mathrm{d}d_{\text{norm}}$$

from 0 to the respective characteristic lattice factor $a_{\text{dot, norm}} \equiv a_{\text{char}}$ is calculated and compared to the area of measured occurrences

$$\Gamma = \sum\nolimits_0^{a_{\text{char}}} \text{bin height} \cdot \text{bin width}$$

within these limits. The difference, normalized by η

$$\delta = \eta^{-1} \cdot (\eta - \Gamma) \tag{6.3}$$

can be regarded as an indication, if clusters are randomly distributed ($\delta = 0$) or, if distances below a_{char} are not present ($\delta = 1$). Figure 6.5 contains δ for different coverage categories plotted against the temperatures of the annealing steps. Deviations δ near to 1 represent a non-random arrangement in terms of occurrences below a_{char}, while small deviations can be identified with a random distribution, i.e. the appearance of distances below a_{char}. However, the histogram for 77 K at high coverages does not reflect a completely random distribution, since rather large distances are barely present. It is striking that the occurring maximum roughly matches a_{char}, indicating a local alignment of the clusters with the template structure. Otherwise, it seems misleading that only nearest-neighbor distances equal to a_{dot} are favored and not the subsequent ones like $\sqrt{3} \cdot a_{\text{char}} = 0.6$ and $2 \cdot a_{\text{char}} = 0.7$.

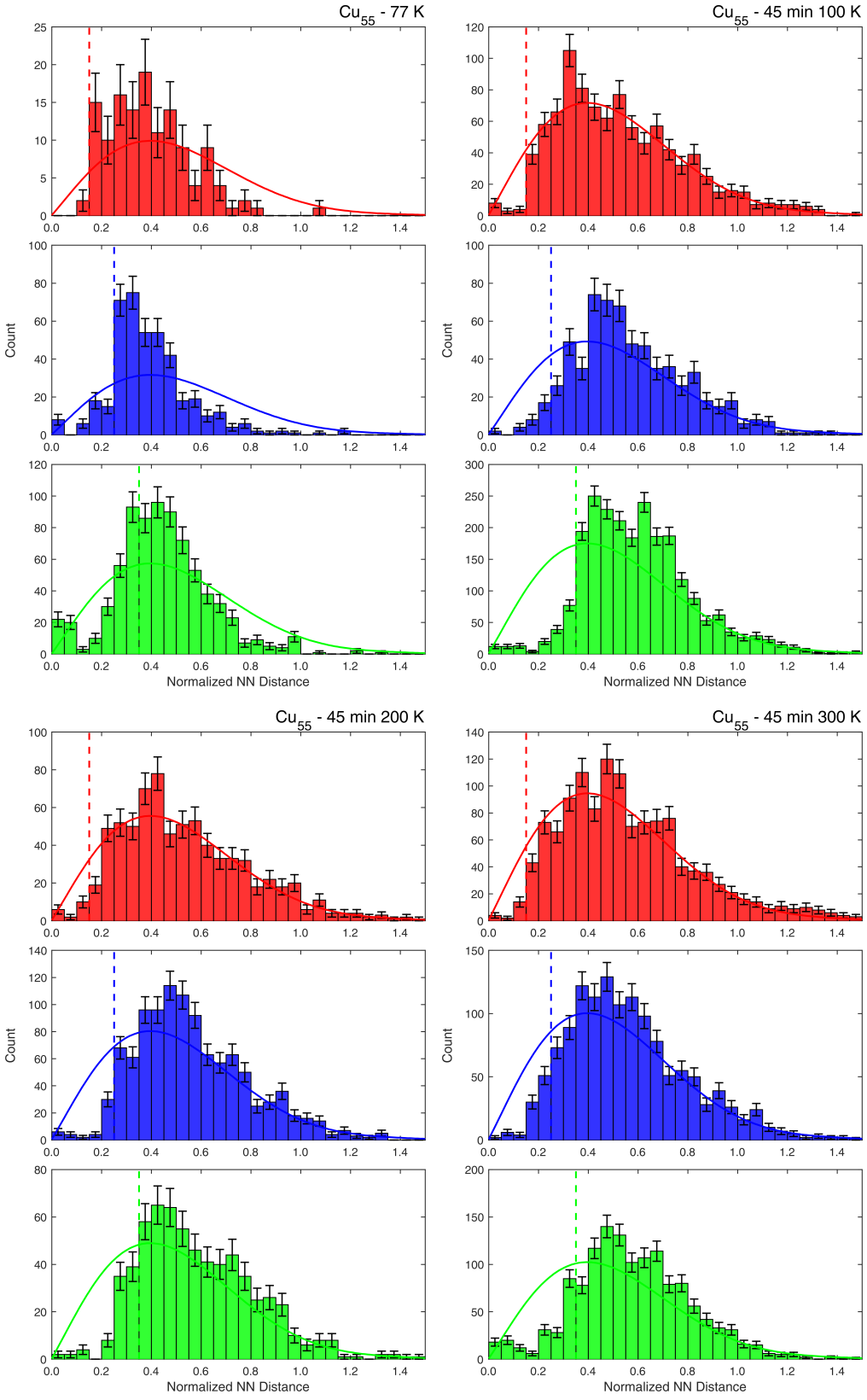

Figure 6.3: Normalized NN Distances for Cu_{55}, 1st experiment, 77 - 300 K.

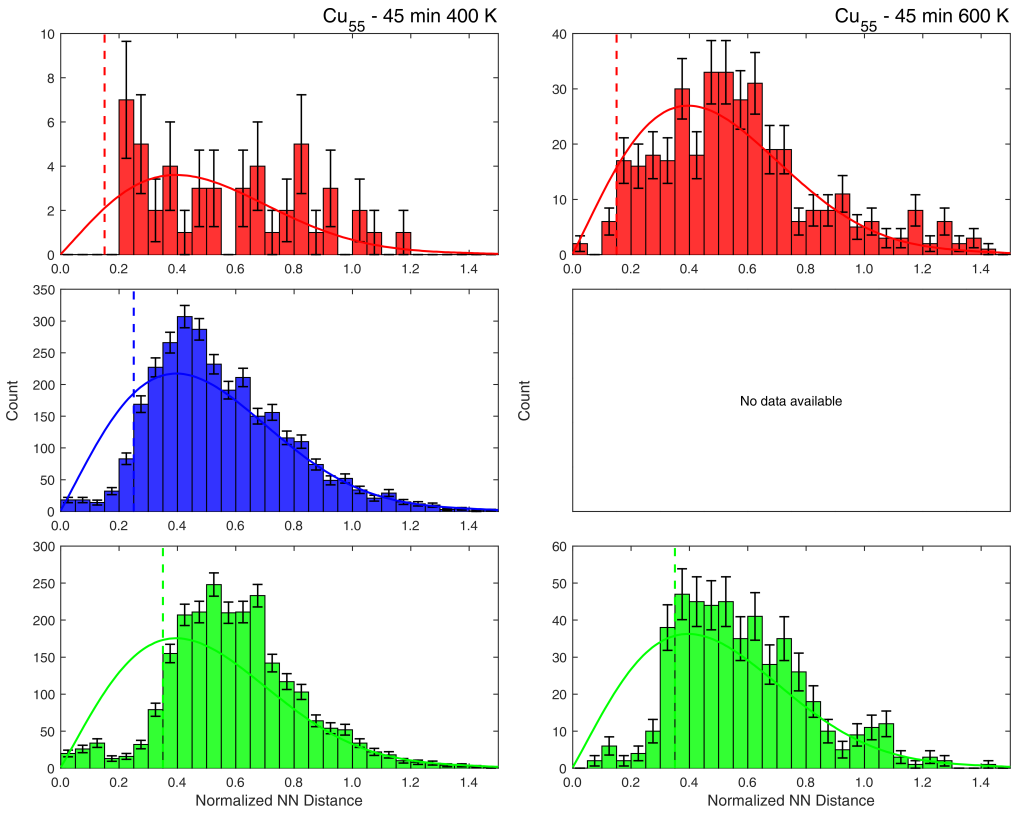

Figure 6.4: Normalized NN Distances for Cu_{55}, 1st experiment, 400 - 600 K.

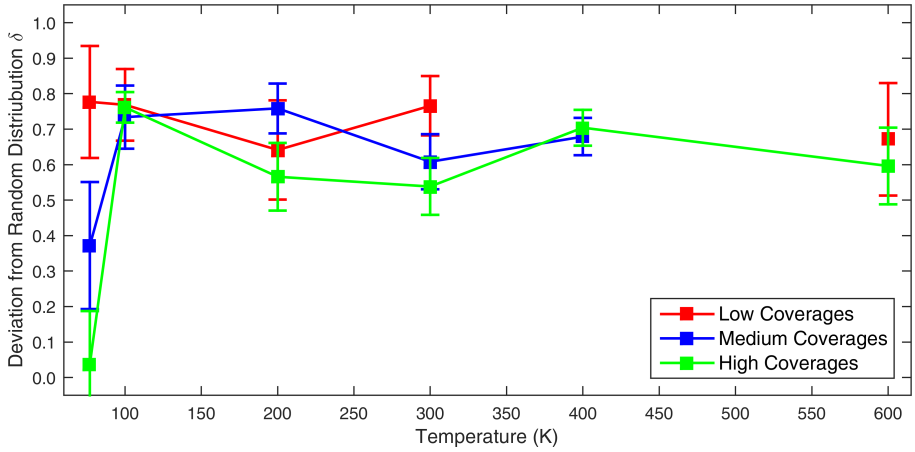

Figure 6.5: Deviations from random distribution for the three coverage categories, plotted against temperatures of the annealing steps for the 1st experiment.

The nearest-neighbor distributions for the second experiment are depicted in figure 6.6. No heating procedures were applied due to a stability problem with the STM tip. At 77 K the distributions for nearest-neighbor distances larger than a_{char} look mainly random for both, Cu_{55} and Cu_{309} clusters. A noticeable gap between f_{random} and the experimental data bins below a_{char} yields an initial alignment of both cluster sizes with the template structure. An evaluation of the deviation from a random distribution by means of equation (6.3) can be found in table 6.3. For low coverages of Cu_{309} no distances below a_{char} were found. The normalized deviation is thus 1 and no error can be assigned.

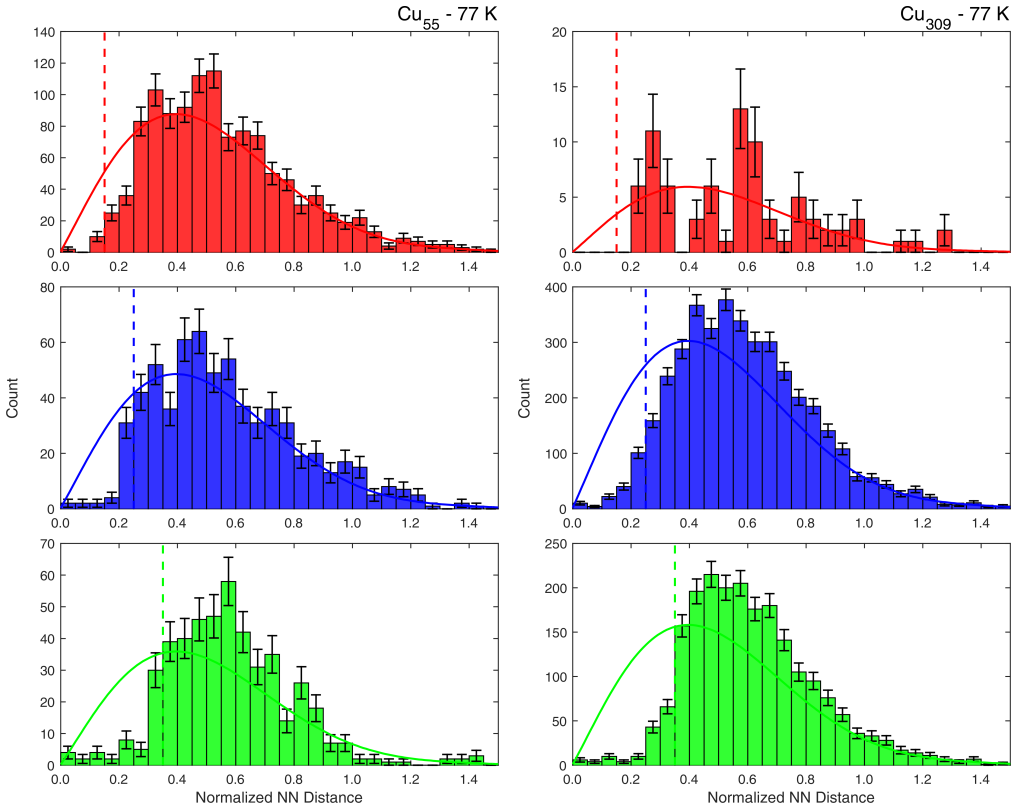

Figure 6.6: Normalized NN Distances for Cu_{55} and Cu_{309}, 2nd experiment.

Category	Low	Medium	High
$\delta\,(Cu_{55})$	0.85 ± 0.06	0.64 ± 0.10	0.64 ± 0.11
$\delta\,(Cu_{309})$	1.00	0.75 ± 0.04	0.79 ± 0.04

Table 6.3: Deviations from random distribution for the 2nd experiment. A graphical illustration is omitted due to the lack of annealing steps.

Cu_{13} clusters, deposited in the third experiment, are meant to be more mobile on the surface, hence an alignment with the template structure is more likely. Assuming that the alignment of Cu_{55} clusters in the first experiment happened during the first annealing step at 100 K, the annealing steps for the third experiment were chosen smaller in temperature and shorter in time in order to determine a threshold for this cluster size. The nearest-neighbor distances for Cu_{13} are depicted in figure 6.7. All histograms for nearest-neighbor distances larger than a_{char} look mainly random, but the edge below a_{char} is cut off. Drawing attention on the histograms for high coverages, the shape is nearly constant along the whole heating procedure and a majority of the deposited clusters are supposed to have already snapped on dot-sites. An overview of the introduced deviation from a random distribution δ is given in figure 6.9(a). Only the data for medium coverages after the first annealing step to 90 K is odd, but can be explained through poor statistics, i.e. insufficient cluster count for this histogram. This is also the case for low coverages after annealing to 90 K. For 95 K no data was found to fit low coverages. The data points in figure 6.9(a) are therefore omitted.
The results concerning the normalized nearest-neighbor distances for the third experiment with Cu_{55} clusters are shown in figure 6.8. Again, low coverages are associated with poor statistics due to insufficient occurences. The remaining histograms are yielding random distributions with a small amount of distances below a_{char}. A comparison between the measured distances and the random distribution in the interval $[0, a_{\mathrm{char}}]$ can be found in figure 6.9(b). As in figure 6.9(a), two data points for low coverages were omitted here due to the lack of experimental data in the mentioned interval.

For all histograms the maximum is shifted slightly to higher distances compared to the expected random distribution f_{random}. This implies at least a certain order of the deposited clusters. In order to obtain distinguishable peaks in a histogram a large amount of clusters has to be deposited. On the other hand, large amounts lead to cluster coalescence, even during deposition. Furthermore, for obtaining height distributions, it is indispensable that clusters are imaged isolated in order to determine their apparent height with respect to the oxide. Thus, a characterization using the STM is hardly feasible. However, a simulation of high coverages is possible by using Monte Carlo methods.

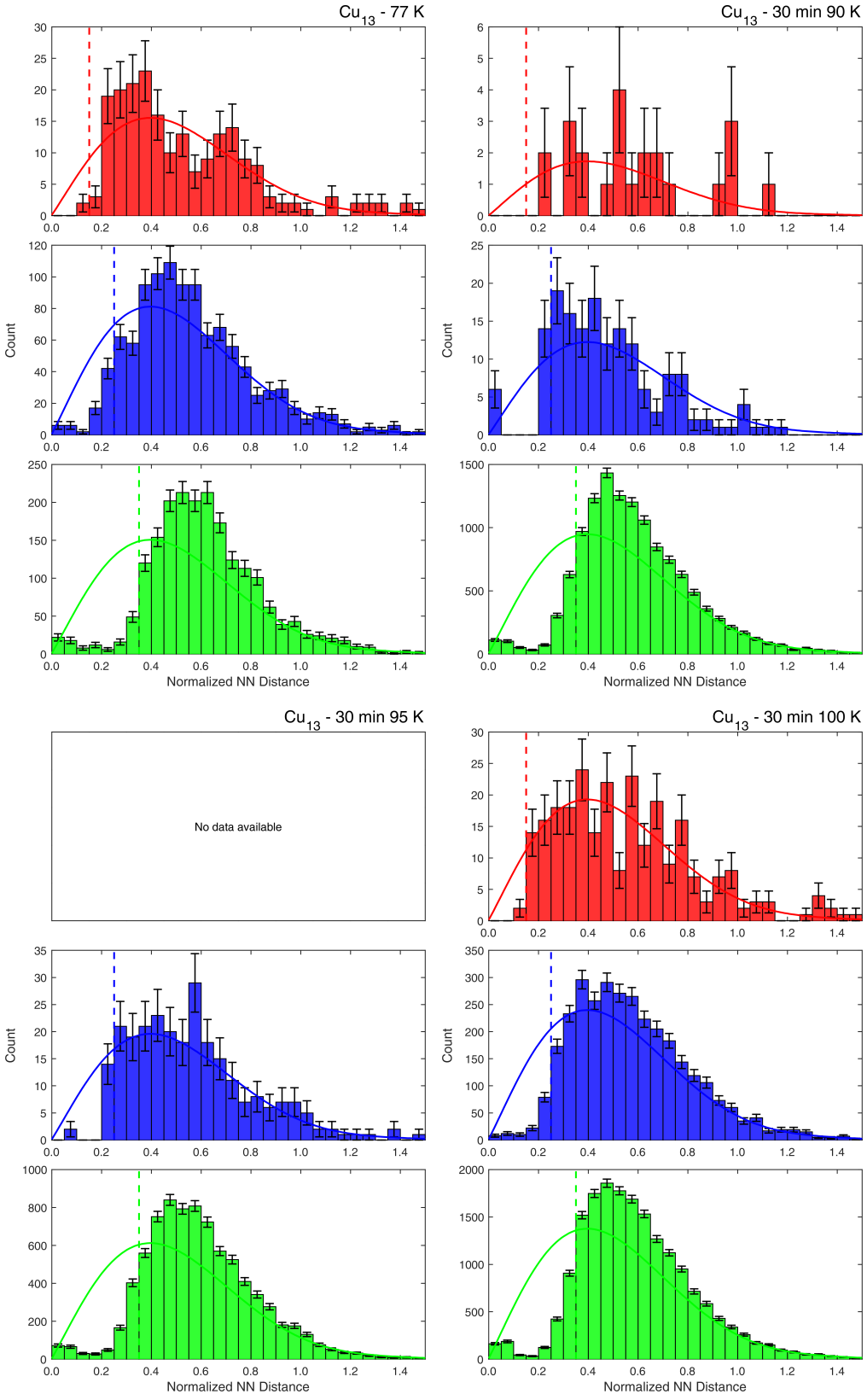

Figure 6.7: Normalized NN Distances for Cu_{13}, 3rd experiment, 77 - 100 K.

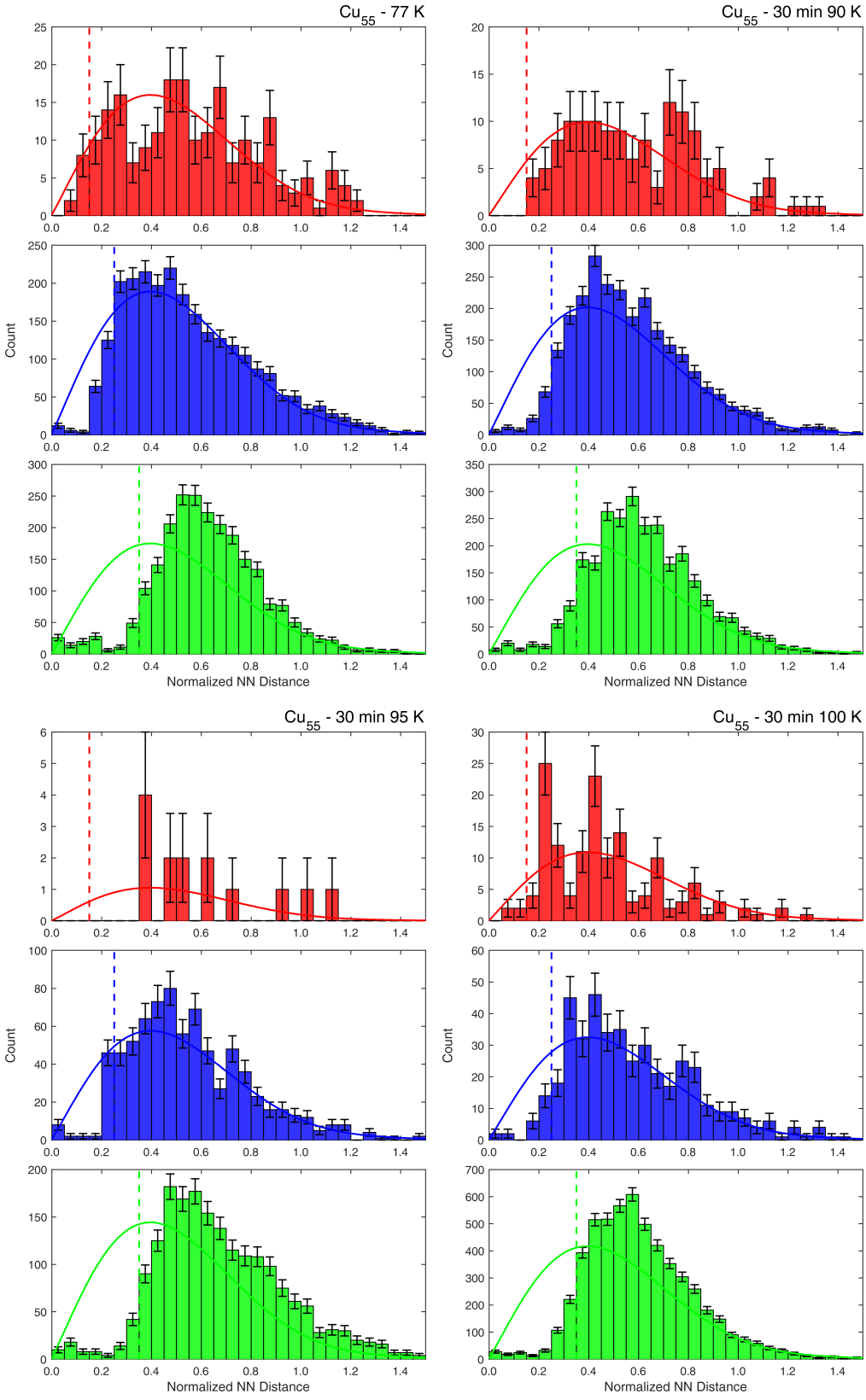

Figure 6.8: Normalized NN Distances for Cu_{55}, 3rd experiment, 77 - 100 K.

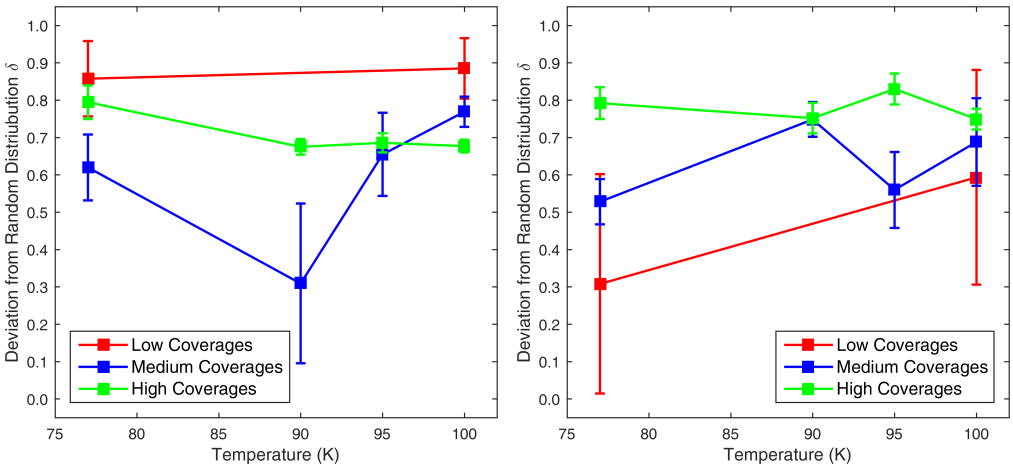

(a) $\delta(T)$ for Cu_{13}. (b) $\delta(T)$ for Cu_{55}.

Figure 6.9: Deviations from random distribution for the three coverage categories, plotted against temperatures of the annealing steps for the 3rd experiment.

6.2 Monte Carlo Simulations

Monte Carlo (MC) methods are well known and applied in physics as they enable the solution of problems through random processes. In this thesis the nearest-neighbor distributions of clusters on γ'-Al_2O_3/Ni_3Al are investigated using Monte Carlo methods. The developed C++ source code of the used simulation program can be found in the appendix.

A random distribution is obtained by generating cluster positions $\{x, y\}$ within an STM frame of a certain size. The nearest-neighbor distances are extracted and normalized. Iterating this process with many frames yields a statistical resilient distribution (law of large numbers). The coverage c, the frame size L and the cluster diameter d_{cluster} are adjustable. The latter is necessary to calculate the number of clusters within a frame on the basis of the coverage according to equation (6.1). Since the positions have no lateral dimensions, even coalesced clusters are captured. Figure 6.10 contains such a random distribution for Cu_{55} clusters with 1.0 % coverage of a monolayer equivalent. The amount of coalesced respectively agglomerated clusters ($d_{\text{real}} \leq d_{\text{cluster}}$) is marked by a dotted area. For small normalized distances, the curve may be approximated linearly to estimate the number of coalesced cluster, as described in [Sie07]. A total of 27.7 million cluster positions were investigated for this certain histogram. The bin width was chosen to be 0.01 normalized distances, hence a line plot is reasonable. A polynomial of 7th degree is fitted to this curve in order to obtain the random distribution function f_{random}, mentioned in the previous section.

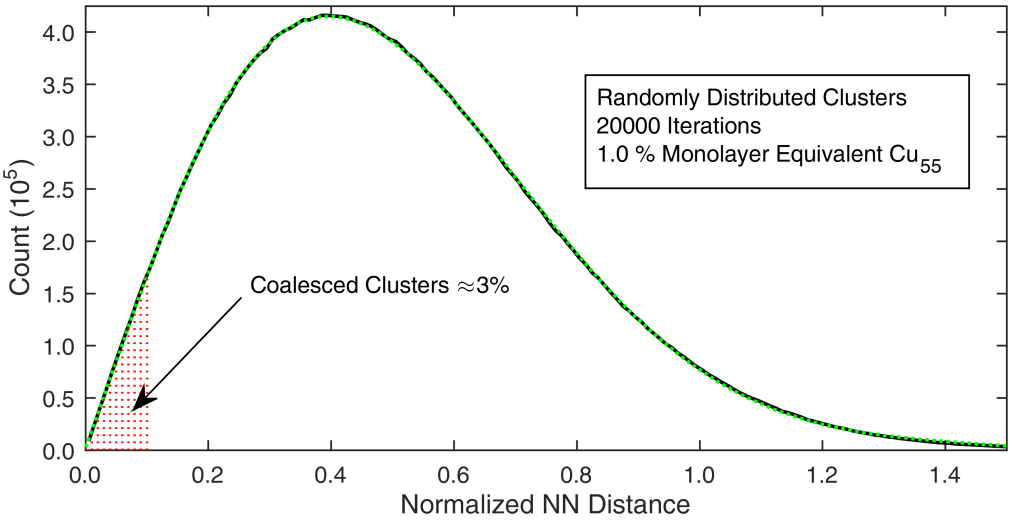

Figure 6.10: Random NN distribution for Cu_{55} clusters, obtained with a Monte Carlo simulation. The green curve denotes a polynomial fit to the data.

The (adjusted) coefficient of determination amounts to $R^2 = 0.99993$ yielding an appropriate representation of the MC obtained data. The shape of the curve is furthermore in good agreement with an analytically deduced expression for circular frames [Kno02].

In order to draw conclusions on non-random distributed clusters, for instance clusters aligned with the template structure of γ'-Al_2O_3/Ni_3Al, the introduction of a lattice is required. The simulation was thus modified to constrain cluster positions on grid points, defined by the hexagonal dot-structure. The number of available sites per frame is calculated through $N_{\mathrm{dot}} = {}^{L^2}/_{a_{\mathrm{dot}}^2} \cdot {}^{1}/_{\cos(30°)}$, while the surface is wetted by a monolayer equivalent if $N_{\mathrm{ML}} = {}^{L^2}/_{d_{\mathrm{cluster}}^2}$ clusters are deposited. Thus a fraction of

$$\frac{N_{\mathrm{dot}}}{N_{\mathrm{ML}}} = \left(\frac{d_{\mathrm{cluster}}}{a_{\mathrm{dot}}}\right)^2 \cdot \frac{1}{\cos\left(30°\right)}$$

of a monolayer equivalent is sufficient to occupy the entire number of dot-sites. The coverage limits for the investigated cluster sizes are: $c\,(\mathrm{Cu}_{13}) = 3.0\,\%$, $c\,(\mathrm{Cu}_{55}) = 7.7\,\%$, $c\,(\mathrm{Cu}_{309}) = 24.4\,\%$. All simulations above these limits will solely lead to a single peak at $a_{\mathrm{dot,\ norm}}$ in a histographic representation. The program is not capable to treat multiple occupation of grid points, although this could happen if clusters coalesce. The validation whether this fact influences the obtained distributions for lower coverages leads to a well known stochastic question: the coupon collector's problem [Fla92]. If there is a set of n different

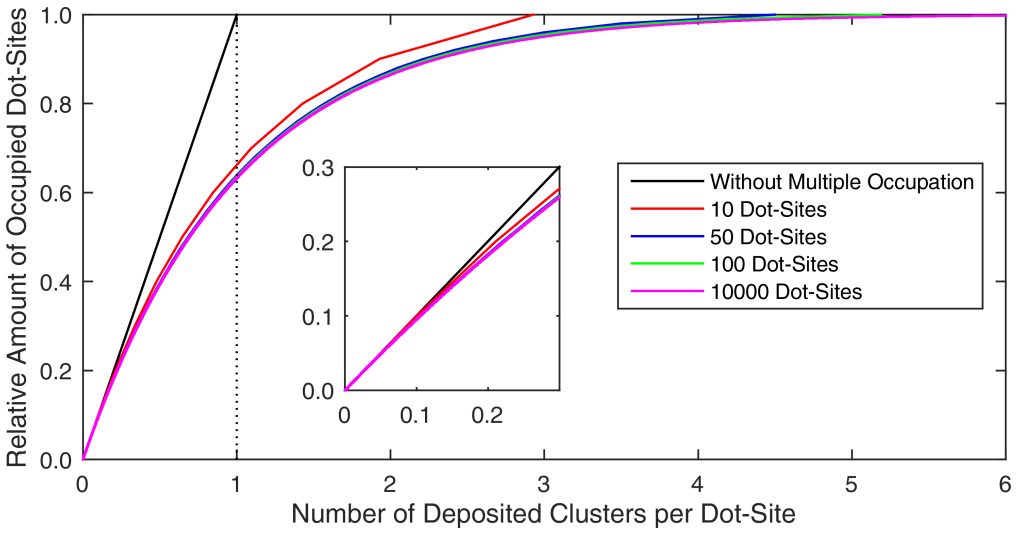

Figure 6.11: Comparison of the used MC simulation with a model concerning multiple occupation per dot-site.

coupons, how many draws of a single coupon are needed to gather all coupons? If the coupons are not replaced after every draw, the answer is trivial (n draws) - this represents the procedure of the used MC program: the entire n dot-sites are occupied once n clusters are deposited. If the coupons are replaced after every draw, the probability of getting a new one is

$$p_i = \frac{n-(i-1)}{n} \quad ,$$

where $i-1$ denotes the amount of already collected coupons. The mathematical expectation of draws to get the ith coupon simply is p_i^{-1}. Making use of the linearity of expectations, all n coupons are gathered after

$$E_n = \sum_{i=1}^{n} p_i^{-1} = n \cdot \sum_{i=1}^{n} \frac{1}{n-i+1} = n \cdot \sum_{j=n}^{1} \frac{1}{j} = n \cdot H_n$$

draws on average, where H_n is the nth harmonic number. Thus, x different coupons are averagely collected after $E_x = n \cdot (H_n - H_{n-x})$ draws. In terms of the initial MC simulation problem, the average number of clusters on a single dot-site is $H_{N_{\mathrm{dot}}} - H_{N_{\mathrm{dot}}-N_{\mathrm{dot,\ occupied}}}$. Iterating the number of occupied dot-sites $N_{\mathrm{dot,\ occupied}}$ yields the data shown in figure 6.11. Without multiple occupation, all sites are occupied with a single cluster. Allowing multiple occupation, it takes more clusters to occupy all sites. For coverages below 10 % of all dot-sites (see inset in figure 6.11) the simulation model is consistent

with the stochastically obtained data. It should also be noted that only the mathematical expectation is considered - like for all statistic processes, there are scenarios in which the entirety of sites would never be occupied, even after a large number of deposited clusters per dot-site.
Parameters for the following MC obtained nearest-neighbor distributions for clusters aligned with the dot-structure are:

- Cluster size: Cu_{55}, since it fits most experimental data in this thesis. Altering the coverages for other sizes leads to the same histograms.
- Frame size: $300 \times 300\,\mathrm{nm}^2$, since most STM images were recorded with an edge length of 200 - 400 nm and boundary effects are neglectable using this range.
- Iterations: the number of frames was chosen dependent on the previous parameters and the coverage to gain some 20 million clusters for a single histogram.

In figure 6.12(a) the nearest-neighbor distribution in the limit of occupation of all dot-sites ($c = 7.7\,\%$) is depicted. As predicted, a single maximum at $a_{\mathrm{dot,\ norm}}$ arises[10]. Figure 6.12(b) contains the same distribution, but the coverage was chosen to be $c = 1.0\,\%$ of a monolayer equivalent. Now, subsequent distances above $a_{\mathrm{dot,\ norm}}$ are present. Shoulders to the local maxima partially appear due to the random character of the simulation. If the number of clusters per frame is lower then expected through the coverage, the normalized distances are also lower even if the real distances are the same. These are examples for extreme parameters with regard to the coverage and should be treated with caution due to the limited validity caused by single occupation of dot-sites.
Distributions closer to the coverages as studied experimentally in the course of this thesis are shown in figure 6.13. For a rather low coverage of $c = 0.08\,\%$, as depicted in figure 6.13(a), the shape of the distribution seems mainly random. The existence of a few distances below $a_{\mathrm{dot,\ norm}}$ can again be explained through the random character of the simulation. Furthermore, the deviation ($\delta = 0.89$) from an ideal random distribution f_{random} is in good accordance with the experimental data for low coverages if sufficient statistics are given. Figure 6.13(b) shows the nearest-neighbor histogram for clusters aligned with the hexagonal dot-structure and a medium coverage of $c = 0.32\,\%$. Obviously, the experimental data for this coverage category does not match the histogram

[10] $a_{\mathrm{dot,\ norm}} = 1.07 \neq 1$ due to normalization on the basis of a square lattice.

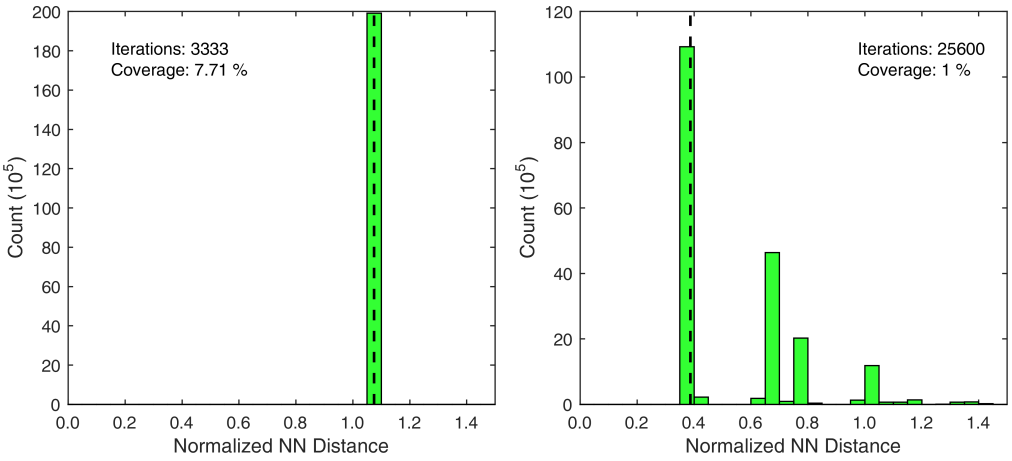

(a) NN distribution for $c = 7.7\,\%$.

(b) NN distribution for $c = 1.0\,\%$.

Figure 6.12: Through Monte Carlo methods obtained nearest-neighbor distributions for extreme coverages.

obtained through the Monte Carlo simulation. A global maximum at $a_{\text{dot, norm}}$ arises, while for large normalized distances a transition to a random distribution is roughly visible. The shape of the histogram for high coverage ($c = 0.64\,\%$), presented in figure 6.13(c), is nearly identical to the simulation for $c = 1.0\,\%$. The shoulders to the local maxima are more distinct due to the fewer clusters per frame and tendentially higher fluctuations of this number.
However, the histograms obtained for medium and high coverages are far from the experimental data. This may be explainable by terraces exhibiting no dot-sites or rapidly alternating domains.

The mentioned heating procedures potentially lead to cluster coalescence or ripening, therefore the height distributions of deposited clusters, before and after annealing, are of particular interest. The apparent height of clusters on γ'-$Al_2O_3/Ni_3Al(111)$ shows a strong dependence on the applied tunneling voltage [Deg04]. In order to interpret the height histograms properly spectroscopic measurements are indicated.

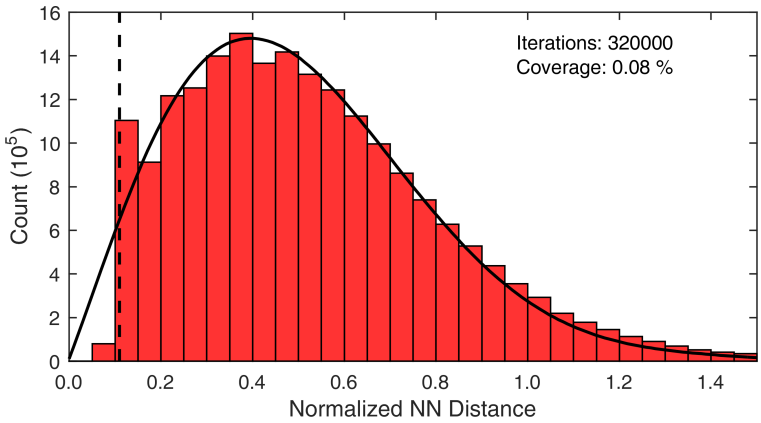

(a) Low coverage, $c = 0.08\,\%$.

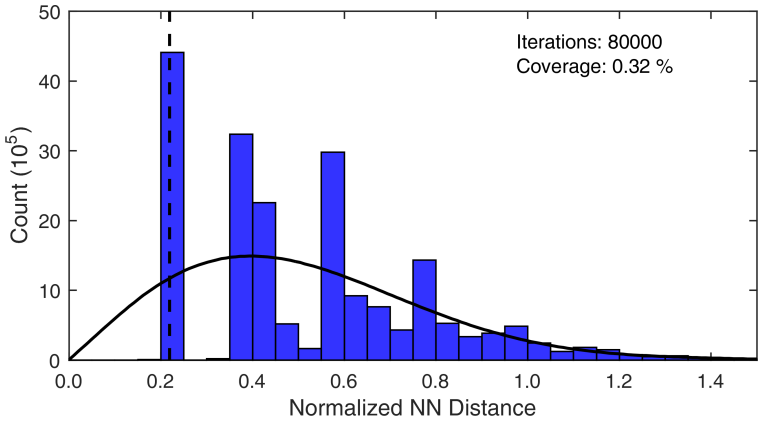

(b) Medium coverage, $c = 0.32\,\%$.

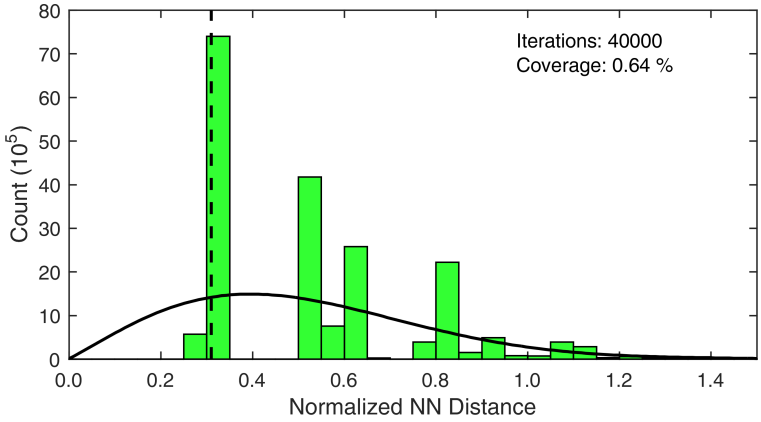

(c) High coverage, $c = 0.64\,\%$.

Figure 6.13: Through Monte Carlo methods obtained nearest-neighbor distributions for coverages close to the experimental ones.

6.3 Local Height Spectroscopy

The type of spectroscopy was chosen to be $Z(V)$. In this case, the tunneling voltage is tuned at a fixed point on the surface while the feedback loop remains enabled. The dependent variable is thus the position of the z piezo actuator. The method is equivalent to record multiple images at different voltages in order to determine the apparent height of a single cluster.
$Z(V)$ spectroscopy was performed in the third experiment after the final annealing step (100 K) within the Cu_{13} cluster spot. The overview images were taken at $U_{Gap} = 1.8\,V$ and $I_T = 16\,pA$ with a frame size of $50 \times 50\,nm^2$. After scanning a promising cluster, the spectroscopy measurement is initialized by selecting the center of the imaged cluster. In order to not lose the correct position due to thermal drifting, only a few seconds elapsed between imaging and spectroscopy of an object. The results for a small cluster (potentially adsorbate), a large cluster (Cu_{13}) and a free spot on the surface are depicted in figure 6.14. The curves are

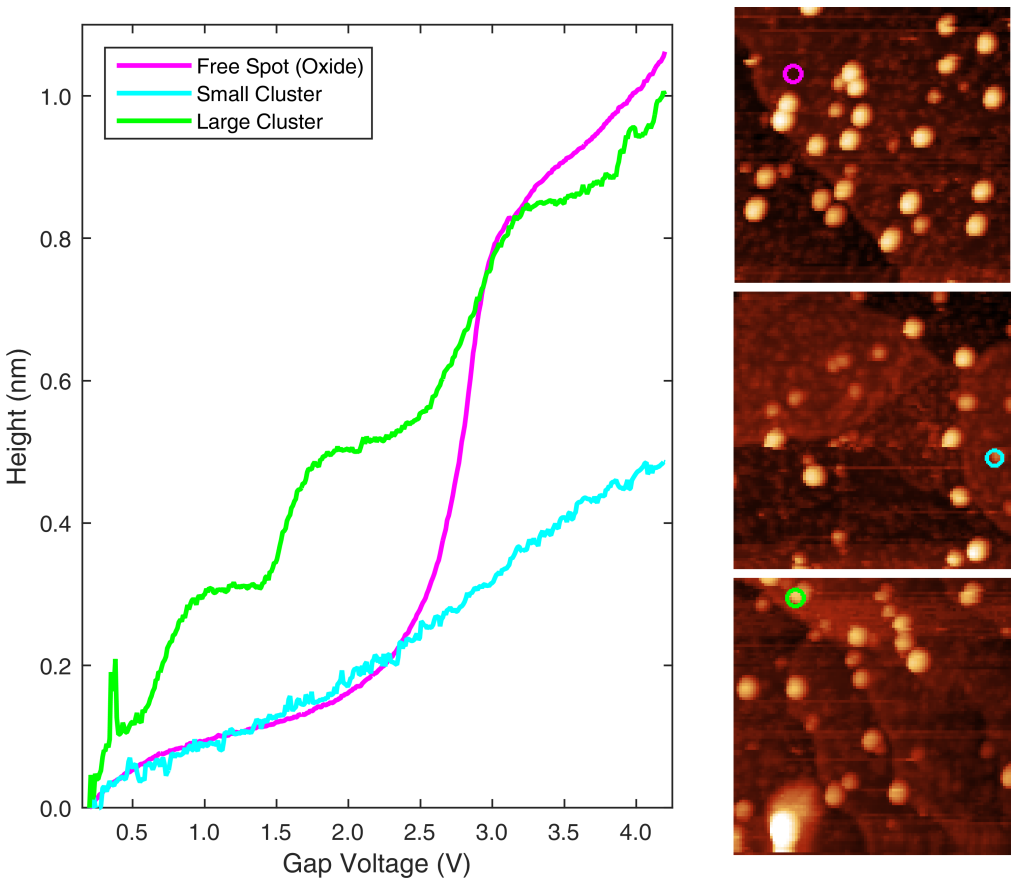

Figure 6.14: $Z(V)$ spectroscopy within the Cu_{13} spot.

set to zero at the beginning of the measurement, since the absolute height may differ due to different positions, terraces or thermal drifting. For all acquired data a voltage range of $U_{\mathrm{Gap}} = 0.2 \ldots 4.2\,\mathrm{V}$ with 400 points and a dwell time of 10 ms was used. Regarding the free spot on γ'-$Al_2O_3/Ni_3Al(111)$ the onset of the rise in height at $U_{\mathrm{Gap}} \approx 2.5\,\mathrm{V}$ is in good agreement with $^{\mathrm{d}I}/_{\mathrm{d}V}$ measurements performed by S. Degen [Deg06]. The height of the small cluster with respect to the oxide was determined to $h = 0.7\,\mathrm{nm}$ indicating that it rather counts as an adsorbate. A nearly linear dependence of the height on the applied tunneling voltage is found.

The $Z(V)$ curve of a Cu_{13} cluster exhibits several plateaus. The reversal points are determined to $U_{\mathrm{rev}} = \{0.71, 1.56, 2.89, 4.03\}\,\mathrm{V}$. The spacing suggests that these plateaus are caused by quantized states within the cluster. Assuming free electrons, the mean energy spacing in case of spin degeneration can be calculated through

$$\delta E = \frac{2\pi^2\hbar^2}{m k_{\mathrm{F}} V}$$

with the electron mass m, the volume of a spherical Cu_{13} cluster V and the Fermi wave vector k_{F} [Ral95]. Copper yields $k_{\mathrm{F}} = 1.36\,\mathrm{\AA}^{-1}$ [Ash76] and thus the lower bound for the energy spacing amounts to $\delta E = 0.72\,\mathrm{eV}$. An upper bound is obtained by means of the Jellium model for a spherical cluster

$$\Delta E = \frac{\hbar^2 k_{\mathrm{F}} \pi}{2.71 m R}$$

with the cluster radius R and the prefactor coming from the average length of classical orbits [Bra93]. This results in an upper bound of $\Delta E = 3.61\,\mathrm{eV}$. The measured plateau width of $\Delta U = 0.85 \ldots 1.33\,\mathrm{V}$ is in good accordance with these theoretically obtained limits for Cu_{13} clusters.

Another explanation can be given through image states, caused by the response to the presence of an electron. These states are hydrogen-like, but expanded and shifted due to the Stark effect if an electric field is applied. For $^{\mathrm{d}I}/_{\mathrm{d}V}$ spectra taken on a Ni(100) surface a series of maxima arises [Bin85], which is equivalent to plateaus in $Z(V)$ spectra. In the case of particle adsorption (or cluster deposition) the structure of the image state spectrum remains unchanged [Plo07]. However, these states are observed at rather large tunneling voltages of $U_{\mathrm{Gap}} > 3.2\,\mathrm{V}$ and the spacing naturally decreases with higher voltages (n^{-2} dependence) in contrast to the spectrum depicted in figure 6.14.

Steps in $Z(V)$ respectively $I(V)$ spectra could also be caused by the electron

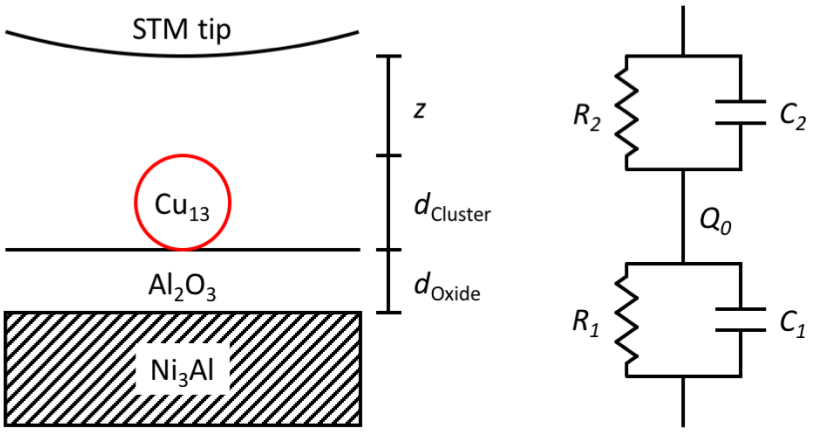

Figure 6.15: Geometrical setup on the surface and corresponding circuit for modelling a double tunneling barrier.

phonon coupling. As shown in [Sap06] for the tunneling through suspended carbon nanotubes, the plateaus are then equally spaced in voltage, which was not observed in the case of $Cu_{13}/Al_2O_3/Ni_3Al$. In addition, the spacing here is of the order of eV, while it is of the order of meV in [Sap06].
Since a cluster is a nanoscopic object, single electron effects have to be considered. A phenomenon occurring in this field is the formation of a Coulomb barrier, firstly observed in the late 1980s [Ful87]. Assigning an additional electron to a cluster changes its potential by $U = e/C$, where C is the capacitance of the cluster with respect to its surrounding. If C is sufficiently small the energy required for an electron to get on the cluster may be larger than its thermal energy and the energy gained by an external field. In this case the junction is blocked. Due to the non-conducting character of the oxide the system $Cu_{13}/Al_2O_3/Ni_3Al$ represents a double tunneling barrier. A numerically solvable model for obtaining $I(V)$ curves is presented in [Han91]. Parameters are the resistance R and capacitance C of the respective junction, the residual charge on the cluster Q_0 and the temperature T. A circuit diagram, compared to the actual geometry, is depicted in figure 6.15. The capacitance is calculated assuming a sphere (cluster) above a planar surface (substrate respectively tip), which is twice the capacitance of two closely separated spheres

$$C = 2 \cdot 2\pi r \varepsilon_0 \varepsilon_\mathrm{r} \left(\frac{d^3 + dr^2 - r^3}{d^3 - dr^2} \right) \tag{6.4}$$

with the permittivity ε, the sphere radius r and the distance between their centers d [Stö13]. The tip apex is more or less blunt compared to the cluster dimensions

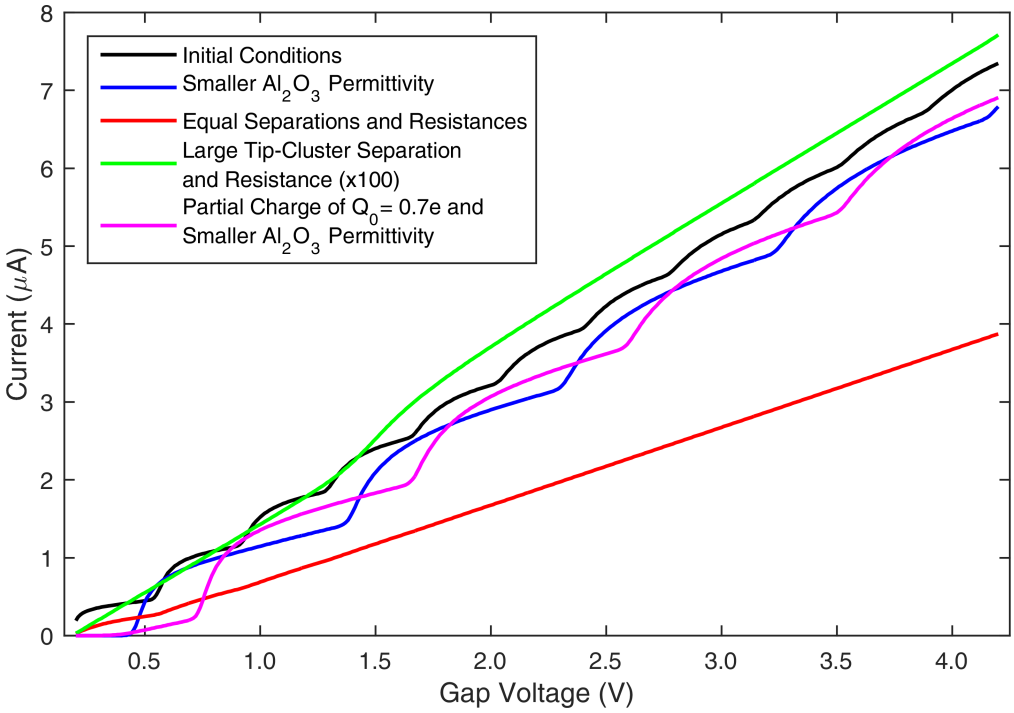

Figure 6.16: Numerically obtained $I(V)$ curves for a double tunneling barrier.

and therefore modeled as a planar surface ($r_{\mathrm{tip}} \to \infty$). For the tunneling junction tip-cluster $\varepsilon_{\mathrm{r}} = 1$ is obvious, while the junction cluster-substrate is governed by the dielectric material Al_2O_3 with $\varepsilon_\infty \approx 3$ in the high frequency limit [Pas09] and $\varepsilon_{\mathrm{r}} \approx 7.5$ in the static case [Rav06]. The geometric radius, deduced from equation (2.1), $r\,(\mathrm{Cu}_{13}) = 3.3\,\text{Å}$ may be enlarged by an electron spillout of $\sigma = 0.74\,\text{Å}$ [Kni92], yielding a sphere radius of $r = 4.04\,\text{Å}$. Together with the thickness of the oxide film $d_{\mathrm{oxide}} = 5.0\,\text{Å}$, a capacitance of $C_1 = 4.33 \cdot 10^{-19}\,\mathrm{F}$ is calculated. The resistance of the first junction is set to $R_1 = 500\,\mathrm{k\Omega}$ following theoretical calculations from [Lan87] for a tunneling distance of d_{oxide}. In the same manner, a tip-cluster separation of $z = 0.1\,\text{Å}$ is assumed, yielding $R_2 = 32\,\mathrm{k\Omega}$ and $C_2 = 8.28 \cdot 10^{-20}\,\mathrm{F}$. Together with $T = 77\,\mathrm{K}$ and $Q_0 = 0\,\mathrm{C}$ are these the initial conditions for modeling the double tunneling barrier. The resulting $I(V)$ curve (black) is shown in figure 6.16. Proceeding from this point several variations can be considered respectively:

- ε_{r} is based on a rather thick layer of Al_2O_3, which was most likely investigated at room temperature. The value for the film used here may be smaller, hence $\varepsilon_{\mathrm{r}} = 3$ is taken into account (blue curve).

- The tip-cluster separation of 0.1 Å lies nearly in the contact regime - a more reasonable distance would be $z = 5.0\,\text{Å}$, resulting in equal parameters for both junctions (red curve).
- The tip-cluster separation is modified further to $z = 7.0\,\text{Å}$, which also increases the resistance to $R_2 = 50\,\text{M}\Omega$ (green curve).
- It can not be excluded that the cluster is partially charged, therefore Q_0 was set to 0.7 e in addition to the small $\varepsilon_\text{r} = 3$ (magenta curve).

All curves exhibit the behavior of a Coulomb barrier with similarities to the $Z(V)$ spectroscopy presented in figure 6.14. However, the quantitative course of these $I(V)$ spectra is not directly comparable to $Z(V)$ spectra. It is noticeable that the reversal points for a smaller ε_r and a partially charged cluster are in good agreement with the experimental obtained data, although the model predicts equally spaced plateaus.
The introduced model has to be extended to simulate $Z(V)$ spectra. Therefore, $I(V)$ curves for numerous distances between tip and cluster z in the interval $[0, 1.2]\,\text{nm}$ are calculated. The capacitance C_2 respectively the resistance R_2 is obtained through equation (6.4) respectively

$$R_2(z) = \begin{cases} R_0 & z < z_0 \\ R_0 \cdot 10^{(z-z_0)/1\,\text{Å}} & z \geq z_0 \end{cases}$$

with $R_0 = 32\,\text{k}\Omega$ and $z_0 = 373\,\text{pm}$. These values are deduced from figure 6.17, originally calculated by [Lan87]. The knee between 5 and 9 bohr is roughly approximated as a kink resulting in a maximum deviation of $\approx 33\,\text{k}\Omega$ at 7 bohr. For every voltage V, a tip-cluster distance z satisfying $I(V, z) = 16\,\text{pA}$ (setpoint of the experimental data) is selected, leading to a dataset of $Z(V)$. The simulated spectrum is shown in figure 6.19 (black curve). Additional spectra were obtained by setting $\varepsilon_\text{r} = 3$ (blue curve), a partial charge of $Q_0 = 0.7\,\text{e}$ (cyan curve) and a combination of both (magenta curve). Comparing $I(V)$ and $Z(V)$ it is clearly visible, that the individual steps are less pronounced in $Z(V)$. The initial rise in z for all spectra can be regarded as an establishment of a conventional tunneling process with typical distances of $z \approx 1\,\text{nm}$, while subsequent steps are then caused by the double tunneling barrier (in particular the capacitance). For both, the initial parameter set and a smaller Al_2O_3 permittivity, a step at $U_\text{Gap} \approx 1.5\,\text{V}$ occurs, in good agreement with the experimentally obtained data. However, the simulated curves are not completely reflecting the $Z(V)$ spectrum shown in figure 6.14. It should be noted, that R_1 and R_2 are additionally voltage

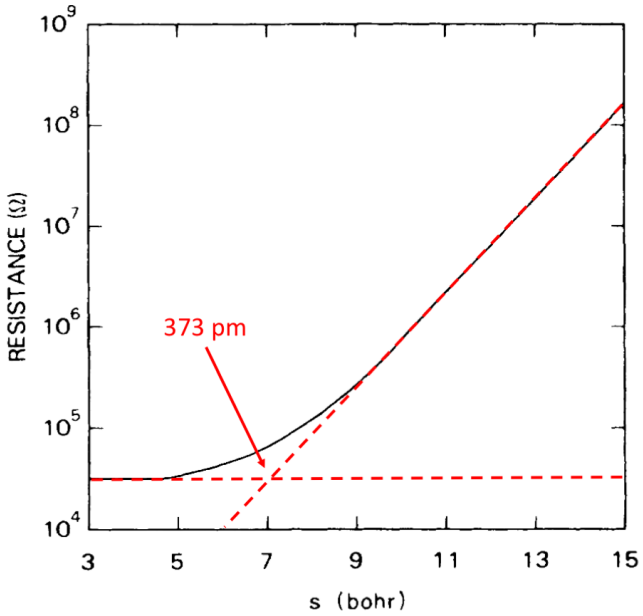

Figure 6.17: Tunneling resistance vs. tip surface separation s, which is measured from the nucleus of the tip atom to the positive background edge of the sample. $s = 3$ bohrs refers to a contact between tip and sample. The curve is approximated by a constant and an exponential part (dashed lines). Reprinted figure with permission from [Lan87]. Copyright 1987 by the American Physical Society.

dependent, which is not included in this simple model. The calculations from [Lan87] are valid for small voltages, zero temperature and a single Na tip atom. The increase at $U_{\mathrm{Gap}} \approx 2.5\,\mathrm{V}$ (see figure 6.14) is explainable due to additional conducting channels within the oxide film and thus a breakdown of the double tunneling barrier. The apparent height, as imaged by the STM, is assumed to be

$$h(U_{\mathrm{Gap}}) = d + 2\sigma + \kappa(U_{\mathrm{Gap}}) \tag{6.5}$$

with the geometrical diameter d from equation (2.1), the electron spillout σ and the offset $\kappa(U_{\mathrm{Gap}})$ caused by the oxide film. As observed by S. Degen [Deg06], the height of clusters on γ'-Al_2O_3/Ni_3Al is measured correctly for tunneling voltages $U_{\mathrm{Gap}} < 1.0\,\mathrm{V}$ and $U_{\mathrm{Gap}} > 3.0\,\mathrm{V}$, while it is measured with an offset therebetween. In terms of figure 6.14 the course of the $Z(V)$ spectra of a Cu_{13} cluster and a free spot on the oxide is roughly identical[11] for $U_{\mathrm{Gap}} < 0.7\,\mathrm{V}$ and $U_{\mathrm{Gap}} > 3.3\,\mathrm{V}$. A visualization of the tip trace when scanning clusters deposited on the oxide

[11] The curves were set to zero at $U_{\mathrm{Gap}} = 0.2\,\mathrm{V}$ and not in the high voltage regime assuming that the tip-cluster separation lies nearly in the contact regime for $U_{\mathrm{Gap}} = 0.2\,\mathrm{V}$. A minor offset in the high voltage regime can therefore not be excluded.

film, analogous to [Car97], can be found in figure 6.18 for the different voltage regimes. This implies that κ can be deduced from the difference of the $Z(V)$ spectra yielding an offset of $\kappa(1.8\,\mathrm{V}) \approx 4\,\text{Å}$ in apparent height of the cluster for $U_{\mathrm{Gap}} = 1.8\,\mathrm{V}$. The approach does not only include the additional tunneling distance caused by the oxide, but also the electronic structure of the cluster, which might change if investigating another cluster size. For the Cu_{13} cluster in the overview image, recorded at $U_{\mathrm{Gap}} = 1.8\,\mathrm{V}$, $h = 1.2\,\mathrm{nm}$ is thus expected, whereas $h = 1.3\,\mathrm{nm}$ was found.
In summary, it can be stated that the $Z(V)$ plateaus are either caused by electronic states within the cluster or a coulomb barrier. Other considered effects do not match the actual circumstances found in the spectrum for Cu_{13} in figure 6.14. The spectroscopic results help to interpret the height histograms, presented in the following.

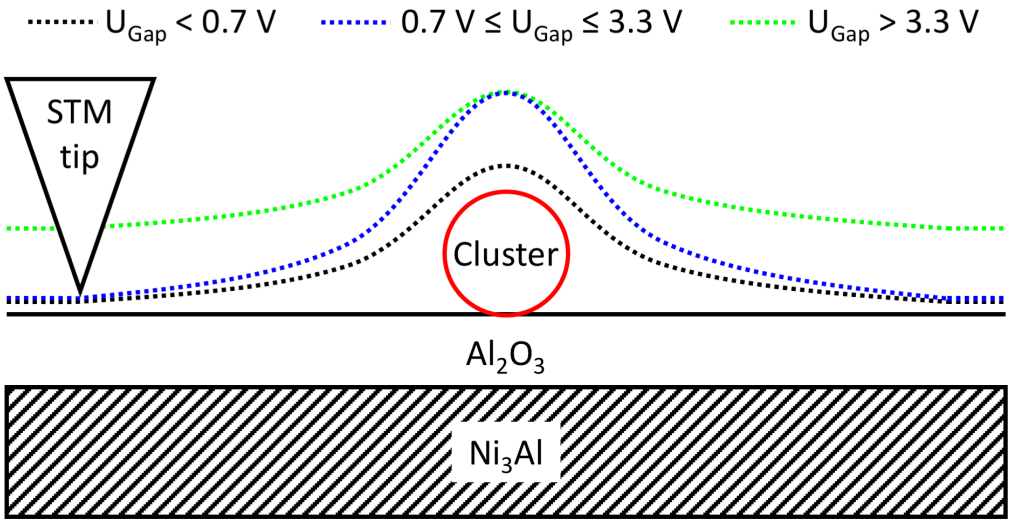

Figure 6.18: Tip trace when scanning a cluster deposited on the oxide film for the different voltage regimes inspired by [Car97].

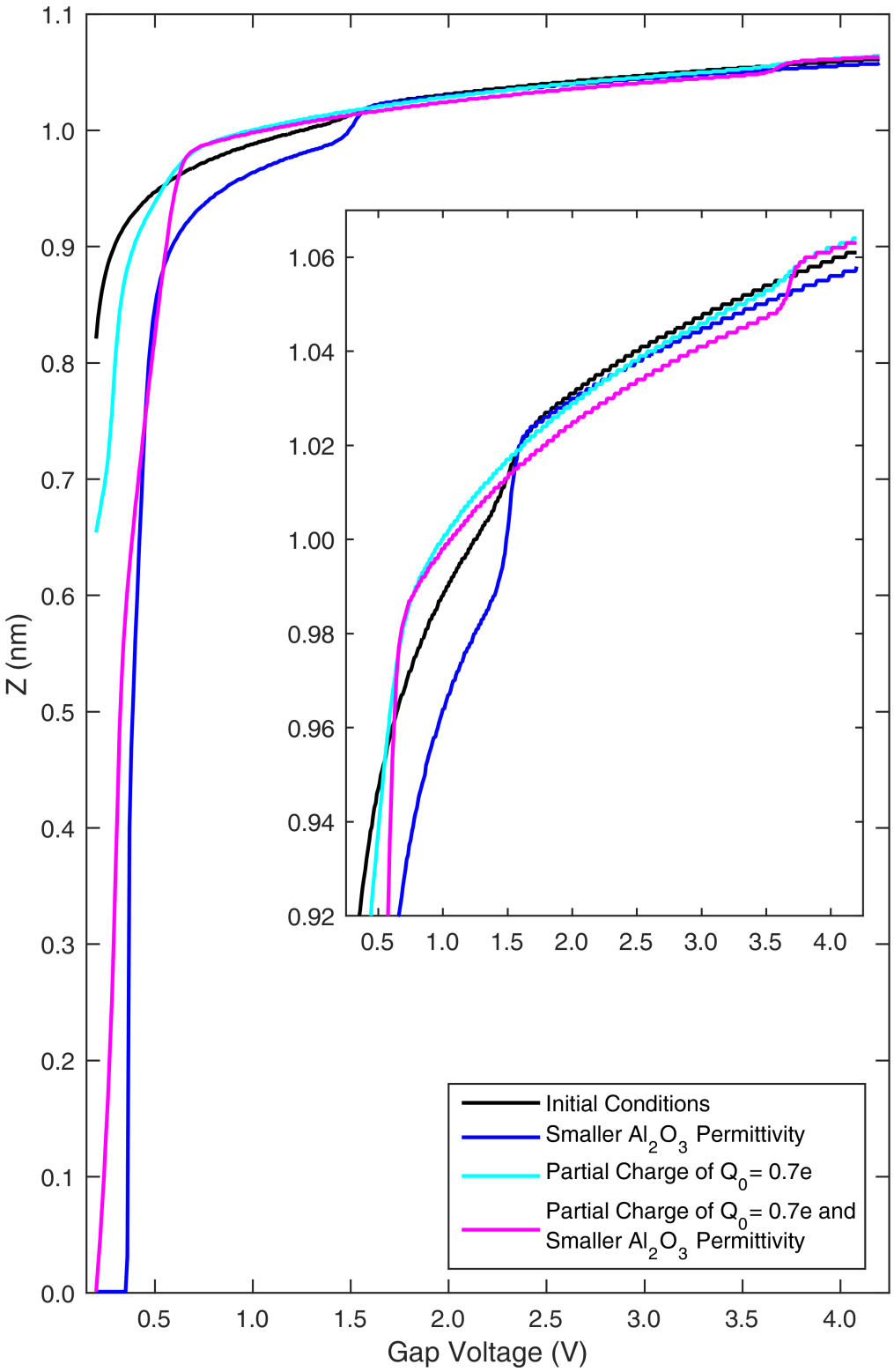

Figure 6.19: Numerically obtained $Z(V)$ curves for a double tunneling barrier. The inset shows an enlargement of the plateau region.

6.4 Apparent Cluster Height

The cluster height is of particular interest, since it indicates whether clusters retain a mass selection after deposition. The apparent height for clusters on γ'-Al_2O_3/Ni_3Al, as measured by STM, strongly depends on the applied voltage between tip and sample. For $U_{\mathrm{Gap}} < 3.0\,\mathrm{V}$ no states within the oxide film are available [Deg06] due to a rather large band gap of $E_{\text{band gap}} \approx 7\,\mathrm{eV}$ [Ros99b]. In this case, the oxide layer can be regarded as an additional tunneling distance and a variable thickness $\kappa(U_{\mathrm{Gap}})$ has to be subtracted from the apparent height. In order to get the geometric cluster height, an electron spillout has to be considered in addition (see equation 6.5). For $U_{\mathrm{Gap}} \geq 3.3\,\mathrm{V}$ the cluster height is measured with respect to the oxide surface, i.e. it should equal the diameter including spillout if the cluster is intact and no penetration took place. Due to imaging issues both ranges of tunneling voltages were used, hence blue histograms belong to low voltages ($\kappa(U_{\mathrm{Gap}}) \neq 0$), while green histograms indicate a higher tunneling voltage to directly obtain $d_{\mathrm{cluster}} + 2\sigma$. Unfortunately, the presence of adsorbates is unavoidable. In order to distinguish between adsorbed particles and clusters an area at the rim of the sample, where no clusters were deposited, was scanned. The obtained height histogram is depicted in figure 6.20. A maximum at $d \approx 0.7\,\mathrm{nm}$ can be identified. But even adsorbates with $d \approx 1.0\,\mathrm{nm}$ contribute a noticeable amount. The measurements were solely carried out using tunneling voltages between 1.5 V and 2.0 V. Referring to the spectroscopic results (see figure 6.14), the height of adsorbed particles is imaged correctly for $U_{\mathrm{Gap}} < 2.5\,\mathrm{V}$. For higher voltages they might appear smaller by 4 - 5 Å.

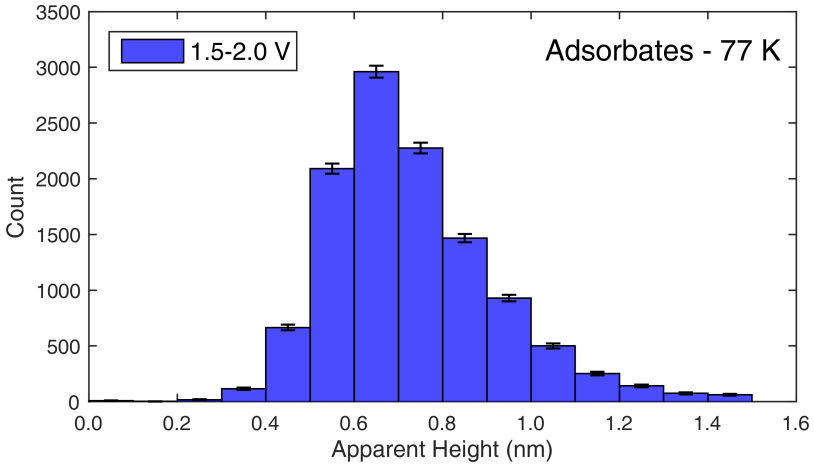

Figure 6.20: Height distribution of adsorbed particles without clusters.

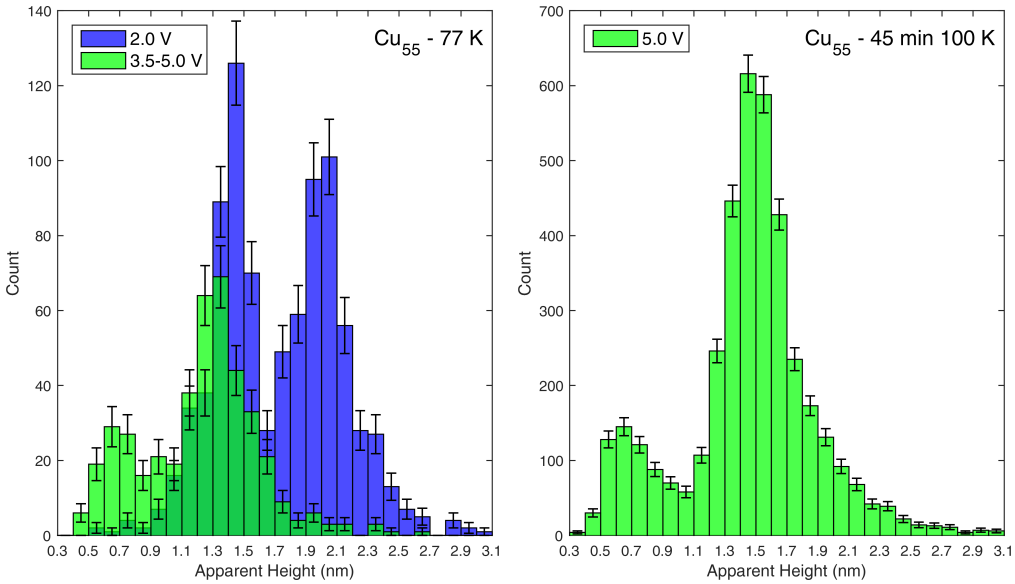

Figure 6.21: Height distributions of Cu_{55}, 1st experiment. Left: distributions as deposited for both voltage regimes. Right: distribution for high tunneling voltages after annealing to 100 K for 45 min.

A classification of different coverages analogous to section 6.1 yields no additional results and is therefore omitted here. Using a PtIr tip for the first experiment, most stable imaging was achieved with $U_{\mathrm{Gap}} = 5.0\,\mathrm{V}$. The typically chosen setpoint for the tunneling current lies in the range of $I_{\mathrm{T}} = 70\text{-}100\,\mathrm{pA}$. Figure 6.21 contains the apparent height of Cu_{55} clusters for the first experiment. Shortly after deposition a two peak structure for both voltage regions arises. By shifting one of the distributions $\approx 7\,\text{Å}$, a satisfying matching can be established, indicating that $\kappa(2.0\,\mathrm{V}) = 7\,\text{Å}$ for Cu_{55} clusters, which is plausible for the used tunneling current and voltage (compare figure 6.17). Referring to equation (6.5), the apparent height of deposited clusters is meant to be $h(2.0\,\mathrm{V}) = 1.92\,\mathrm{nm}$ and $h(3.5\text{-}5.0\,\mathrm{V}) = 1.22\,\mathrm{nm}$, compared to the experimentally determined maxima at $h(2.0\,\mathrm{V}) = 2.0\,\mathrm{nm}$ and $h(3.5\text{-}5.0\,\mathrm{V}) = 1.3\,\mathrm{nm}$. Furthermore, the width of these peaks is in good accordance with previous measurements of similar sized Ag clusters on Au(111) [Mir13] yielding a proper mass selected and intactly landed clusters on the surface. Compared to the mass spectrum shown in figure 4.5, a broadening of the peak for a single cluster mass, imaged by the STM, is unavoidable due to different cluster isomers, orientations and binding sites on the surface [Mes00]. The second maximum at 0.7 nm respectively 1.4 nm should be adsorbate induced, although the height seems too large. As stated from the spectroscopic results, the height of adsorbates is imaged correctly for

low tunneling voltages, hence $h = 1.4\,\text{nm}$ is assumed. This does not reflect the maximum occurring in figure 6.20, but a height of 1.4 nm was also found there. After the first annealing step to 100 K for 45 min the histogram structure remains unaltered, but the maximum is slightly shifted to larger heights. Cu_{55} clusters are potentially decorated with adsorbed particles due to the enhanced mobility of the adsorbates. Furthermore, ripening processes, in particular Ostwald ripening, can not be excluded.

Height histograms for the subsequent heating procedures can be found in figure 6.22 and figure 6.23. After the second annealing step to 200 K for 45 min it was again possible to obtain data in both voltage regimes. For low voltages the histogram is nearly identical to the one obtained at 77 K, although the occurrences of larger particles $h > 2.0\,\text{nm}$ has increased. Focusing on high tunneling voltages, the maximum shifts back to its former position, but a shoulder at 1.8 nm arises. This may occur due to merging of entire clusters or additional ripening. Upon the next annealing step, the shoulder becomes more distinct resulting in potentially two cluster species regarding the apparent height. It seems all the more astonishing that, after annealing to 400 K for 45 min, this shoulder vanishes or is at least incorporated by the Cu_{55} assigned maximum. A possible explanation is a metastable configuration of this height as observed for Ag clusters on C_{60} covered Au(111) [Duf10].

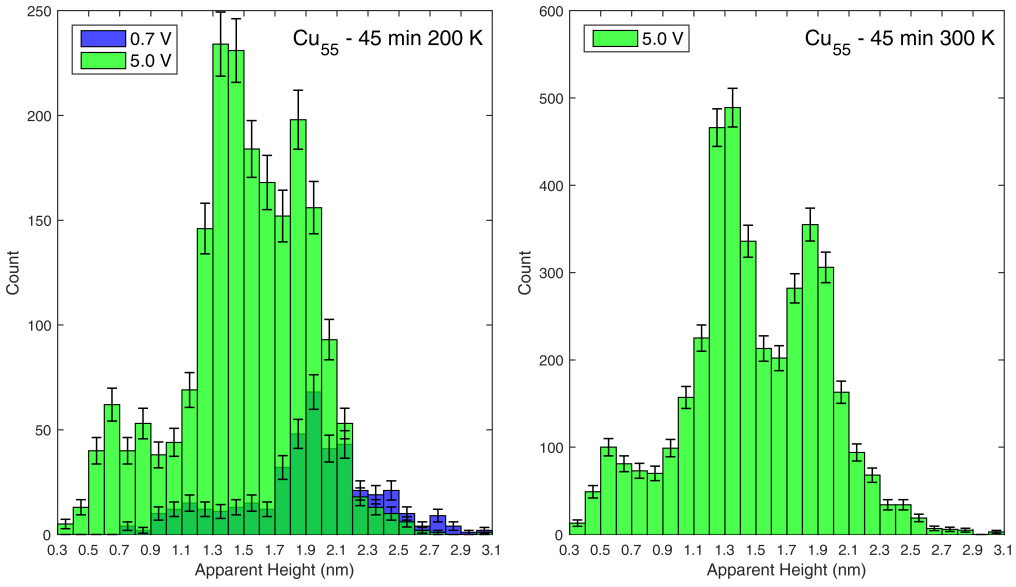

Figure 6.22: Height distributions of Cu_{55}, 1st experiment. Left: distributions for both voltage regimes after annealing to 200 K for 45 min. Right: distribution for high tunneling voltages after annealing to 300 K for 45 min.

Data acquisition for the final annealing step to 600 K for 45 min was only feasible in the low voltage regime and revealed a maximum at 2.0 nm, which is in perfect agreement with the data obtained shortly after deposition at 77 K. Summarizing the first experiment, it is remarkable that the maximum belonging to Cu_{55} clusters is clearly visible over the whole heating procedure. The system can hence be regarded as stable at room temperature and above.
In order to verify the results of the first experiment, Cu_{55} clusters were deposited once again and additionally a spot of Cu_{309}. A new PtIr tip was introduced to the STM and the typical tunneling current was decreased to $I_T = 15 - 20$ pA. The height distributions, as measured after deposition at 77 K, are shown in figure 6.24. Here only high tunneling voltages $U_{Gap} \geq 3.2$ V were feasible. The first maximum of the Cu_{55} distribution at 1.5 nm equals the height found for this cluster size after the first annealing step of the first experiment. However, a second maximum at 2.4 nm can also be found. This finding holds for Cu_{309} clusters likewise. The maximum at 2.0 nm is in good accordance with the geometrical cluster height of $d(Cu_{309}) = 1.91$ nm and the previously mentioned electron spillout. A second, even higher, peak at 2.8 nm arises. Due to intense stability problems with the STM tip, it is reasonable to explain the unclear results with tip artifacts. Referring to the shape of this certain STM tip (see chapter 7) elastic deformation of the tip or cluster [Sol86] might play a role.

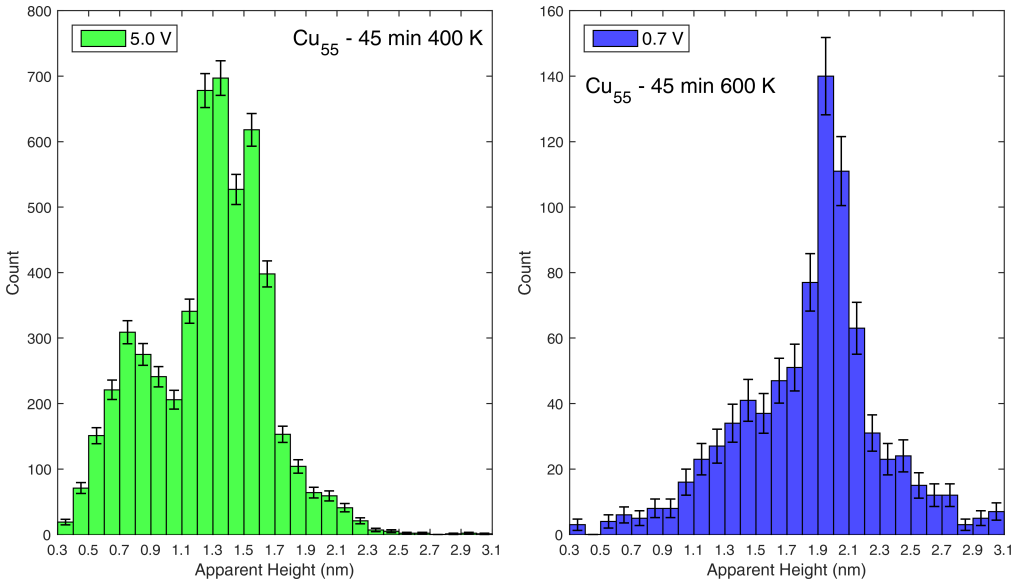

Figure 6.23: Height distributions of Cu_{55}, 1st experiment. Left: distribution for high tunneling voltages after annealing to 400 K for 45 min. Right: distribution for low tunneling voltages after the final annealing to 600 K for 45 min.

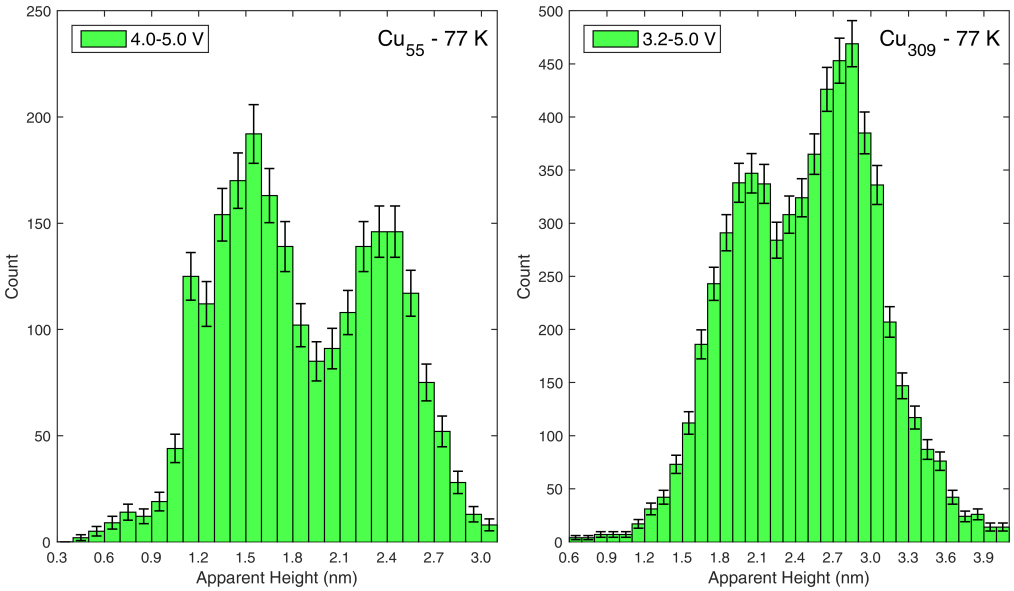

Figure 6.24: Height distributions for the 2nd experiment as deposited at 77 K. Only the high voltage regime was probed. Left: distribution for Cu_{55} clusters. Right: distribution for Cu_{309} clusters.

In the third experiment, switching to a tungsten tip and leaving the tunneling current setpoint untouched, it was solely possible to obtain data in the low voltage regime. Higher voltages $U_{\mathrm{Gap}} > 3.0\,\mathrm{V}$ lead to rapid variations of the tip structure resulting in unstable imaging. Beside Cu_{55}, a spot of Cu_{13} clusters was deposited on this occasion. The corresponding height distributions for Cu_{55} are depicted in figure 6.25. The two maxima structure of former measurements is obviously conserved as well as their position. The peak at 1.9 nm belongs to Cu_{55} clusters, whereas the left one could emerge from adsorbates as described previously. The height distributions obtained for Cu_{13} clusters are shown in figure 6.26. Taking the spectroscopic measurements of Cu_{13} clusters, discussed in section 6.3, as a basis, their apparent height according to equation (6.5) is assumed to be $h(1.8\,\mathrm{V}) = 1.22\,\mathrm{nm}$. The maximum at 1.3 nm can hence be identified with Cu_{13} clusters - this is clearly visible shortly after deposition at 77 K. The ensuing annealing steps reveal an increasing second maximum at 0.9 nm, which is explainable through adsorbed particles. Even storage under UHV conditions does not prevent this type of contamination completely. The measurements confirm that both, Cu_{13} and Cu_{55} clusters, do undoubtedly not coalesce for $T \leq 100\,\mathrm{K}$. The system Cu clusters on an aluminum oxide support can therefore be regarded as well-suited for catalysis, while, for instance, catalytical active Pd atoms on magnesium oxide start coalescing at 90 K [Jud05].

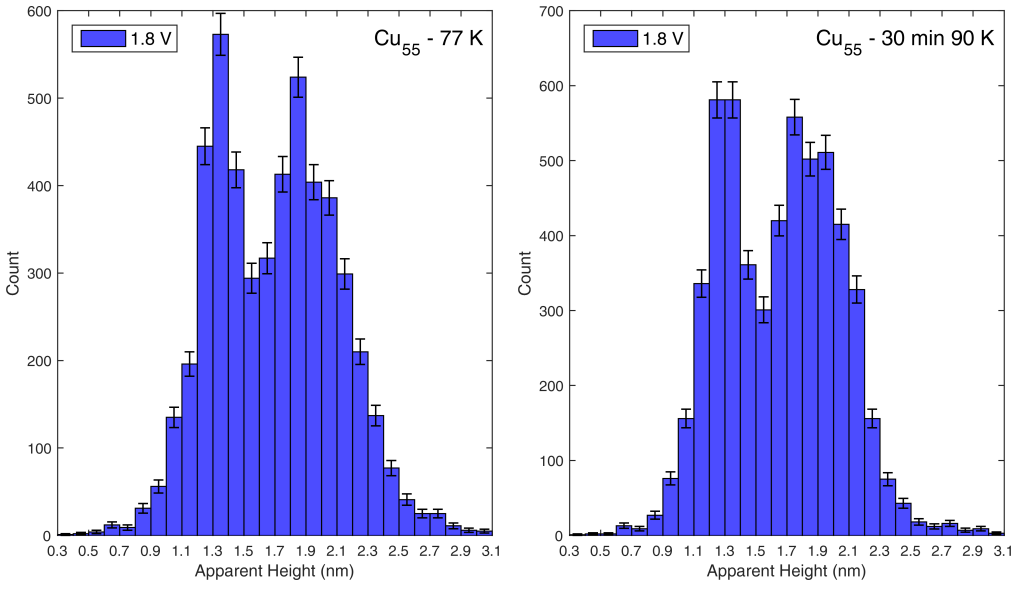

(a) 77 K as deposited.

(b) 90 K for 30 min.

(c) 95 K for 30 min.

(d) 100 K for 30 min.

Figure 6.25: Height distributions of Cu_{55}, 3rd experiment. See (a) - (d) for annealing temperature and duration.

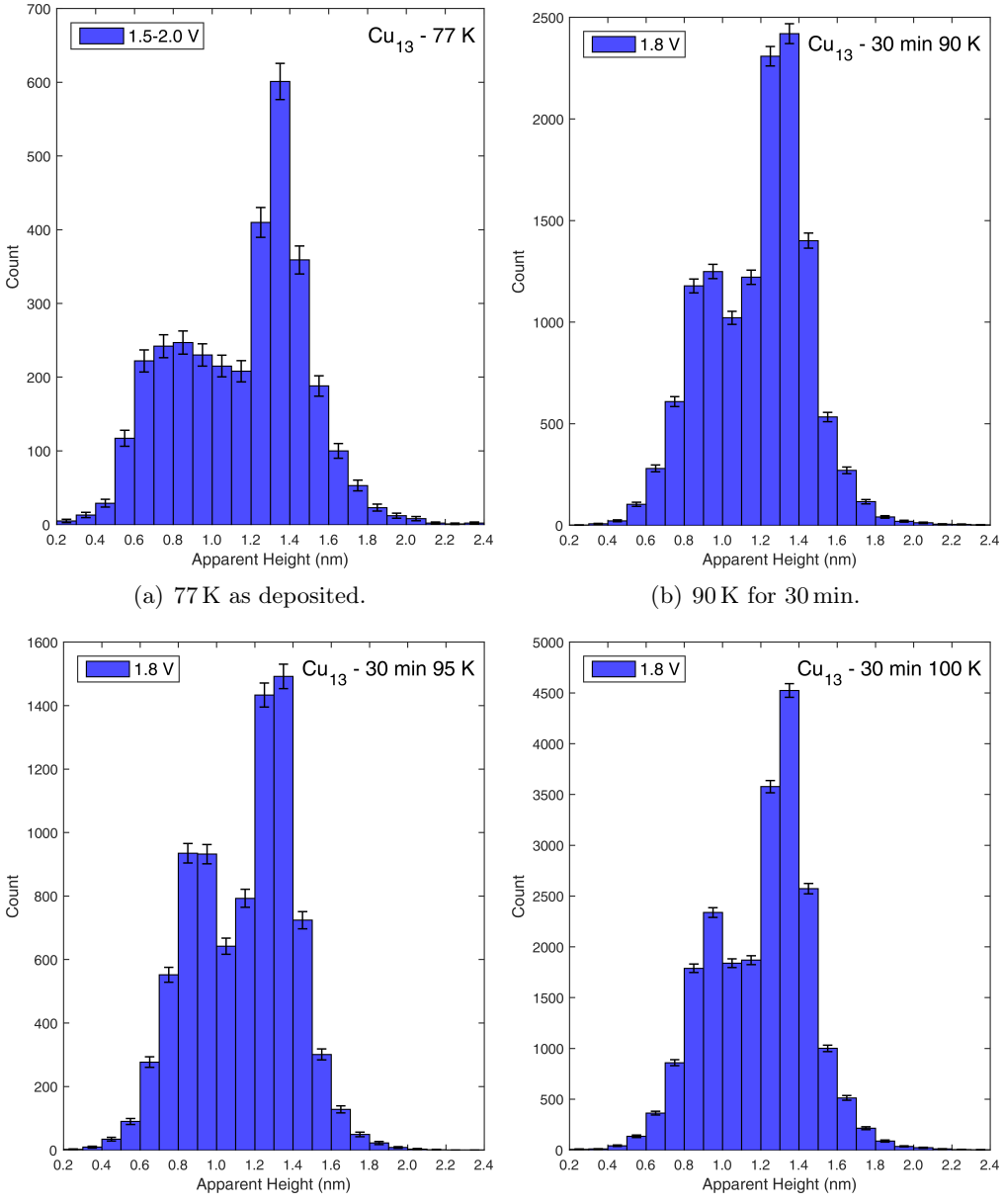

(a) 77 K as deposited.

(b) 90 K for 30 min.

(c) 95 K for 30 min.

(d) 100 K for 30 min.

Figure 6.26: Height distributions of Cu_{13}, 3rd experiment. See (a) - (d) for annealing temperature and duration.

Chapter 7

Discussion

This chapter gives an overview of the results concerning mass selected copper clusters on γ'-$Al_2O_3/Ni_3Al(111)$. Beside a summary and further conclusions, a critical review on single results is given as well.

The first experiment for Cu_{55} clusters, deposited on the oxide film, clearly shows a jump by means of the deviation from a random arrangement after the first heating step was applied (see figure 6.5). This jump was not reproduced in the third experiment for Cu_{55} clusters, although there is a slight tendency visible (see figure 6.9(b)). The reason could be the change of the tip material (and hence the tip shape) from PtIr to W. If the apex geometry differs, particles might be imaged with increased lateral dimensions. For scanned frames exhibiting high coverages, these dimensions may exceed the lattice factor of the dot-structure. Thus, distances smaller than a_{dot} are not observed resulting in an initial high deviation from a random arrangement. Two closely separated clusters may appear as a single cluster and thus their distance is not recorded.

Another explanation for the absent jump of the deviation from a random arrangement could be the sample quality. Although a majority of the terraces exhibited the dot- and network-structure, some plateaus were decorated with zigzag features, referred to as stripe phase [Gri07]. As depicted in figure 7.1, the reconstruction shows a voltage dependence similar to the one found for dot- and network-structure. The zigzag pattern is visible tunneling at $U_{\mathrm{Gap}} = 3.2\,\mathrm{V}$, while $U_{\mathrm{Gap}} = 2.0\,\mathrm{V}$ yields again dots in a hexagonal arrangement. The spacing was determined to $a_{\mathrm{stripe}} = 4.42\,\mathrm{nm}$ (see line profile in figure 7.1), 2.2 % too small compared to AFM measurements resulting in 4.52 nm [Gri07]. It is not clear, if the dots arising from the stripe phase also serve as binding points for clusters. However, the shift of the nearest-neighbor distribution maximum can as well be explained through adsorption of clusters on these dots.

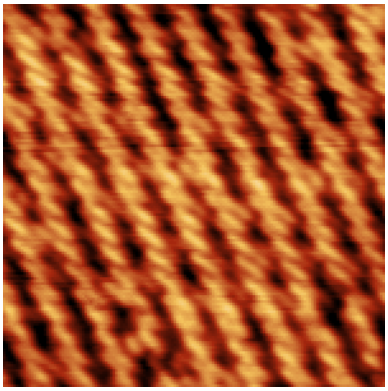

(a) Stripe-structure $U_{\mathrm{Gap}} = 3.2\,\mathrm{V}$.

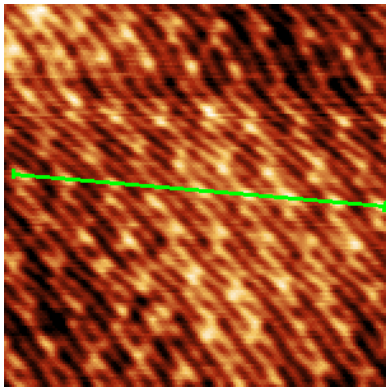

(b) Stripe-structure $U_{\mathrm{Gap}} = 2.0\,\mathrm{V}$.

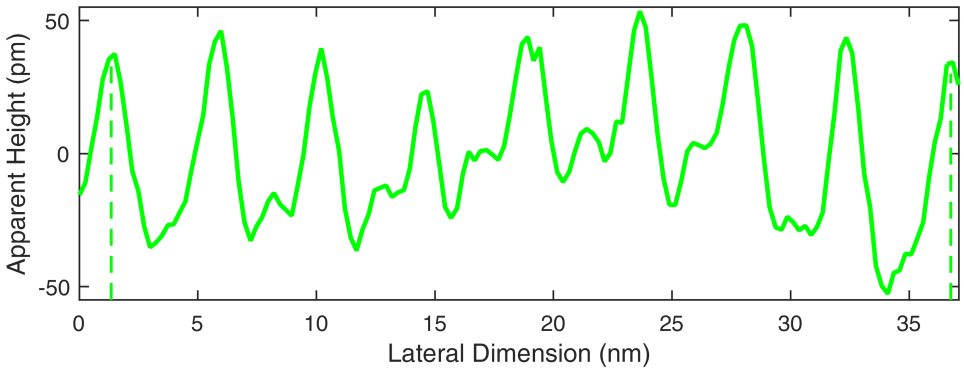

(c) Line profile along stripe-structure

Figure 7.1: Stripe phase of γ'-Al_2O_3. Parameters for both STM images: $I_{\mathrm{T}} = 50\,\mathrm{pA}$, $(37.5 \times 37.5)\,\mathrm{nm}^2$. (a) Stripe-structure visible at $U_{\mathrm{G}} = 3.2\,\mathrm{V}$. (b) Striped dots visible at $U_{\mathrm{G}} = 2.0\,\mathrm{V}$. (c) Line profile corresponding to (b). The dashed lines indicate an averaging measurement of the lattice constant.

There is also a conceptional problem, if using the coverage classifications introduced at the beginning of chapter 6: A range of coverages is pooled into one histogram with one normalized dot-structure lattice factor, referred to as limit, although $a_{\mathrm{dot,\ norm}}$ is different for each coverage. Focusing on high coverages of Cu_{55} clusters, the limit was set to $a_{\mathrm{char}} = 0.35$, which corresponds to a coverage of $c = 0.82\,\%$ - but also lower coverages, for instance $c = 0.5\,\%$ with $a_{\mathrm{dot,\ norm}} = 0.27$, are assigned to this category. Due to the square root in equation (6.2) the impact of the coverage on the normalized distance is reduced but not neglectable. On the other hand, a classification is needed for an appropriate illustration of the random nearest-neighbor distances compared to the dot-structure lattice factor. This is further justified by the fact that only a few occurrences below the respective limit given by a_{char} were counted.

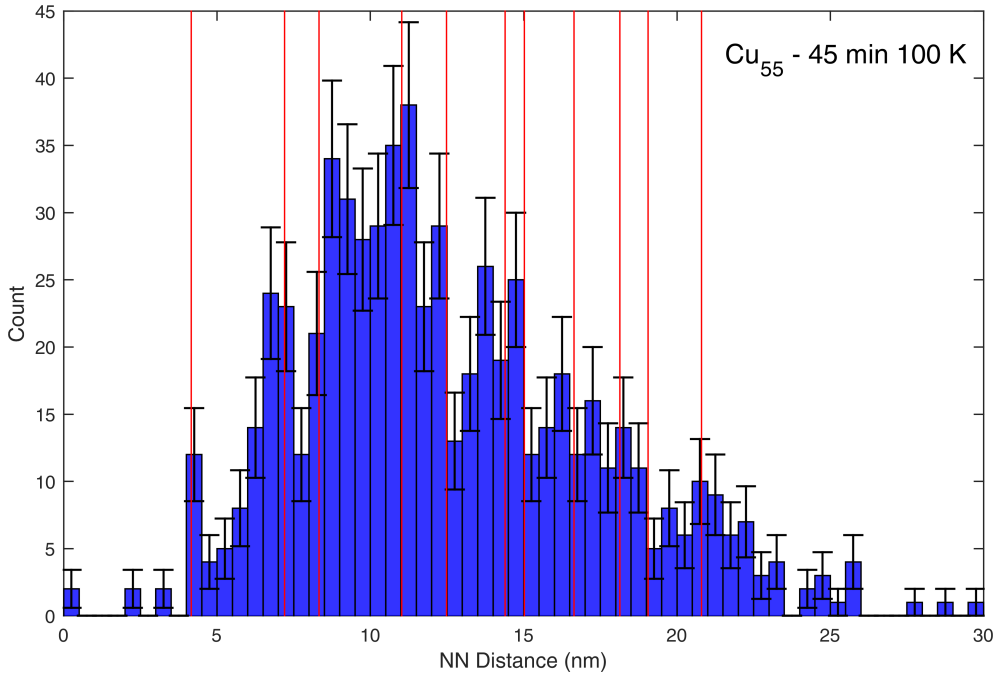

Figure 7.2: Measured NN Distances for Cu_{55} clusters, 1st experiment, 100 K. Distances associated with dot-structure sites are marked by red lines.

But the nearest-neighbor distances can also be visualized without normalization. If clusters align with the dot-structure, maxima at $d = a_{\mathrm{dot}}$, $d = \sqrt{3} \cdot a_{\mathrm{dot}}$, $d = 2a_{\mathrm{dot}}$ and at subsequent distances should occur. Figure 7.2 contains the distribution for measured distances in the first experiment after annealing to 100 K for 45 min (medium coverage). The first 11 nearest-neighbor distances associated with the hexagonal dot-structure are marked by red lines. It can be seen that maxima emerge at some dot-sites. Especially $a_{\mathrm{dot}} = 4.16\,\mathrm{nm}$ shows a significant count compared to adjacent distances. This visualization is independent of the coverage, but due to a smaller bin size needed to visualize the possible maxima at the red-line positions, most bins are related with a rather huge error of $> 20\,\%$. Therefore, detecting these maxima is in most cases at the limit of being statistically significant.

Concerning the height distributions of investigated cluster sizes, it is noticeable that the determined distribution of adsorbates is not retrieved in cluster height distributions. The reason may lie in the initial selection of clusters using the "clusterizer" software for semi-automatic height measurement. When investigating a frame, recorded in an empty spot, the shape and lateral dimensions of all particles (adsorbates) is nearly identical. This also applies for the brightness, which corresponds to the narrow height distribution found in figure 6.20. But if

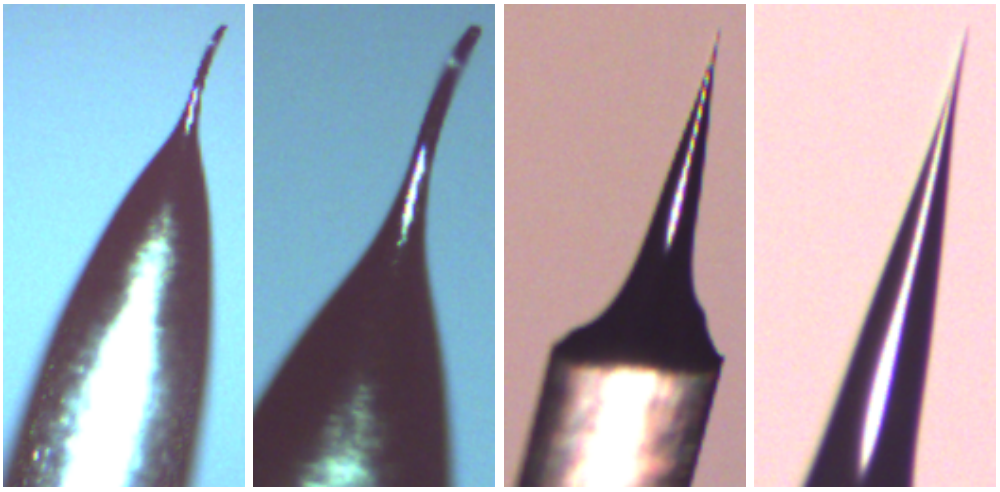

(a) PtIr tip (broken). (b) PtIr tip 2× zoom. (c) W tip. (d) W tip 2× zoom.

Figure 7.3: Images of used tips obtained through optical microscopy. (a) PtIr tip ($d_{\text{wire}} = 250\,\mu\text{m}$) for 2nd experiment. (b) PtIr tip 2× zoom. (c) W tip ($d_{\text{wire}} = 100\,\mu\text{m}$) for 3rd experiment. (d) W tip 2× zoom.

evaluating an image containing clusters and adsorbates, the height distribution gets wider, leading to bright particles (clusters) and darker ones (adsorbates). Furthermore, the lateral dimensions and shape of these two species might be different. Tendentially, only clusters are selected by the software operator, which simultaneously results in a truncation of smaller heights in a histogram for adsorbates. The sample was investigated over a time span of several months for each experiment, hence adsorbates are most likely present, although this is not reflected in the measured height histograms.

Focusing on the second experiment, the height distribution for Cu_{55} clusters deviates from all other distributions obtained for this cluster size. The first maximum at $h = 1.5\,\text{nm}$ is shifted 2 Å to larger heights compared to the maximum obtained shortly after deposition in the first experiment. Since the sample preparation was not changed, the reason should be caused by the STM itself. Indeed, the tip was exchanged, which worsened imaging stability and obviously did also affect the results. An explanation may be given through the shape of the PtIr tip. As depicted in figure 7.3 it is striking that the apex of this PtIr tip is decorated with a spike. This influences mechanical stability and may lead to vibrations during measurement and hence incorrect height determination in contrast to the well-shaped tungsten tip used afterwards for the third experiment. Unfortunately, as figure 7.3 indicates, the PtIr tip was additionally damaged before removing from the UHV chamber.

The maximum at $h = 0.6\,\mathrm{nm}$, found in Cu_{55} height distributions for high voltages in the first experiment, could also arise from clusters wetting the surface. Assuming an fcc lattice with $a_{\mathrm{copper}} = 3.61\,\text{Å}$ [Ash76], the stacking of three layers add up to $h = 3\sqrt{3} \cdot a_{\mathrm{copper}} = 0.63\,\mathrm{nm}$, which is fairly close to the mentioned maximum. Concerning the maximum at $h = 1.9\,\mathrm{nm}$, arising after annealing to $T = 200\,\mathrm{K}$ for 45 min, the formation of nine copper layers ($h = 1.88\,\mathrm{nm}$) seems unlikely. Therefore, it is reasonable to assume coalesced clusters or ripening processes causing this height.
The spectroscopic measurements of Cu_{13} clusters reveal important details to interpret the height distributions of various deposited cluster sizes. The modeling of a double tunneling barrier resulting in a Coulomb blockade for $I(V)$ could explain the arising plateaus in $Z(V)$ spectra, but some assumptions not directly extracted from the experiment had to be made. A comprehensive characterization of the experimental results was not achieved in the investigated voltage range. Therefore, the plateaus are rather caused by quantized states within the examined cluster. The upper and lower bounds, calculated through a simple model for electronic state spacing, are in good agreement with the measured plateau width.

Summary

In conclusion it was shown that mass selected copper clusters on γ'-Al_2O_3/$Ni_3Al(111)$ are stable concerning their height, even after various heating procedures up to 600 K lasting for 45 min. This has to be seen in contrast to the nucleation of copper clusters on the surface (no mass selection), which are subject to rapid growth after annealing to 650 K [Wil01].
By evaluating the nearest-neighbor distances of deposited clusters, it can be assumed that the dot-structure also serves as a template for nanostructuring with mass selected clusters opening huge advantages regarding size-sensitive catalysis. The non-conduction character of the oxide film causes a decoupling of the electronic cluster states from the substrate and hence enables the verification of quantized states within clusters.

Chapter 8

Outlook

Mass selected clusters on γ'-Al_2O_3/Ni_3Al(111) are an interesting system worth further investigation. One possible extension of the presented experiments could be the deposition of clusters near to the coverage limits to occupy the entirety of available dot-sites. In this case, the observation of regular cluster arrays on the surface should be visible directly in STM images without the evaluation of nearest-neighbor distances. Unfortunately, the amount of coalesced and agglomerated clusters will rise significantly to $\approx 28\,\%$ (assuming random cluster positions after deposition). However, a majority of deposited clusters will retain a mass selection and hence, for instance, maintained catalytic activity. Due to the high temperature stability of deposited clusters, γ'-Al_2O_3/Ni_3Al(111) proves as an ideal support, not only in terms of catalysis, but also regarding data storage, if using magnetic nanoparticles. For that reason, it should be considered to use magnetic cluster material like iron or cobalt. In the case of atomic beam deposition, it was found that the shape of iron islands (two-dimensional versus three-dimensional) depends on the substrate temperature [Leh06].
In order to study the height distributions further, the deposition of other cluster sizes should be intended. This would also enable additional spectroscopic measurements to verify whether emerging plateaus are caused by quantized states or yet a Coulomb blockade.
The Monte Carlo simulation program should be modified to handle multiple occupation of dot-sites in order to get correct results for high coverages. In addition, the effects of heating processes can be implemented. This would enable using a random distribution as starting point, where clusters snap on dot-sites or coalesce with a certain probability depending on temperature and time.
Concerning the preparation of the oxide film several improvements are conceivable. The parameters for obtaining areas exhibiting the stripe phase should be

determined to avoid its formation. Small deviations from the preparation cycle could be an explanation. Therefore, it should be aimed for an automation of the preparation cycle or at least the heating treatments. Once a sufficient current for the filament is reached the temperature is controlled solely by the accelerating potential. A simple PID-driven control loop should be capable of increasing, decreasing and holding the desired temperature.

In the course of this thesis a new ultraviolet photoelectron spectroscopy setup was installed [Sci]. The package offers a microwave-driven helium discharge in order to get high intensity emission at $\gamma = 21.2\,\mathrm{eV}$ (HeIα) and $\gamma = 40.8\,\mathrm{eV}$ (HeIIα). A monochromatization is realized via an adjustable grating. The eventually ejected electrons can be analyzed with a micro-channel plate detector allowing fast band structure mapping or spacial resolution of the cluster spots in case of several spots deposited on one sample. The photoelectron setup can help revealing the electronic structure of the Ni_3Al substrate and the oxidized surface Al_2O_3. Of particular interest is the spectroscopy of deposited clusters in order to determine their electronic structure in contact with the surface on an averaging level. It may as well be feasible to observe quantized states analogously to clusters in a free beam. The HeIIα line also enables core level spectroscopy of a few cluster materials like lead.

Chapter 9

Appendix

9.1 Monte Carlo Simulation Source Codes

The Monte Carlo simulation source code is divided in three files: the random number generator "ran.h", a class file named "cluster.h" and the main file "simulation.cpp".
The random number generator was taken from Numerical Recipes [Pre07]. With a period of $3.1 \cdot 10^{57}$ it can be assumed that the numbers are uncorrelated. The constructor is seeded with an integer value (commonly the current timestamp). In addition to the generation of random 32 and 64 bit integers, it is also possible to obtain a double-precision floating number within the interval $[0, 1]$.

```
//*** ran.h ***//
#ifdef _MSC_VER
typedef unsigned __int64 Ullong;
#else
typedef unsigned long long int Ullong;
#endif
typedef unsigned int Uint;
typedef double Doub;

struct Ran {

   Ullong u,v,w;
   Ran(Ullong j) : v(4101842887655102017LL), w(1) {
      u = j ^ v; int64();
      v = u; int64();
      w = v; int64();
   }
```

```
18    inline Ullong int64() {
19       u = u * 2862933555777941757LL + 7046029254386353087LL;
20       v ^= v >> 17; v ^= v << 31; v ^= v >> 8;
21       w = 4294957665U*(w & 0xffffffff) + (w >> 32);
22       Ullong x = u ^ (u << 21); x ^= x >> 35; x ^= x << 4;
23       return (x + v) ^ w;
24    }
25    inline Doub doub() { return 5.42101086242752217E-20 * int64(); }
26    inline Uint int32() { return (Uint)int64(); }
27
28 };
```

The "cluster.h" file will be discussed in pieces. Firstly the needed headers should be included and some new variable types have to be defined in order to store the simulation data.

```
1  //*** cluster.h ***//
2
3  #include "ran.h"
4  #include <vector>
5  #include <time.h>
6  #include <math.h>
7  #include <iostream>
8  #include <sstream>
9  #include <fstream>
10
11 typedef std::vector <double> d1_vector;
12 typedef std::vector <d1_vector> d2_vector;
13 typedef std::vector <d2_vector> d3_vector;
```

Followed by the class itself with the constructor and some essential settings. All parameters are stored in private variables. Additionally the expected amount of clusters per frame and the number of grid points for the overlaying lattice are calculated. The user can also choose between the deposition of clusters on a free field (arbitrary positions), on a square lattice or a hexagonal lattice (positions constrained to grid points). If console output is enabled, the progress of the iterations is periodically written to the terminal. Furthermore, it is possible to save the real nearest-neighbor distances rather than the normalized ones.

```
15 class cluster {
16
17    public:
```

```
18  cluster(unsigned int size_, unsigned int iterations_, double
        coverage_, double diameter_, double lattice_const_):size(size_),
        iterations(iterations_), coverage(coverage_),
        diameter(diameter_), lattice_const(lattice_const_),
        random(time(0)), console_out(false), real_distances(false),
        mode(1), value(4) {
19    this->count = static_cast<int>((this->size * this->size) /
          (this->diameter * this->diameter) * this->coverage);
20    this->x_spots_hex =
          static_cast<int>(this->size/this->lattice_const);
21    this->y_spots_hex =
          static_cast<int>(this->size/this->lattice_const/pow(0.75,
          0.5));
22    this->x_spots_square =
          static_cast<int>(this->size/this->lattice_const);
23    this->y_spots_square =
          static_cast<int>(this->size/this->lattice_const);
24  }
25  void set_mode(unsigned int m) {
26    this->mode = m;
27    std::cout << "simulation mode set to " << m << std::endl;
28  }
29  void set_console_output() {
30    this->console_out = true;
31    std::cout << "console output enabled" << std::endl;
32  }
33  void set_real_distances() {
34    this->real_distances = true;
35    std::cout << "histogram output set to real distances" <<
          std::endl;
36  }
```

Each iteration starts with the spreading of clusters on the chosen grid. After completion the distance between nearest-neighboring clusters is calculated and stored as an item of the current frame. Finally, these distances are attached to a vector containing all results of the previous iterations/frames. If chosen, every 10th iteration will be displayed on the console. The resulting histogram is obtained by counting the occurrence of distances by means of the passed parameters and saved to file with the current settings as header lines. Additionally, it is possible to retrieve the entire data as three-dimensional vector. The data structure is visualized in figure 9.1.

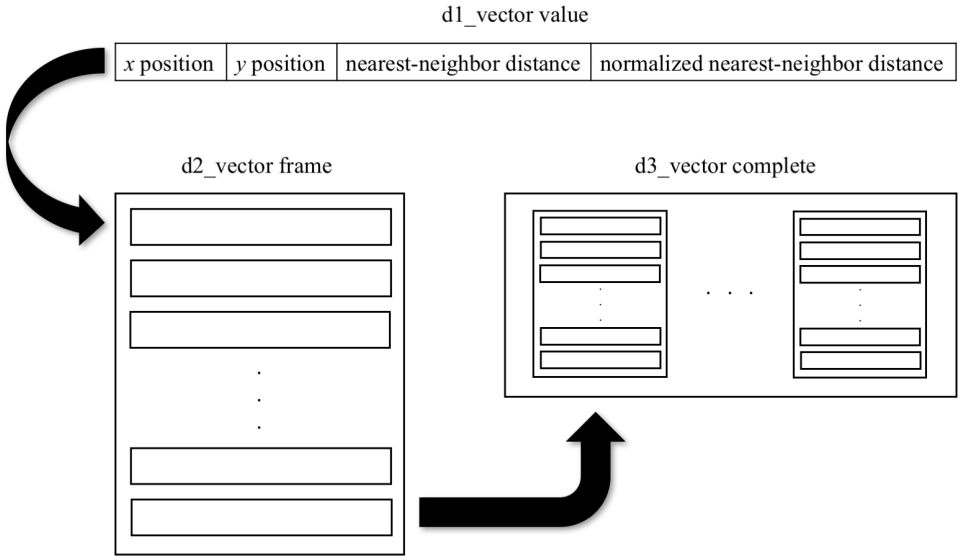

Figure 9.1: Data structure of used vectors. Each cluster has an x and y position as well as a distance to its nearest-neighbor (absolute and normalized). A frame consists of a certain amount of clusters with the mentioned properties. Each iteration generates a frame, which is a part of the complete simulation.

```
37    void iterate() {
38       this->complete.clear();
39       for(unsigned int i=0; i<this->iterations; i++) {
40          if(this->mode == 1) this->spread_free_field();
41          if(this->mode == 2) this->spread_hex_lattice();
42          if(this->mode == 3) this->spread_square_lattice();
43          this->calculate_nn();
44          this->complete.push_back(this->frame);
45          if(this->console_out == true && i%10 == 0) std::cout << "Mode:
                " << this->mode << " Iteration " << i+1 << " of " <<
                this->iterations << std::endl;
46       }
47    }
48    void hist_output(double hist_start_, double hist_end_, double
          hist_step_) {
49       this->hist_start = hist_start_;
50       this->hist_end = hist_end_;
51       this->hist_step = hist_step_;
52       int counter;
53       std::stringstream filename;
54       filename << "data/hist-" << this->size << "x" << this->size <<
             "." << this->iterations << "." << this->coverage;
```

```
55      if(this->mode == 1) filename << ".free";
56      if(this->mode == 2) filename << ".hex";
57      if(this->mode == 3) filename << ".square";
58      filename << ".dat";
59      std::fstream output(filename.str().c_str(), std::ios::out);
60      output << "# Positions and Distances for ";
61      if(this->mode == 1) output << "free field" << std::endl;
62      if(this->mode == 2) output << "hexagonal lattice" << std::endl;
63      if(this->mode == 3) output << "square lattice" << std::endl;
64      output << "# Size: " << this->size << "x" << this->size << "
            nm^2" << std::endl;
65      output << "# Iterations: " << this->iterations << std::endl;
66      output << "# Coverage: " << this->coverage*100 << " %" <<
            std::endl;
67      output << "# Cluster diameter: " << this->diameter << " nm" <<
            std::endl;
68      output << "# Lattice constant: " << this->lattice_const << " nm"
            << std::endl;
69      output << "#" << std::endl;
70      for(double d=this->hist_start; d<this->hist_end;
            d=d+this->hist_step) {
71         output << d << "\t";
72         counter = 0;
73         for(unsigned int i=0; i<this->complete.size(); i++) {
74            for(unsigned int j=0; j<this->complete[i].size(); j++) {
75               if(this->real_distances == false) {
                     if(this->complete[i][j][3] >= d &&
                     this->complete[i][j][3] < d+this->hist_step)
                     counter++; }
76               else { if(this->complete[i][j][2] >= d &&
                     this->complete[i][j][2] < d+this->hist_step)
                     counter++; }
77            }
78         }
79         output << counter << std::endl;
80      }
81      output.close();
82   }
83   d3_vector get_data() { return this->complete; }
```

The following variables and methods are declared as private within the cluster class. Each simulation mode has its own spread method, since the approach is

quite different. For a free field, it is sufficient to generate random double-precision floating numbers within the borders of the frame. Assuming a lattice only certain spots can be occupied. The nearest-neighbor distance is simply calculated by comparing the distances from one cluster to all other clusters of the frame and picking the minimum value.

```
84    private:
85    unsigned int size;
86    unsigned int iterations;
87    double coverage;
88    double diameter;
89    double lattice_const;
90    Ran random;
91    bool console_out;
92    bool real_distances;
93    unsigned int mode;
94    unsigned int count;
95    unsigned int x_spots_hex, y_spots_hex;
96    unsigned int x_spots_square, y_spots_square;
97    double hist_start, hist_end, hist_step;
98    d1_vector value;
99    d2_vector frame;
100   d3_vector complete;
101
102   void spread_free_field() {
103      this->frame.clear();
104      for(unsigned int i=0; i<this->count; i++) {
105         this->value[0] = this->random.doub()*this->size;
106         this->value[1] = this->random.doub()*this->size;
107         this->frame.push_back(this->value);
108      }
109   }
110   void spread_hex_lattice() {
111      this->frame.clear();
112      for(unsigned int i=0; i<this->y_spots_hex; i++) {
113         for(unsigned int j=0; j<this->x_spots_hex; j++) {
114            if(this->random.doub() <=
                  1.0*this->count/(this->x_spots_hex*this->y_spots_hex)) {
115               i%2 == 0 ? this->value[0] = j * this->lattice_const :
                     this->value[0] = (j + 0.5) * this->lattice_const;
116               this->value[1] = pow(0.75, 0.5) * i * this->lattice_const;
117               this->frame.push_back(this->value);
```

```
118             }
119          }
120       }
121    }
122    void spread_square_lattice() {
123       this->frame.clear();
124       for(unsigned int i=0; i<this->y_spots_square; i++) {
125          for(unsigned int j=0; j<this->x_spots_square; j++) {
126             if(this->random.doub() <= 1.0*this->count/
                   (this->x_spots_square*this->y_spots_square)) {
127                this->value[0] = j * this->lattice_const;
128                this->value[1] = i * this->lattice_const;
129                this->frame.push_back(this->value);
130             }
131          }
132       }
133    }
134    void calculate_nn() {
135       bool first_step;
136       double distance, temp_distance, diff_x, diff_y;
137       for(unsigned int i=0; i<this->frame.size(); i++) {
138          first_step = true;
139          distance = 0.0;
140          for(unsigned int j=0; j<this->frame.size(); j++) {
141             if(i != j) {
142                diff_x = fabs(this->frame[j][0] - this->frame[i][0]);
143                diff_y = fabs(this->frame[j][1] - this->frame[i][1]);
144                temp_distance = pow((pow(diff_x, 2.0) + pow(diff_y,
                      2.0)), 0.5);
145                if(first_step == true || temp_distance < distance) {
146                      distance = temp_distance;
147                }
148                first_step = false;
149             }
150          }
151          this->frame[i][2] = distance;
152          this->frame[i][3] = distance /
                pow((1.0*this->size*this->size/this->frame.size()), 0.5);
153       }
154    }
155 };
```

The source code of the main program "simulation.cpp" is structured as follows: Firstly the mandatory headers are included and the amount of passed parameters is checked. If this fails, the program quits and writes the correct usage to the terminal. To make use of rudimentary multiprocessor support the OpenMP [Dag98] package was also implemented. After initializing objects for the various spread modes the simulation is started by the "iterate()" method and finally, a histogram of the nearest-neighbor distances is generated. Due to OpenMP simulations for the three different modes are processed in parallel.

```
1  //*** simulation.cpp ***//
2
3  #include "cluster.h"
4  #include <stdlib.h>
5
6  int main(int argc, char *argv[]) {
7
8     if(argc != 6) {
9        std::cout << "****** bad or missing parameter ******" <<
             std::endl;
10       std::cout << "********** parameters are: ***********" <<
             std::endl;
11       std::cout << "** 1. size (integer)           **" << std::endl;
12       std::cout << "** 2. iterations (integer)     **" << std::endl;
13       std::cout << "** 3. coverage (0.1 means 10%) **" << std::endl;
14       std::cout << "** 4. cluster diameter (nm)    **" << std::endl;
15       std::cout << "** 5. lattice constant (nm)    **" << std::endl;
16       std::cout << "************************************" <<
             std::endl;
17       return -1;
18    }
19    unsigned const int size = atoi(argv[1]);
20    unsigned const int iterations = atoi(argv[2]);
21    const double coverage = atof(argv[3]);
22    const double diameter = atof(argv[4]);
23    const double lattice_const = atof(argv[5]);
24    #pragma omp parallel
25    {
26    #pragma omp sections nowait
27    {
28    #pragma omp section
29    {
30    cluster ff(size, iterations, coverage, diameter, lattice_const);
```

```
31    ff.set_mode(1);
32    ff.set_console_output();
33    ff.iterate();
34    ff.hist_output(0,2,0.01);
35    }
36    #pragma omp section
37    {
38    cluster hx(size, iterations, coverage, diameter, lattice_const);
39    hx.set_mode(2);
40    hx.set_console_output();
41    hx.iterate();
42    hx.hist_output(0,2,0.01);
43    }
44    #pragma omp section
45    {
46    cluster sq(size, iterations, coverage, diameter, lattice_const);
47    sq.set_mode(3);
48    sq.set_console_output();
49    sq.iterate();
50    sq.hist_output(0,2,0.01);
51    }
52    }
53    }
54
55 }
```

The code was tested on Debian 8 using the GNU Compiler Collection 4.9.2 [17b]. Simulations took place on a Dell OptiPlex 5040 Workstation with Windows 10 requiring compiling the code with mingw 4.6.3 [17d]. In both cases the compiler was called with the following flags:

```
g++ -m64 -fopenmp -Wall -o2 -o simulation simulation.cpp
```

This enables 64 bit support, parallel computing, compiler warnings and optimization level 2.

To generate the simulation data presented in section 6.2, about 6 days of computation on a Dell OptiPlex 5040 workstation were needed. The limiting factor was determined to be the system's memory. If not sufficient, the operating system makes use of paging and writes volatile data to the much ($\approx 10^3$) slower storage.

9.2 Movement of UHV System

When moving the UHV system described in chapter 4 to the new site, several things had to be considered. The basement offers two foundations, which should be decoupled from each other and the rest of the building. In order to check this decoupling vibration velocitiy measurements were performed in cooperation with Scienta Omicron. The raw data was saved as time dependent waveform audio (.wav) files. To obtain a frequency dependent spectrum the open source software audacity 2.1.2 [16] was used. Applying a Hann window function for Fourier analysis minimizes spectral leakage and leads to the data shown in figure 9.2.

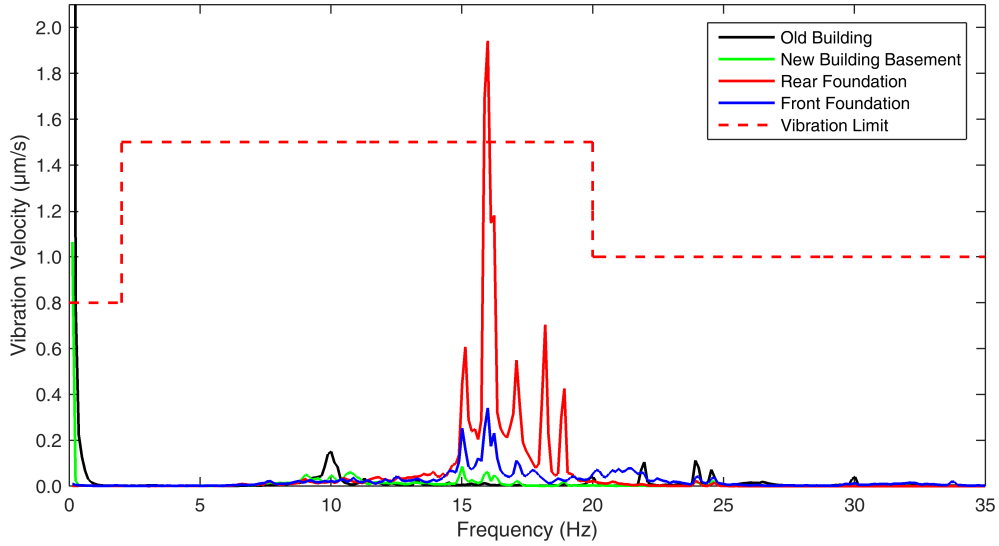

Figure 9.2: Vibration velocity measurement comparison for new and old site.

Both, the old site and the basement of the new site reveal extremely high vibration velocities below 1 Hz, which might be assigned to vibrations of the whole building, but might also be a measurement artifact. Modern buildings show vibrational maxima at frequencies in the range of 15 - 20 Hz, while people walking on the floor cause excitations near 1 - 3 Hz [Poh86]. Above 1 Hz both sites were well-suited for reliable STM operation concerning the limit given by Scienta Omicron (dashed line). The STM foundations show no vibration velocities below 1 Hz. However, the vibrations of the rear foundation violate the limits at about 16 Hz. For this reason the surface analysis system was placed on the front foundation to ensure high STM performance.

The new laboratory provides an additional room which houses the roughening pumps. This leads to a decrease in noise and also vibration level. The connection

between turbo-molecular pumps and roughening pumps are made through a new klein flange (KF) tube system that had to be planned and installed. The length is given by the installation location of the UHV system and the cluster beam facility respectively. The two turbo-molecular pumps of the VUV light source should share a roughening pump, as well as the two turbo-molecular pumps attached to the VUV monochromator and the preparation chamber. The manipulator sealing is independently pumped by a rotary vane pump. Two additional tubes are needed for the turbo-molecular pump of the mass selector and the two pumps attached to cryo chamber and cluster source. In figure 9.3 an early sketch of the tube system is shown to estimate the length of the various lines.

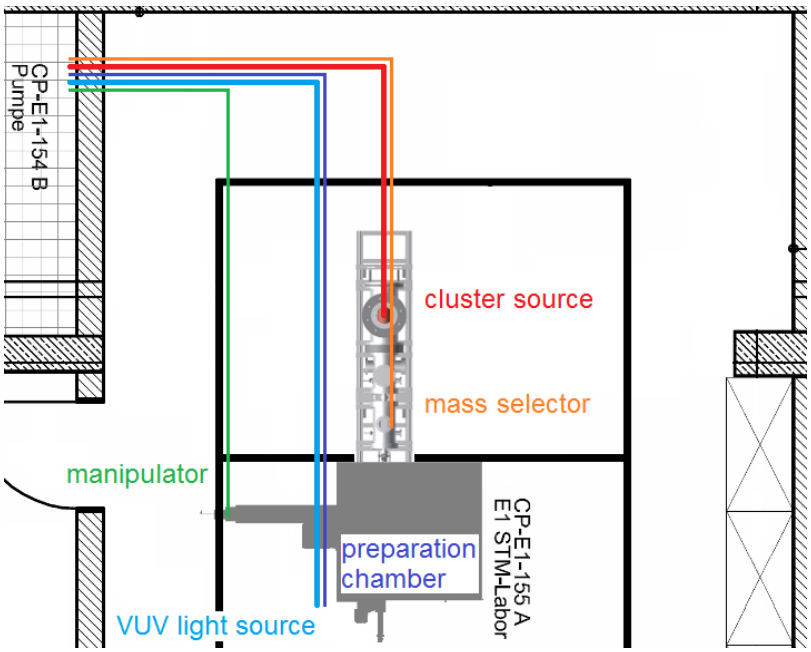

Figure 9.3: Sketch of the tube system at the ceiling (top view).

To introduce some flexibility the 90° bendings were planned as metallic hoses in contrast to stainless steel tubes for the straight parts. The pumping speed respectively the volume flow rate S decreases, if long tubes are used (see [Wut86] for detailed calculation of formulas used in this section). An effective pumping speed is described by the relationship

$$\frac{1}{S_{\text{eff}}} = \frac{1}{S} + \frac{1}{C} \quad .$$

The conductance C of a long circular shaped tube in ℓ/s can be calculated through

$$C = 12.1 \cdot \frac{d^3}{l} \quad , \tag{9.1}$$

where d is the inner diameter and l is the length of the tube (both in cm). Apparently, C mainly depends on the inner diameter d. Therefore, pumping lines with estimated high gas amount (cluster source and VUV light source) were chosen to be of 50 mm inner diameter, in contrast to 25 mm used otherwise. The effect of smooth bendings on the conductance is negligible, i.e. the complete distance from roughening pump to turbo-molecular pump can be regarded as a long tube and equation (9.1) holds. The process pressure p_{vac} and volume flow rate of the high vacuum pump S_{vac} have to be in balance with the foreline pressure p_{foreline} and the volume flow rate of the roughening pump S_{foreline}. Hence, the minimum volume flow rate on foreline side can be calculated through

$$S_{\text{foreline}} = \frac{p_{\text{vac}} \cdot S_{\text{vac}}}{p_{\text{foreline}}} \quad .$$

Turbo-molecular pump operation is only possible below a certain foreline pressure. Table 9.1 contains therefore an estimation of the required pumping speed for each pumping line. $L_{1\,\text{m}}$ refers to a 1 m connection between turbo-molecular pump and roughening pump with 25 mm diameter as it is the common case, if foreline pumps are placed next to the system in the same room. The Manipulator requires solely the presence of a low vacuum to reduce leakage through the sealing.
As a rule of thumb the pumping speed should be tripled to compensate for the longer vacuum line. However, even with heavy gas load, volume flow rates of $\approx 32\,\text{m}^3/\text{h}$ are not exceeded. The additional volume of the tube system prolonged the time to evacuate the UHV chamber by less than 1 minute. These amounts are easily manageable with available pumps. Detailed Drawings of the new foreline system visualized with Autodesk Inventor are shown in figures 9.4, 9.5 and 9.6.

Pumping line	#1	#2	#3	#4
p_{vac} (10^{-3} mbar)	50	10	0.01	0.10
S_{vac} (ℓ/s)	150	600	250	450
p_{foreline} (mbar)	9	6	8	8
S_{foreline} ($10^{-2}\,\ell/\text{s}$)	83	120	0.03	0.56
Tube Length (m)	12.8	10.9	12.0	12.9
Tube Diameter (cm)	5.0	5.0	2.5	2.5
Tube Volume (ℓ)	100.5	85.6	23.6	25.3
$L_{1\,\text{m}}$ (ℓ/s)	1.89	1.89	1.89	1.89
S_{pump} (m^3/h)	5.4	11.8	$1.1 \cdot 10^{-3}$	$20 \cdot 10^{-3}$
L_{new} (ℓ/s)	1.18	1.39	0.16	0.15
S_{pump} (m^3/h)	10.2	32.0	$1.1 \cdot 10^{-3}$	$21 \cdot 10^{-3}$

Table 9.1: Required pumping speed and tube parameters for the new foreline system. #1 denotes the line for the VUV light source, #2 corresponds to the cluster source, #3 represents the mass selector tube and finally, #4 is the preparation chamber line.

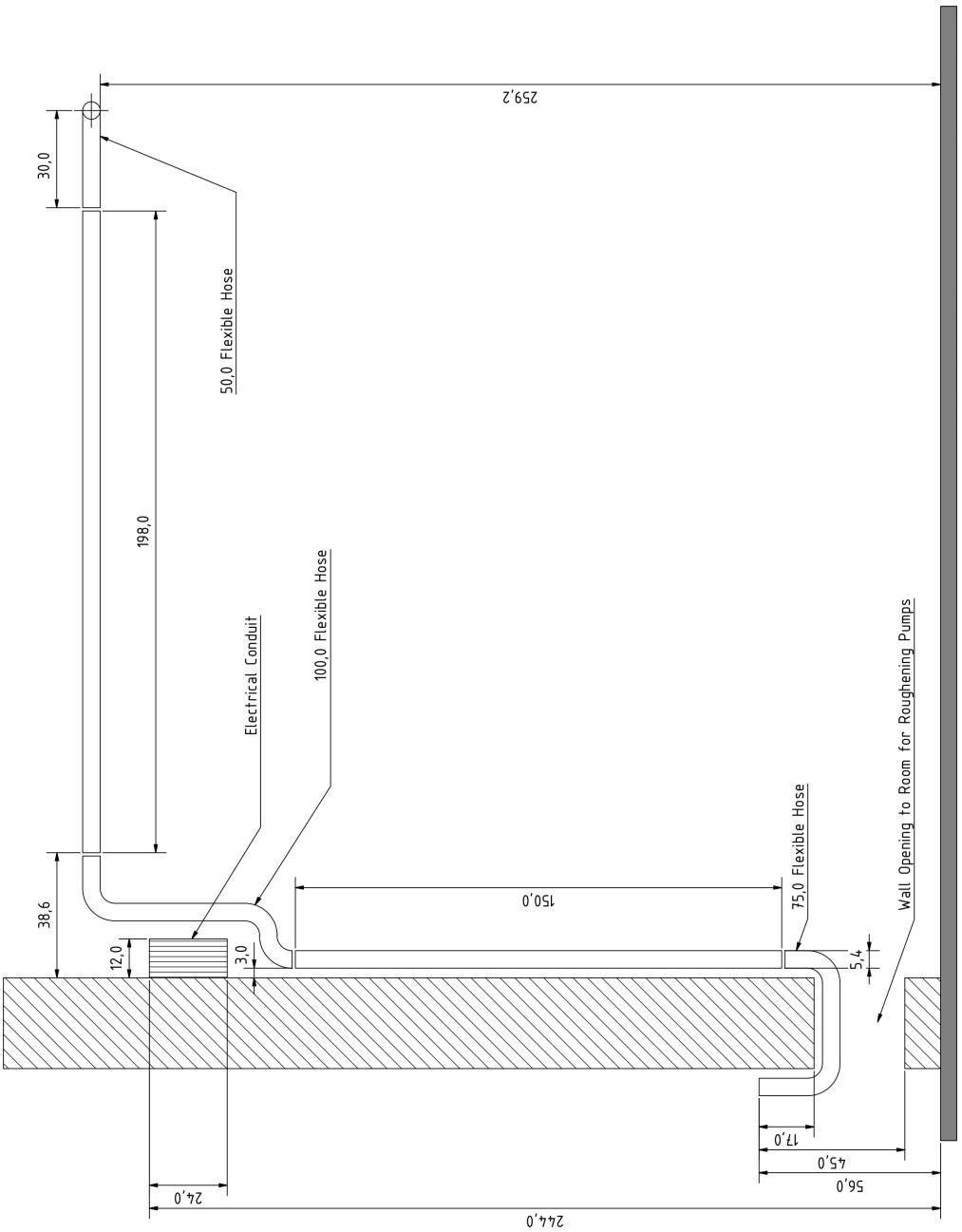

Figure 9.4: Drawing of the tube system (front view).

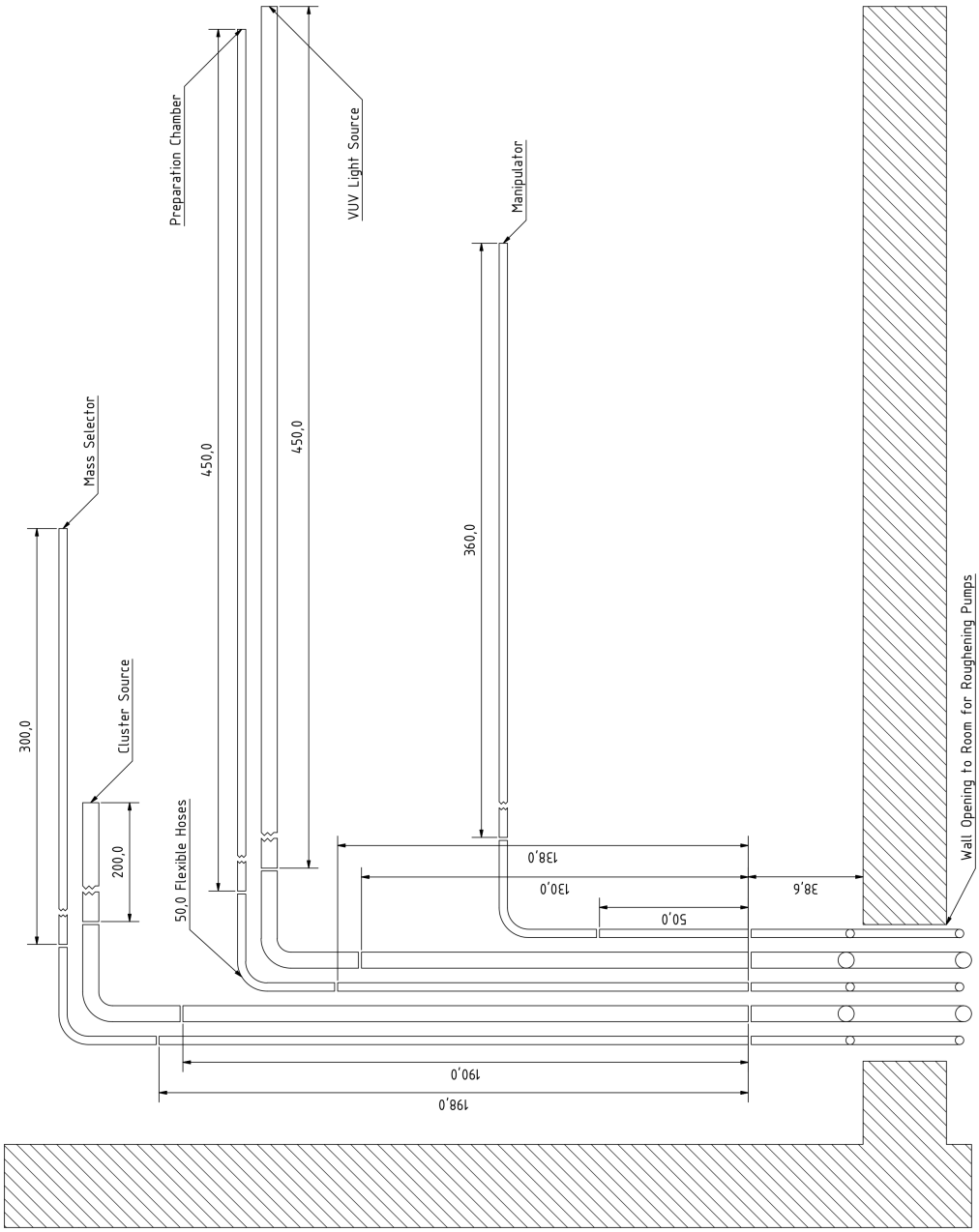

Figure 9.5: Drawing of the tube system (top view).

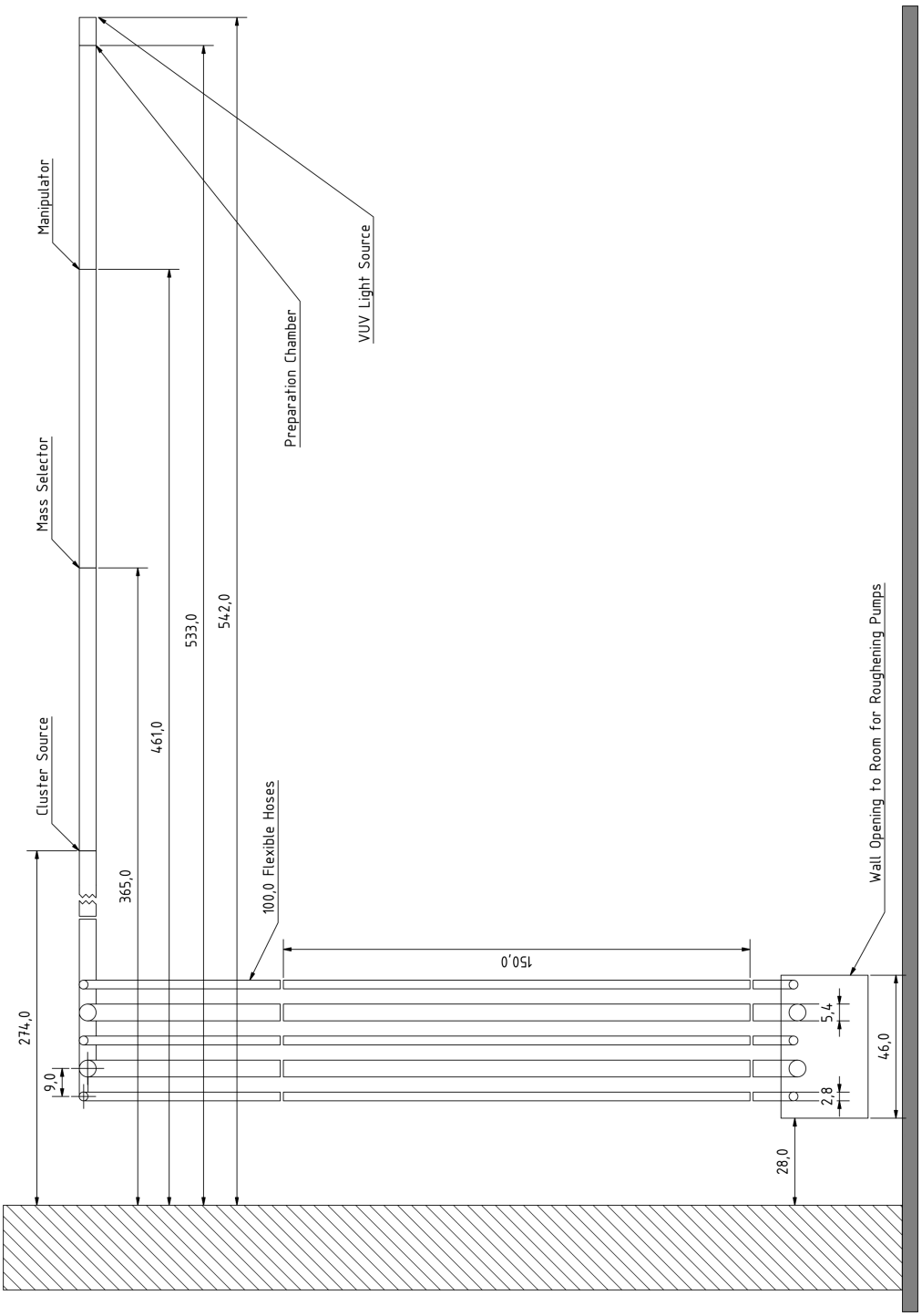

Figure 9.6: Drawing of the tube system (side view).

9.3 Deposition Parameters

Experiment No.	1	2		3	
Spot No.	1	1	2	1	2
Cluster size (atoms)	55	309	55	13	55
Mass (u)	3620	20128	3596	858	3581
Current (pA)	2.6	6.1	4.6	12.1	30.5
Amount (pAmin)	18	14	16	17	14
Deposition time (s)	432	140	210	84	28
Wait time t_w	13	7	7	16	7
Sample bias (V)	-13	-9	-13	-12	-15
Temperature (K)	77	79	79	78	78
x (mm)	23.90	23.45	23.45	22.21	22.21
y (mm)	12.00	11.50	11.50	11.62	11.62
z (mm)	181.53	179.30	182.50	178.86	182.42
He flux (sccm)	120	200		200	
Ar flux (sccm)	100	100		100	
Magnetron Power (W)	12.0	12.0		12.0	
Iris (V)	2.1	2.5		2.1	
Ring (V)	3.1	3.0		7.7	
Skimmer (V)	0.0	0.9		4.3	
A1 (V)	-79.1	-50.3		-77.9	
A2 (V)	-584.3	-505.8		-484.0	
A3 (V)	-41.3	-49.8		-79.4	
X-Deflector (V)	4.0	-1.0		5.0	
Y-Deflector (V)	0.7	0.6		0.7	
Focus (V)	-220.1	-236.0		-238.6	
HV-Out (V)	-511.3	-492.3		-502.1	
M-Tube (V)	-192.0	-246.0		-247.0	
Y+ (V)	-934.6	-949.4		-944.3	
Y- (V)	-919.5	-920.8		-911.0	
D1 (V)	-985.6	-984.3		-995.6	
D2 (V)	-294.3	-290.0		-279.7	
D3 (V)	-908.3	-904.5		-904.1	
Aperture (V)	-623.4	-500.0		-459.9	

Table 9.2: Deposition parameters for experiments within this thesis.

Bibliography

[16] *Audacity - Free, open source, cross-platform audio software for multi-track recording and editing.* 2016. URL: http://www.audacityteam.org (visited on 12/05/2016) (cit. on p. 86).

[17a] *AG v. Issendorff.* 2017. URL: http://cluster.physik.uni-freiburg.de (visited on 10/27/2017) (cit. on p. 20).

[17b] *GCC, the GNU Compiler Collection - GNU Project.* 2017. URL: https://gcc.gnu.org (visited on 06/08/2017) (cit. on p. 85).

[17c] *Gnuplot.* 2017. URL: http://www.gnuplot.info (visited on 09/18/2017) (cit. on p. 34).

[17d] *MinGW - Minimalist GNU for windows.* 2017. URL: http://www.mingw.org (visited on 06/08/2017) (cit. on p. 85).

[17e] *UMR 7325 Conrad Becker.* 2017. URL: http://www.cinam.univ-mrs.fr/cinam/spip.php?page=perso&name=becker (visited on 11/29/2017) (cit. on p. 27).

[Alb94] O. Albrektsen, H. W. M. Salemink, K. A. Morch, and A. R. Thölen. "Reliable tip preparation for high-resolution scanning tunneling microscopy". In: *Journal of Vacuum Science & Technology B: Microelectronics and Nanometer Structures Processing, Measurement, and Phenomena* **12**. (1994), pp. 3187–3190. DOI: 10.1116/1.587497. (Cit. on p. 18).

[Ana10] J. S. Ananta, B. Godin, R. Sethi, L. Moriggi, X. Liu, R. E. Serda, R. Krishnamurthy, R. Muthupillai, R. D. Bolskar, L. Helm, M. Ferrari, L. J. Wilson, and P. Decuzzi. "Geometrical confinement of gadolinium-based contrast agents in nanoporous particles enhances T_1 contrast". In: *Nature Nanotechnology* **5** (2010), pp. 815–821. DOI: 10.1038/nnano.2010.203. (Cit. on p. 2).

[Ash76] N. W. Ashcroft and D. N. Mermin. *Solid State Physics*. Saunders College Publishing, Philadelphia, 1976, pp. 29–83 (cit. on pp. 55, 73).

[Bar15] I. Barke, H. Hartmann, D. Rupp, L. Flückiger, M. Sauppe, M. Adolph, S. Schorb, C. Bostedt, R. Treusch, C. Peltz, S. Bartling, T. Fennel, K.-H. Meiwes-Broer, and T. Müller. "The 3D-architecture of individual free silver nanoparticles captured by X-ray scattering". In: *Nature Communications* **6** (2015), p. 6187. doi: 10.1038/ncomms7187. (Cit. on p. 6).

[Bar92] U. Bardi, A. Atrei, and G. Rovida. "Initial stages of oxidation of the Ni_3Al alloy: structure and composition of the aluminum oxide overlayer studied by XPS, LEIS and LEED". In: *Surface Science* **268**. (1992), pp. 87–97. doi: 10.1016/0039-6028(92)90952-3. (Cit. on pp. 1, 31).

[Bec98] C. Becker, J. Kandler, H. Raaf, R. Linke, T. Pelster, M. Dräger, M. Tanemura, and K. Wandelt. "Oxygen adsorption and oxide formation on Ni_3Al (111)". In: *Journal of Vacuum Science & Technology A: Vacuum, Surfaces, and Films* **16**. (1998), pp. 1000–1005. doi: 10.1116/1.581221. (Cit. on p. 27).

[Bin82] G. Binnig, H. Rohrer, Ch. Gerber, and E. Weibel. "Surface Studies by Scanning Tunneling Microscopy". In: *Physical Review Letters* **49** (1982), pp. 57–61. doi: 10.1103/PhysRevLett.49.57. (Cit. on p. 11).

[Bin85] G. Binnig, K. H. Frank, H. Fuchs, N. Garcia, B. Reihl, H. Rohrer, F. Salvan, and A. R. Williams. "Tunneling Spectroscopy and Inverse Photoemission: Image and Field States". In: *Physical Review Letters* **55** (1985), pp. 991–994. doi: 10.1103/PhysRevLett.55.991. (Cit. on p. 55).

[Bor26] M. Born. "Quantenmechanik der Stoßvorgänge". In: *Zeitschrift für Physik A Hadrons and Nuclei* **38**. (1926), pp. 803–827 (cit. on p. 13).

[Bra93] M. Brack. "The physics of simple metal clusters: self-consistent jellium model and semiclassical approaches". In: *Reviews of Modern Physics* **65** (1993), pp. 677–732. doi: 10.1103/RevModPhys.65.677. (Cit. on p. 55).

[Buc10] A. Buchsbaum, M. De Santis, H. C. N. Tolentino, M. Schmid, and P. Varga. "Highly ordered Pd, Fe, and Co clusters on alumina on $Ni_3Al(111)$". In: *Physical Review B* **81** (2010), p. 115420. doi: 10.1103/PhysRevB.81.115420. (Cit. on p. 1).

[Car97] D. L. Carroll, M. Wagner, M. Rühle, and D. A. Bonnell. "Schottky-barrier formation at nanoscale metal-oxide interfaces". In: *Physical Review B* **55** (15 1997), pp. 9792–9799. doi: 10.1103/PhysRevB.55.9792. (Cit. on p. 60).

[Col09] P. Colomban. "The Use of Metal Nanoparticles to Produce Yellow, Red and Iridescent Colour, from Bronze Age to Present Times in Lustre Pottery and Glass: Solid State Chemistry, Spectroscopy and Nanostructure". In: *Journal of Nano Research* **8** (2009), pp. 109–132. doi: 10.4028/www.scientific.net/JNanoR.8.109. (Cit. on p. 1).

[Dag98] L. Dagum and R. Menon. "OpenMP: An Industry-Standard API for Shared-Memory Programming". In: *IEEE Computational Science and Engineering* **5**. (1998), pp. 46–55. doi: 10.1109/99.660313. (Cit. on p. 84).

[Dav27] C. Davisson and L. H. Germer. "The Scattering of Electrons by a Single Crystal of Nickel". In: *Nature* **119** (1927), pp. 558–560. doi: 10.1038/119558a0. (Cit. on p. 13).

[Deg04] S. Degen, C. Becker, and K. Wandelt. "Thin alumina films on $Ni_3Al(111)$: A template for nanostructured Pd cluster growth". In: *Faraday Discussions* **125** (2004), pp. 343–356. doi: 10.1039/B303244B. (Cit. on pp. 2, 52).

[Deg05] S. Degen, A. Krupski, M. Kralj, A. Langner, C. Becker, M. Sokolowski, and K. Wandelt. "Determination of the coincidence lattice of an ultra thin Al_2O_3 film on $Ni_3Al(111)$". In: *Surface Science Letters* **576**. (2005), pp. L57–L64. doi: 10.1016/j.susc.2004.12.020. (Cit. on pp. 31, 32).

[Deg06] S. Degen. "Aufbau eines Tieftemperaturrastertunnelmikroskops und Messungen auf $Ni_3Al(111)$". PhD thesis. Rheinische Friedrich-Wilhelms-Universität Bonn, 2006 (cit. on pp. 32, 55, 59, 62).

[Duf09] S. Duffe. "Thermally activated processes and electronic properties of size selected Ag clusters and grown metal islands on C_{60} functionalized surfaces". PhD thesis. Technische Universität Dortmund, 2009 (cit. on p. 20).

[Duf10] S. Duffe, N. Grönhagen, L. Patryarcha, B. Sieben, C. Yin, B. von Issendorff, M. Moseler, and H. Hövel. "Penetration of thin C_{60} films by metal nanoparticles". In: *Nature Nanotechnology* **5** (2010), p. 335. doi: 10.1038/nnano.2010.45. (Cit. on p. 64).

[Ech81] O. Echt, K. Sattler, and E. Recknagel. "Magic Numbers for Sphere Packings: Experimental Verification in Free Xenon Clusters". In: *Physical Review Letters* **47** (1981), pp. 1121–1124. doi: 10.1103/PhysRevLett.47.1121. (Cit. on p. 6).

[Ewa13] P. P. Ewald. "Zur Theorie der Interferenzen der Röntgenstrahlen in Kristallen". In: *Physikalische Zeitschrift* **14**. (1913), pp. 465–472 (cit. on p. 14).

[Fla92] P. Flajolet, D. Gardy, and L. Thimonier. "Birthday paradox, coupon collectors, caching algorithms and self-organizing search". In: *Discrete Applied Mathematics* **39**. (1992), pp. 207–229. doi: 10.1016/0166-218X(92)90177-C. (Cit. on p. 49).

[Flo15] R. Floegel. "Untersuchung massenselektierter Kupfer-Cluster auf einem dünnen Oxidfilm mittels STM und LEED". MA thesis. Technische Universität Dortmund, 2015 (cit. on p. 37).

[Flö15] D. Flötotto, Z. M. Wang, and E. J. Mittemeijer. "On the structural development during ultrathin amorphous Al_2O_3 film growth on Al(111) and Al(100) surfaces by thermal oxidation". In: *Surface Science* **633**. (2015), pp. 1–7. doi: 10.1016/j.susc.2014.11.008. (Cit. on p. 27).

[Fra96] R. Franchy, J. Masuch, and P. Gassmann. "The oxidation of the NiAl(111) surface". In: *Applied Surface Science* **93**. (1996), pp. 317–327. doi: 10.1016/0169-4332(95)00333-9. (Cit. on p. 27).

[Fri13] W. Friedrich, P. Knipping, and M. Laue. "Interferenzerscheinungen bei Röntgenstrahlen". In: *Annalen der Physik* **346**. (1913), pp. 971–988 (cit. on p. 14).

[Fuk13] Y. Fukamori, M. König, B. Yoon, B. Wang, F. Esch, U. Heiz, and U. Landman. "Fundamental Insight into the Substrate-Dependent Ripening of Monodisperse Clusters". In: *ChemCatChem* **5**. (2013), pp. 3330–3341. doi: 10.1002/cctc.201300250. (Cit. on p. 10).

[Fuk16] Y. Fukamori. "Static and dynamic characterization of size-selected cluster diffusion and ripening on periodically wettable surfaces". PhD thesis. Technische Universität München, 2016 (cit. on p. 10).

[Ful87] T. A. Fulton and G. J. Dolan. "Observation of single-electron charging effects in small tunnel junctions". In: *Physical Review Letters* **59** (1987), pp. 109–112. DOI: 10.1103/PhysRevLett.59.109. (Cit. on p. 56).

[Gri07] S. Gritschneder, S. Degen, C. Becker, K. Wandelt, and M. Reichling. "Atomic structure of a stripe phase on $Al_2O_3/Ni_3Al(111)$ revealed by scanning force microscopy". In: *Physical Review B* **76** (2007), p. 014123. DOI: 10.1103/PhysRevB.76.014123. (Cit. on p. 69).

[Grö11] N. Grönhagen. "Cluster-Surface Interaction of Mass Selected Ag Clusters with Graphite, Gold and C_{60} Functionalized Surfaces". PhD thesis. Technische Universität Dortmund, 2011 (cit. on pp. 26, 38).

[Grö12] N. Grönhagen, T. T. Järvi, N. Miroslawski, H. Hövel, and M. Moseler. "Decay Kinetics of Cluster-Beam-Deposited Metal Particles". In: *The Journal of Physical Chemistry C* **116**. (2012), pp. 19327–19334. DOI: 10.1021/jp305089d. (Cit. on p. 9).

[Gus18] P. Gust. "Herstellung großer massenselektierter Cluster unter Verbesserung eines Flugzeit-Massenselektors". MA thesis. Technische Universität Dortmund, 2018 (cit. on p. 25).

[Hab06] H. Haberland, K. Kleinermanns, and F. Träger. "Cluster". In: *Bergmann Schäfer, Lehrbuch der Experimentalphysik, Band 5, Gase, Nanosysteme, Flüssigkeiten.* Walter de Guyter GmbH & Co. KG, 2006, pp. 817–822 (cit. on pp. 5, 7).

[Hab91] H. Haberland, M. Karrais, and M. Mall. "A new type of cluster and cluster ion source". In: *Zeitschrift für Physik D Atoms, Molecules and Clusters* **20**. (1991), pp. 413–415. DOI: 10.1007/BF01544025. (Cit. on p. 21).

[Hab94] H. Haberland, M. Mall, M. Moseler, Y. Qiang, T. Reiners, and Y. Thurner. "Filling of micron-sized contact holes with copper by energetic cluster impact". In: *Journal of Vacuum Science & Technology A: Vacuum, Surfaces, and Films* **12**. (1994), pp. 2925–2930. DOI: 10.1116/1.578967. (Cit. on p. 21).

[Ham06] G. Hamm, C. Barth, C. Becker, K. Wandelt, and C. R. Henry. "Surface Structure of an Ultrathin Alumina Film on $Ni_3Al(111)$: A Dynamic Scanning Force Microscopy Study". In: *Physical Review*

Letters **97** (2006), p. 126106. DOI: 10.1103/PhysRevLett.97.126106. (Cit. on p. 27).

[Han91] A. E. Hanna and M. Tinkham. "Variation of the Coulomb staircase in a two-junction system by fractional electron charge". In: *Physical Review B* **44** (1991), pp. 5919–5922. DOI: 10.1103/PhysRevB.44.5919. (Cit. on p. 56).

[Hei14] K. Heinz. "Electron Based Methods: 3.2.1 Low-Energy Electron Diffraction (LEED)". In: *Surface and Interface Science, Volume 1: Concepts and Methods*. Wiley-VCH Verlag GmbH & Co. KGaA, 2014, pp. 93–150. DOI: 10.1002/9783527680535.ch4. (Cit. on pp. 14, 15).

[Hei99] U. Heiz, A. Sanchez, S. Abbet, and W.-D. Schneider. "Catalytic Oxidation of Carbon Monoxide on Monodispersed Platinum Clusters: Each Atom Counts". In: *Journal of the American Chemical Society* **121**. (1999), pp. 3214–3217. DOI: 10.1021/ja9836l. (Cit. on p. 8).

[Höv98] H. Hövel, T. Becker, D. Funnemann, B. Grimm, C. Quitmann, and B. Reihl. "High-resolution photoemission combined with low-temperature STM". In: *Journal of Electron Spectroscopy and Related Phenomena* **88-91** (1998), pp. 1015–1020. DOI: 10.1016/S0368-2048(97)00114-X. (Cit. on p. 17).

[Hug05] M. D. Hughes, Y.-J. Xu, P. Jenkins, P. McMorn, P. Landon, D. I. Enache, A. F. Carley, G. A. Attard, G. J. Hutchings, F. King, E. H. Stitt, P. Johnston, K. Griffin, and C. J. Kiely. "Tunable gold catalysts for selective hydrocarbon oxidation under mild conditions". In: *Nature* **437** (2005), pp. 1132–1135. DOI: 10.1038/nature04190. (Cit. on p. 1).

[Ira06] T. Irawan. "Geometric and Electronic Properties of Size-Selected Metal Clusters on Surfaces". PhD thesis. Universität Dortmund, 2006 (cit. on pp. 20, 22, 24).

[Iss99] B. von Issendorff and R. E. Palmer. "A new high transmission infinite range mass selector for cluster and nanoparticle beams". In: *Review of Scientific Instruments* **70**. (1999), pp. 4497–4501. DOI: 10.1063/1.1150102. (Cit. on p. 22).

[Jud05] K. Judai, A. S. Worz, S. Abbet, J.-M. Antonietti, U. Heiz, A. Del Vitto, L. Giordano, and G. Pacchioni. "Acetylene trimerization on Ag, Pd and Rh atoms deposited on MgO thin films". In:

Physical Chemistry Chemical Physics **7** (2005), pp. 955–962. DOI: 10.1039/B414399J. (Cit. on p. 66).

[Kho13] H. KHOSRAVIAN, Y. LEI, A. UHL, M. TRENARY, and R. J. MEYER. "Nucleation behavior of supported Rh nanoparticles fabricated from $Rh(CO)_2(acac)$ on $Al_2O_3/Ni_3Al(111)$". In: *Chemical Physics Letters* **555** (2013), pp. 7–11. DOI: 10.1016/j.cplett.2012.10.086. (Cit. on p. 1).

[Kly00] D. KLYACHKO and D. M. CHEN. "Cluster shapes in STM images of isolate clusters and cluster materials". In: *Surface Science* **446**. (2000), pp. 98–102. DOI: 10.1016/S0039-6028(99)01110-3. (Cit. on p. 39).

[Kni84] W. D. KNIGHT, K. CLEMENGER, W. A. DE HEER, W. A. SAUNDERS, M. Y. CHOU, and M. L. COHEN. "Electronic Shell Structure and Abundances of Sodium Clusters". In: *Physical Review Letters* **52** (1984), pp. 2141–2143. DOI: 10.1103/PhysRevLett.52.2141. (Cit. on p. 7).

[Kni92] M. B. KNICKELBEIN. "Electronic shell structure in the ionization potentials of copper clusters". In: *Chemical Physics Letters* **192**. (1992), pp. 129–134. DOI: 10.1016/0009-2614(92)85440-L. (Cit. on p. 57).

[Kno02] N. KNORR, H. BRUNE, M. EPPLE, A. HIRSTEIN, M. A. SCHNEIDER, and K. KERN. "Long-range adsorbate interactions mediated by a two-dimensional electron gas". In: *Physical Review B* **65** (2002), p. 115420. DOI: 10.1103/PhysRevB.65.115420. (Cit. on p. 49).

[Kos07] O. KOSTKO, B. HUBER, M. MOSELER, and B. VON ISSENDORFF. "Structure Determination of Medium-Sized Sodium Clusters". In: *Physical Review Letters* **98** (2007), p. 043401. DOI: 10.1103/PhysRevLett.98.043401. (Cit. on p. 8).

[Kre05] M. KREMS, J. ZIRBEL, M. THOMASON, and R. D. DUBOIS. "Channel electron multiplier and channelplate efficiencies for detecting positive ions". In: *Review of Scientific Instruments* **76**. (2005), p. 093305. DOI: 10.1063/1.2052052. (Cit. on p. 25).

[Lan87] N. D. LANG. "Resistance of a one-atom contact in the scanning tunneling microscope". In: *Physical Review B* **36** (1987), pp. 8173–8176. DOI: 10.1103/PhysRevB.36.8173. (Cit. on pp. 57–59).

[Leh06] A. Lehnert, A. Krupski, S. Degen, K. Franke, R. Decker, S. Rusponi, M. Kralj, C. Becker, H. Brune, and K. Wandelt. "Nucleation of ordered Fe islands on $Al_2O_3/Ni_3Al(111)$". In: *Surface Science* **600**. (2006), pp. 1804–1808. doi: 10.1016/j.susc.2006.02.013. (Cit. on p. 75).

[Lim06] D. C. Lim, R. Dietsche, M. Bubek, G. Ganteför, and Y. D. Kim. "Oxidation and Reduction of Mass-Selected Au Clusters on SiO_2/Si". In: *ChemPhysChem* **7**. (2006), pp. 1909–1911. doi: 10.1002/cphc.200600285. (Cit. on p. 2).

[Mac62] A. L. Mackay. "A dense non-crystallographic packing of equal spheres". In: *Acta Crystallographica* **15**. (1962), pp. 916–918. doi: 10.1107/S0365110X6200239X. (Cit. on p. 6).

[Mar03] T. Maroutian, S. Degen, C. Becker, K. Wandelt, and R. Berndt. "Superstructures and coincidences of a thin oxide film on a metallic substrate: A STM study". In: *Physical Review B* **68** (2003), p. 155414. doi: 10.1103/PhysRevB.68.155414. (Cit. on pp. 31, 32).

[Mes00] S. Messerli, S. Schintke, K. Morgenstern, A. Sanchez, U. Heiz, and W.-D. Schneider. "Imaging size-selected silicon clusters with a low-temperature scanning tunneling microscope". In: *Surface Science* **465**. (2000), pp. 331–338. doi: 10.1016/S0039-6028(00)00722-6. (Cit. on p. 63).

[Mir13] N. Miroslawski. "Ultraviolet photoelectron spectroscopy and scanning tunneling microscopy of silver and copper clusters on HOPG, noble metals and rare gas layers". PhD thesis. Technische Universität Dortmund, 2013 (cit. on p. 63).

[Neč12] D. Nečas and P. Klapetek. "Gwyddion: an open-source software for SPM data analysis". In: *Open Physics* **10**. (2012), pp. 181–188. doi: 10.2478/s11534-011-0096-2. (Cit. on p. 27).

[Par00] H. Park, J. Park, A. K. L. Lim, E. H. Anderson, A. P. Alivisatos, and P. L. McEuen. "Nanomechanical oscillations in a single-C_{60} transistor". In: *Nature* **407** (2000), pp. 57–60. doi: 10.1038/35024031. (Cit. on p. 2).

[Pas09] T. Passerat de Silans, I. Maurin, P. Chaves de Souza Segundo, S. Saltiel, M.-P. Gorza, M. Ducloy, D. Bloch, D. de Sousa Meneses, and P. Echegut. "Temperature dependence of the dielectric permittivity of CaF_2, BaF_2 and Al_2O_3: application

to the prediction of a temperature-dependent van der Waals surface interaction exerted onto a neighbouring $Cs(8P_{3/2})$ atom". In: *Journal of Physics: Condensed Matter* **21**. (2009), p. 255902. DOI: 10.1088/0953-8984/21/25/255902. (Cit. on p. 57).

[Plo07] H.-C. Ploigt, C. Brun, M. Pivetta, F. Patthey, and W.-D. Schneider. "Local work function changes determined by field emission resonances: NaCl/Au(100)". In: *Physical Review B* **76** (2007), p. 195404. DOI: 10.1103/PhysRevB.76.195404. (Cit. on p. 55).

[Poh86] D. W. Pohl. "Some design criteria in scanning tunneling microscopy". In: *IBM Journal of Research and Development* **30**. (1986), pp. 417–427. DOI: 10.1147/rd.304.0417 (cit. on p. 86).

[Pre07] W. H. Press, S. A. Teukolsky, W. T. Vetterling, and B. P. Flannery. *Numerical Recipes 3rd Edition: The Art of Scientific Computing*. Cambridge University Press, 2007, p. 342 (cit. on p. 77).

[Ral95] D. C. Ralph, C. T. Black, and M. Tinkham. "Spectroscopic Measurements of Discrete Electronic States in Single Metal Particles". In: *Physical Review Letters* **74** (1995), pp. 3241–3244. DOI: 10.1103/PhysRevLett.74.3241. (Cit. on p. 55).

[Rav06] R. Ravindran, K. Gangopadhyay, S. Gangopadhyay, N. Mehta, and N. Biswas. "Permittivity enhancement of aluminum oxide thin films with the addition of silver nanoparticles". In: *Applied Physics Letters* **89**. (2006), p. 263511. DOI: 10.1063/1.2425010. (Cit. on p. 57).

[Ros99a] A. Rosenhahn, J. Schneider, C. Becker, and K. Wandelt. "The formation of Al_2O_3-layers on $Ni_3Al(111)$". In: *Applied Surface Science* **142**. (1999), pp. 169–173. DOI: 10.1016/S0169-4332(98)00669-2. (Cit. on p. 27).

[Ros99b] A. Rosenhahn, J. Schneider, J. Kandler, C. Becker, and K. Wandelt. "Interaction of oxygen with $Ni_3Al(111)$ at 300 K and 1000 K". In: *Surface Science* **433-435**. (1999), pp. 705–710. DOI: 10.1016/S0039-6028(99)00126-0. (Cit. on p. 62).

[Sap06] S. Sapmaz, P. Jarillo-Herrero, Y. M. Blanter, C. Dekker, and H. S. J. van der Zant. "Tunneling in Suspended Carbon Nanotubes Assisted by Longitudinal Phonons". In: *Physical Review Letters* **96** (2006), p. 026801. DOI: 10.1103/PhysRevLett.96.026801. (Cit. on p. 56).

[Sch07] M. Schmid, G. Kresse, A. Buchsbaum, E. Napetschnig, S. Gritschneder, M. Reichling, and P. Varga. "Nanotemplate with Holes: Ultrathin Alumina on $Ni_3Al(111)$". In: *Physical Review Letters* **99** (2007), p. 196104. DOI: 10.1103/PhysRevLett.99.196104. (Cit. on p. 32).

[Sci] Scienta Omicron R3000 and VUV5k. *Specifications are taken from the respective manuals* (cit. on p. 76).

[Sie07] B. Sieben. "Rastertunnelmikroskopie an Clustersystemen". Dipl thesis. Universität Dortmund, 2007 (cit. on p. 48).

[Sol86] J. M. Soler, A. M. Baro, N. García, and H. Rohrer. "Interatomic Forces in Scanning Tunneling Microscopy: Giant Corrugations of the Graphite Surface". In: *Physical Review Letters* **57** (1986), pp. 444–447. DOI: 10.1103/PhysRevLett.57.444. (Cit. on p. 65).

[Stö13] H. Stöcker. *Taschenbuch der Physik*. 7th ed. Europa-Lehrmittel - Nourney, Vollmer GmbH & Co. KG, 2013, p. 424 (cit. on p. 56).

[Ter83] J. Tersoff and D. R. Hamann. "Theory and Application for the Scanning Tunneling Microscope". In: *Physical Review Letters* **50** (1983), pp. 1998–2001. DOI: 10.1103/PhysRevLett.50.1998. (Cit. on p. 11).

[Ven84] J. A. Venables, G. D. T. Spiller, and M. Hanbucken. "Nucleation and growth of thin films". In: *Reports on Progress in Physics* **47**. (1984), p. 399. DOI: 10.1088/0034-4885/47/4/002. (Cit. on p. 9).

[Voi15] Bert Voigtländer. *Scanning Probe Microsopy*. Springer-Verlag Berlin Heidelberg, 2015, pp. 279–334. DOI: 10.1007/978-3-662-45240-0 (cit. on pp. 12, 13).

[Vol10] M. Vollmer and K.-P. Möllmann. "Fundamentals of Infrared Thermal Imaging". In: *Infrared Thermal Imaging*. Wiley-VCH Verlag GmbH & Co. KGaA, 2010, pp. 35–44. DOI: 10.1002/9783527630868.ch1. (Cit. on p. 20).

[Wil01] A. Wiltner, A. Rosenhahn, J. Schneider, C. Becker, P. Pervan, M. Milun, M. Kralj, and K. Wandelt. "Growth of copper and vanadium on a thin Al_2O_3-film on $Ni_3Al(111)$". In: *Thin Solid Films* **400**. (2001), pp. 71–75. DOI: 10.1016/S0040-6090(01)01453-5. (Cit. on p. 73).

[Wut86] M. Wutz, H. Adam, and W. Walcher. *Theorie und Praxis der Vakuumtechnik*. 3rd ed. Friedr. Vieweg & Sohn Verlagsgesellschaft mbH, 1986, pp. 72–384 (cit. on pp. 17, 87).

List of Figures

List of Tables

Acknowledgement

I would like to thank various people for their help during the past years.
First and foremost I wish to acknowledge the guidance and support of my supervisor Prof. Dr. Heinz Hövel. Not only his tremendous knowledge, but also his prudence and advice are attributes I value most. I am also grateful for the opportunity to participate in workshops of the cluster community and for the trust in me planning the movement of the UHV system to the laboratory in the new physics building.
Thanks to Prof. Dr. Mirko Cinchetti for his interest in the project and for acting as referee for this thesis. I appreciate the effort of Prof. Dr. Dr. Wolfgang Rhode and Dr. Bärbel Siegmann for completing the board of examiners.
Prof. Dr. Conrad Becker provided me with valuable information concerning the sample preparation. I am grateful for his constructive recommendations.
I would also like to thank Prof. Dr. Metin Tolan for providing funds enabling research activities such as attending conferences all over the world. Furthermore, his anecdotes always brought a smile to my face.
I am thankful to Dr. Christoph Schröder, who introduced me in the laboratory during my master's thesis and helped with many issues occurring at the beginning of the project. In the same manner, I would like to thank Matthias Bohlen, Raphael Floegel, Philipp Gust and Alexander Kononov for gathering measurement data, fruitful discussions and useful ideas.
I also express my gratitude to our technicians Thorsten Witt and Georg Jülicher, who assisted in numerous eletronic and mechanical problems. Thanks to Susanne Kralemann and the mechanical workshop for producing a new sample plate with proper mounting and for welding the KF-flanges for the new foreline system. The installation of the new photoelectron spectroscopy setup would not have been possible without the construction skills of Lutz Feldmann who designed a support for the analyser and the monochromator of the VUV light source. In this context I am particularly grateful for training and support during the movement and installation through Scienta Omicron represented primarily by Jens Garleff

and Vincent Lehane. Klaus Wiegers and Daniel Tuettmann provided helium and nitrogen, liquid and gaseous, when it was needed - thank you!
I wish to acknowledge the excellent working atmosphere within the chair E1a. We shared not only the work site, but also many activities and interests such as soccer, bowling and having at least one beer at various graduation parties. I honor the helpfulness of everybody.
Special thanks to Dr. Christoph Schröder, Dr. Paul Salmen and Dr. Stefanie Roese, who shared an office with me. Always welcomed guests from our coffee group were Dr. Julia Nase, Dr. Julian Schulze and Dr. Holger Göhring. I enjoyed every single lunch break while discussing topics far apart from physics. I love sharing a coffee with all of you.
I would like to thank my friends, which let me forget about physics and work, leastwise on weekends. I express my very great appreciation to my parents for their support, their confidence and their encouragement.
Finally, my deepest gratitude to my wife Jessica. She always behaves supportively towards me, despite the lack of time due to working on weekends and attending numerous conferences. Thanks for taking care of our son Lukas. His curiosity and foolishness enrich my life.